

GEO-LOCATION OF INDIVIDUAL LIGHTNING
DISCHARGES USING IMPULSIVE VLF
ELECTROMAGNETIC WAVEFORMS

A DISSERTATION
SUBMITTED TO THE DEPARTMENT OF ELECTRICAL ENGINEERING
AND THE COMMITTEE ON GRADUATE STUDIES
OF STANFORD UNIVERSITY
IN PARTIAL FULFILLMENT OF THE REQUIREMENTS
FOR THE DEGREE OF
DOCTOR OF PHILOSOPHY

Troy Gaylon Wood
December 2004

© Copyright by Troy Gaylon Wood 2005
All Rights Reserved

I certify that I have read this dissertation and that, in my opinion, it is fully adequate in scope and quality as a dissertation for the degree of Doctor of Philosophy.

Umran S. Inan(Principal Adviser)

I certify that I have read this dissertation and that, in my opinion, it is fully adequate in scope and quality as a dissertation for the degree of Doctor of Philosophy.

Timothy F. Bell

I certify that I have read this dissertation and that, in my opinion, it is fully adequate in scope and quality as a dissertation for the degree of Doctor of Philosophy.

Antony C. Fraser-Smith

Approved for the University Committee on Graduate Studies:

Dedication

To my parents
Gaylon and Audrey
and to the Sundgrens
Wendy, Chris and Jackson

Abstract

Every second, lightning strikes the ground up to 200 times around the world with flashes occurring more frequently in some places than others. A variety of systems exist that detect and locate lightning flashes for a variety of commercial and scientific applications including air traffic control, climate modeling, and for use by the electric utility industry. These lightning detection systems have a wide range of capabilities in their detection accuracy and in their spatial and temporal coverage. For example, commercial detection systems provide very precise time and location information for lightning strikes but also require a densely packed array of sensors limiting their coverage to areas where those sensors can be placed. At the other extreme, the sensors aboard satellites can detect lightning all around the world yet any particular area is only visible for a few minutes each day as the satellite passes over it.

When lightning strikes it generates an impulsive broadband electromagnetic pulse known as a radio atmospheric (sferic). The radiation in the very low frequency and extremely low frequency (VLF/ELF) bands (300-30,000 Hz) of the sferic propagates through the waveguide formed by the Earth and the ionosphere with low attenuation. Because of this low attenuation sferics can be detected at distances in excess of 10,000 km from their source lightning locations.

A new technique of global lightning location is presented that takes advantage of propagation characteristics of the VLF/ELF frequency band. The technique employs a few widely (9,000 km) spaced receivers to provide continuous regional coverage of lightning activity. By combining magnetic direction finding and time of arrival difference measurements in the VLF/ELF band, individual lightning strokes are located to within ~ 100 km of their source locations. The influences of the Earth/ionosphere

waveguide on VLF wave propagation are discussed and lightning location results are compared with existing lightning detection systems.

Acknowledgements

As you sit through the many long nights in front of your computer writing your dissertation, you can not help but to reflect on what got you to this point. And despite all of the bickering and complaining that goes on during this time you realize that your time at Stanford is coming to an end and you are thankful for all of those people that have supported, encouraged, assisted and befriended you along the way.

I would like to thank my principal advisor, Professor Umran Inan, for his steadfast support and enthusiasm and for keeping his sense of humor during my tenure at Stanford. Special thanks to Professor Antony Fraser-Smith for helping to keep things in the right perspective and to Dr. Tim Bell for his advice and wisdom on technical matters.

As my research involved using data acquired all around the world, I would like to thank all of my fellow researchers and colleagues who made my research possible. In particular, I would like to thank the science technicians at Palmer Station, Jeff Otten and John Booth, for tending to our experiments during the cold Antarctic months. Thanks to Colin Price, Yoav Yair and Boris Starobinets for their assistance in acquiring data in the Negev desert. Thanks to Hank Voss and Bob Davis at Taylor University. Thanks to my colleagues in the lighting community, especially Kenneth Cummins for his generosity with NLDN data, Phil Krider for his prompt replies to my many annoying questions and to Dennis Boccippio for his thorough (and often referenced) responses to my inquiries.

I am immensely grateful to all of the members of the VLF group. Thanks to Steve Cummer and Victor Pasko for helping to get started on the right path. Thanks to Jerry Yarborough and Bill Trabucco for their vast experience and technical expertise.

Thanks to Shaolan Min for keeping everything in order and running smoothly. Of course, thank you to all of the VLF students who are also my friends.

I would also like to thank my parents, Gaylon and Audrey Wood, my sister Wendy Sundgren, her husband Chris and my nephew Jackson for their love and for always being there in the past, present and future.

Troy Wood
Stanford, California
December 10, 2004

This research was supported by the National Science Foundation under grant OPP-9910565 and by NASA under grant NGT 5-50227. NLDN data provided by the NASA Lightning Imaging Sensor (LIS) instrument team and the LIS data center via the Global Hydrology Resource Center (GHRC) located at the Global Hydrology and Climate Center (GHCC), Huntsville, Alabama through a license agreement with Global Atmospheric, Inc. (GAI). The data available from the GHRC are restricted to LIS science team collaborators and to NASA EOS and TRMM investigators.

Contents

Dedication	iv
Abstract	v
Acknowledgements	vii
1 Introduction	1
1.1 The Lightning Discharge	2
1.2 Radio Atmospherics	5
1.3 History of Global Lightning Observations	7
1.4 Lightning Detection Data Systems	8
1.4.1 Space-borne Lightning Detection	8
1.4.2 The National Lightning Detection Network	9
1.4.3 Additional Lightning Detection Systems	12
1.5 Contributions	12
2 Propagation in the E-I Waveguide	14
2.1 Ideal Parallel Plate Waveguide	14
2.2 Mode Excitation in a Parallel Plate Waveguide	19
2.2.1 Sferic Sources	19
2.2.2 Excitation of Waveguide Modes	20
2.3 The Earth-Ionosphere Waveguide	22
2.3.1 Properties of the Earth and Ionosphere	22
2.3.2 Theory of Earth-Ionosphere Waveguide Propagation	25

2.3.3	Correction for Curved Earth	27
2.3.4	VLF Propagation Characteristics	27
3	Sferic Detection and Direction Finding	29
3.1	Data Acquisition	29
3.1.1	Magnetic Loop Antenna	30
3.1.2	Pre-Amplifier and Line Receiver	31
3.1.3	Analog to Digital Conversion	32
3.2	Sferic Detection	34
3.2.1	Detection Filtering	34
3.2.2	Time of Arrival Determination	37
3.3	Direction Finding	38
3.4	Polarization and Quasi-mode Errors	40
3.5	Site Error Correction	41
3.6	Arrival Azimuth Verification	43
3.7	Correlation of Sferic Energy and Peak Current	52
3.8	Monitoring of Thunderstorms	53
3.9	Measurement of Lightning Stroke Rate	59
4	Lightning Triangulation	64
4.1	VLF Receiver Sites	64
4.2	Two Station Triangulation Algorithm	64
4.2.1	Location Grid	64
4.2.2	Computational Solution	67
4.3	Two Station Triangulation Simulation	72
4.3.1	Location Error	72
4.3.2	Antipodal Error	73
4.3.3	Mismatch Error	75
4.4	Two Station Triangulation Observations	76
4.5	Three Station Triangulation	82
4.6	Three Station Triangulation Observations	86

5	Summary and Suggestions for Future Work	89
5.1	Summary	89
5.2	Future Research Suggestions	91
5.2.1	Direction Finding Improvements	91
5.2.2	Triangulation Improvements	92
A	Derivation of Equations	94
A.1	Great Circle Intersection	94
A.2	Derivation of Antenna Parameters	98
	Bibliography	100

List of Figures

1.1	A cartoon of the various phases of a negative cloud-to-ground lightning flash [Adapted from <i>Rakov</i> , 2003, p. 110].	3
1.2	Ten second frequency-time spectrum showing sferics and transmitter signals from 0-20 kHz.	5
1.3	Example time domain waveform of a large sferic received at Palmer Station.	6
1.4	Number of thunderdays occurring during a year.	8
1.5	Optical Transient Detector Seasonal Flash Density (a.) December-February, (b.) March-May, (c.) June-August, (d.) September-October [Adapted from images available through the Global Hydrology Resource Center]	10
2.1	Wave propagation in an ideal waveguide with perfectly conducting boundaries.	15
2.2	Mode-Frequency relationships in ideal waveguide with height $h = 100$ km. a: Mode angle versus frequency for first 5 waveguide modes. b: Group arrival time versus frequency for first 5 modes and TEM mode at a distance of 5000 km.	17
2.3	Sferic spectrum from Upland, Indiana showing tweeks caused by the first five waveguide mode cutoffs.	19
3.1	Typical VLF Receiver System	30
3.2	Frequency Response of VLF Receiver at Palmer Station, Antarctica .	33
3.3	Stages of Sferic Detection Algorithm	35
3.4	Time of Arrival Dependence on Threshold Setting	37

3.5	Antenna Distortion Parameters	42
3.6	Example Site Error Correction Curves	43
3.7	The lines labelled -40° to 0° represent great circle paths from North America to Palmer Station, Antarctica.	44
3.8	Each green cross represents the location of an NLDN cloud-to-ground lightning flash and the lines represent the great circle paths to Palmer Station.	45
3.9	Histogram of the errors between arrival azimuths calculated from NLDN data and azimuths obtained from direction finding at Palmer Station.	47
3.10	Comparison between arrival azimuth, detection efficiency and azimuth error.	48
3.11	Histogram of the errors between arrival azimuths calculated from NLDN data and azimuths obtained from direction finding at Vieques Island.	50
3.12	Azimuth errors between sferics detected at Vieques Island and LIS total lightning data.	51
3.13	Divisions in arrival azimuth for sferics matched to NLDN flashes.	53
3.14	Linear correlation coefficients of VLF intensity verses NLDN peak current for sferics matched to NLDN flashes.	54
3.15	Histograms of arrival azimuths calculated from NLDN data.	55
3.16	Histograms of sferic arrival azimuths.	56
3.17	OTD data with azimuth lines to Palmer Station (top) and a comparison of projected OTD azimuths to sferic azimuth data (center and bottom).	58
3.18	A rate comparison between sferics detected at Palmer Station with an azimuth between -21° and -23° and NLDN CG flashes with calculated azimuths between -21° and -23°	59
3.19	Ratio of height gain functions for two least attenuated modes, M_1 and M_2 , to TEM mode at 7.5 kHz. R_{nonNLDN} is the ratio for sferics not matched to NLDN flashes and R_{NLDN} is the ratio for sferics matched to NLDN flashes	62
4.1	Important VLF receiver sites around the world.	65

4.2	Lines of azimuth from Palmer Station (red) and Vieques Island (blue).	65
4.3	Lines of equal time of arrival difference between Palmer Station and Vieques Island.	67
4.4	Two Station Triangulation Illustration	68
4.5	Two Station Lookup Table	69
4.6	Two station chi-square cost map.	70
4.7	Simulated location error.	73
4.8	Simulated antipodal error.	74
4.9	Simulated mismatch error.	75
4.10	Detection efficiency of the triangulation algorithm.	77
4.11	Location accuracy of the triangulation algorithm.	78
4.12	Comparison of triangulated lightning source locations to LIS lightning flashes.	79
4.13	Sferic Count for region bounded by 8° S and 13° S latitude and 71° W and 80° W longitude.	82
4.14	Equal time of arrival difference curves between Palmer Station and Sde Boker.	83
4.15	Equal time of arrival difference curves between Palmer Station and Upland.	84
4.16	Equal time of arrival difference curves between Upland and Sde Boker.	84
4.17	Azimuth Lines and TOAD curves for three station triangulation. . . .	85
4.18	Three station chi-square cost map.	86
4.19	NLDN flash density for 0000 – 2400 UT, 01 August 2002.	87
4.20	Three station triangulated event density 0000-2400 UT 01 August 2002.	88
A.1	Linearized Plot of Spherical Geometry.	95
A.2	Antenna Distortion Parameters	98

Chapter 1

Introduction

“He unleashes his lightning beneath the whole heaven and sends it to the ends of the earth” Job 37:3

Since the beginning of recorded history, lightning has been a source of fascination and inspiration to mankind. Greek mythology describes thunder and lightning as the mighty weapons of Zeus, forged by the Cyclopes in Hephaistos’s workshop. In the Bible, lightning is often depicted as a manifestation of the wrath of God. Even today, people, and insurance companies, often describe lightning related deaths and destruction as “acts of God”.

In less dramatic fashion, the scientific study of lightning has progressed over the years beginning modestly with the invention of the lightning rod by Benjamin Franklin in the mid 1700’s and accelerating in the last 30 years due to the development of high speed data acquisition techniques [Uman, 1987, pp. 7-8]. Lightning radiates an electromagnetic pulse which contains energy over a wide bandwidth, spanning from just a few hertz [Burke and Jones, 1992] up to tens of megahertz [Weidman and Krider, 1986]. Due to the sub-millisecond to millisecond time scales and several kilometer spatial scales associated with the lightning current, most of the energy in the radiated spectrum is contained in the Extremely Low Frequency (ELF 3-3000 Hz) and Very Low Frequency (VLF 3-30 kHz) bands [Uman, 1987, p. 118]. The electromagnetic pulses from lightning at ELF/VLF frequencies are known as radio atmospherics, more often referred to as sferics, and are the primary focus of this

dissertation. At ELF and VLF frequencies, electromagnetic waves are reflected by the ground and by the conducting layer of the atmosphere known as the ionosphere, and they can thus be efficiently guided around the Earth. In this “Earth-ionosphere” waveguide, sferics propagate with low loss (typically 2-3 dB/1000 km) and can therefore be detected at great distances from their source locations [Davies, 1990, p. 367]. By observing sferics at several different locations, the source locations of the individual lightning discharges can be determined [Horner, 1954]. Also, the characteristics of the sferic waveforms observed at each receiver yield information about the source lightning and properties of the ionosphere and the ground along the propagation path [Cummer, 1997, p. 42-58].

1.1 The Lightning Discharge

Within a typical thundercloud an electric dipole is formed between a large main positively charged layer located above a negatively charged layer of equal magnitude [Rakov and Uman, 2003, p. 68]. This separation of charge is believed to be caused primarily by the so-called graupel-ice mechanism in which heavier graupel particles fall and interact with lighter ice particles caught in the updraft of a thunderstorm [Rakov and Uman, 2003, p. 86]. This interaction results in the larger heavier particles carrying a net negative charge and the smaller lighter particles carrying a net positive charge. Once these charged layers contain enough charge, the electric fields associated with the charge separation might begin to exceed the dielectric breakdown voltage of air, leading to a lightning flash.

Lightning flashes can be roughly classified into two groups; cloud flashes, those that do not terminate at the Earth’s surface, and ground flashes, those with at least a partial discharge to the Earth’s surface [Prentice and Mackerras, 1977]. Historically, cloud flashes are the most numerous type of lightning but are also the hardest to definitively identify [Prentice and Mackerras, 1977]. Ground flash discharges can also be divided into two groups depending on which layer of charge they originate in. If the ground flash originates in the negatively charged layer it is called a negative cloud-to-ground flash and electrons are moved from the cloud to the ground. If the ground

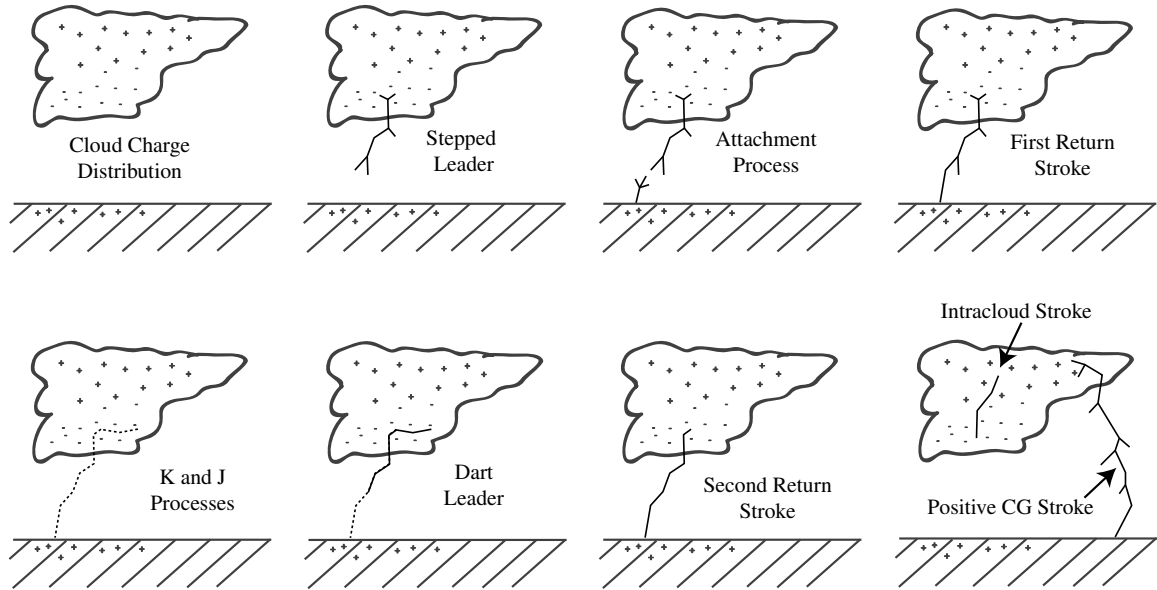


Figure 1.1: A cartoon of the various phases of a negative cloud-to-ground lightning flash [Adapted from *Rakov*, 2003, p. 110].

flash originates in the positively charged layer it is called a positive cloud-to-ground flash and positive charge is moved from the cloud to the ground. In other words, electrons travel from the ground to the cloud.

As illustrated in Figure 1.1, a negative cloud-to-ground flash is initiated when a conductive channel known as a stepped leader begins to work its way down from the cloud after a preliminary breakdown within the negatively charged layer. The stepped leader approaches the ground in a series of discrete steps that are 10's to 100's of meters in length. As the stepped leader advances downward the electric field between the end of the stepped leader and the ground becomes high enough that conductive leaders begin to reach upwards from the ground until the stepped leader and a conductive leader are only 10 to 100 meters apart. Once within this “striking distance”, attachment occurs and a conductive channel is created between the negatively charged layer of the cloud and the ground. At this point the first return stroke of the flash occurs and a large electric current flows from the ground to the cloud generating an electromagnetic impulse, i.e., a radioatmospheric or a

spheric. The current typically has a peak value of around 30 kiloamps (kA) but intense return strokes may have currents in excess of several hundred kA. Also, due to the time duration of the primary current and the typical lengths (i.e., ~ 7 km in Florida [Rakov and Uman, 2003, p. 123]) of the conductive channel, the peak intensity of the radiated field of the spheric lies in the 1-10 kHz range [Uman, 1987, p. 377]. After the first return stroke the layer of charge may be depleted resulting in the termination of the flash. However, if additional charge is available, processes known as J and K occur that redistribute the remaining charge in the cloud [Uman, 1987, p. 179]. The J-process is characterized by a steady electric field change over a period of tens of milliseconds and K-processes are characterized by small relatively rapid electric field variations at intervals of 2-20 milliseconds [Uman, 1987, p. 179]. The conducting channel from the first return stroke is still partially ionized following the first return stroke and a dart leader re-ionizes the channel leading the way for a second return stroke. This process may occur over and over again resulting in dozens of return strokes in a given lightning flash with intervals between return strokes of tens of milliseconds. Subsequent return strokes after the first one typically have peak currents that are about half that of the first return stroke [Berger *et al.*, 1975]. Figure 1.1 depicts the various stages of a two stroke negative cloud-to-ground lightning flash.

A similar process occurs for positive cloud-to-ground discharges. Positive cloud-to-ground flashes typically have higher peak currents than negative cloud-to-ground flashes but also make up a smaller percentage of all lightning flashes, although the ground flashes in some storms are predominantly positive flashes [Rakov and Uman, 2003, p. 214].

As mentioned above, cloud flashes are the most common type of lightning discharge, with their occurrence within typical thunderstorms typically exceeding ground flashes by a ratio of about 3 to 1 [Prentice and Mackerras, 1977]. Cloud flashes occur between the negatively charged and the positively charged layers of thunderclouds and can have currents of similar magnitude to cloud-to-ground discharges [Rakov and Uman, 2003, p. 323].

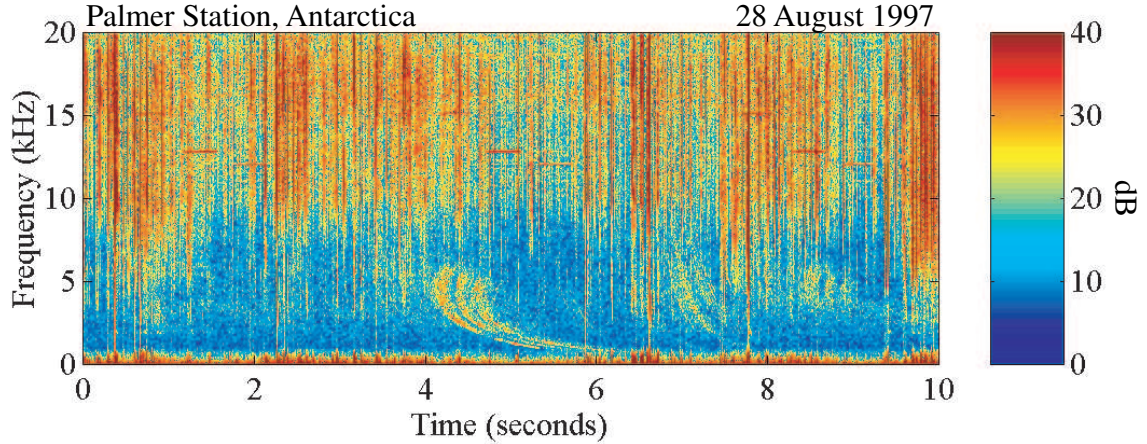


Figure 1.2: Ten second frequency-time spectrum showing sferics and transmitter signals from 0-20 kHz.

1.2 Radio Atmospherics

The Extremely Low Frequency (ELF) and Very Low Frequency (VLF) bands of radio atmospherics (sferics) have been studied for more than fifty years. The initial interest in this frequency range was due to the application of VLF transmission for long range radio communications. ELF and VLF waves were found not only to reflect between the earth and the ionosphere, making non-line-of-sight communication possible, but also to have low attenuation over long distances, namely $\sim 2\text{-}3$ dB/1,000 km for VLF and even as low as ~ 0.3 dB/1,000 km at 10 Hz [Jones, 1967]. Thus, these frequency bands were deemed ideal for transcontinental communication and for communication with ocean going vessels.

Figure 1.2 displays a frequency-time spectrogram covering the range from 0-20 kHz showing the typical signals that occupy the ELF/VLF frequency band. Each vertical line in the figure is a sferic and, even at this resolution, hundreds are visible during the 10 seconds shown. Each of these sferics originate at lightning discharges occurring in thunderstorms located all around the world, propagating to the receiver location through the Earth-ionosphere waveguide. The horizontal lines visible between 10-15 kHz are the Russian Alpha transmitters which are used for navigation. A series of

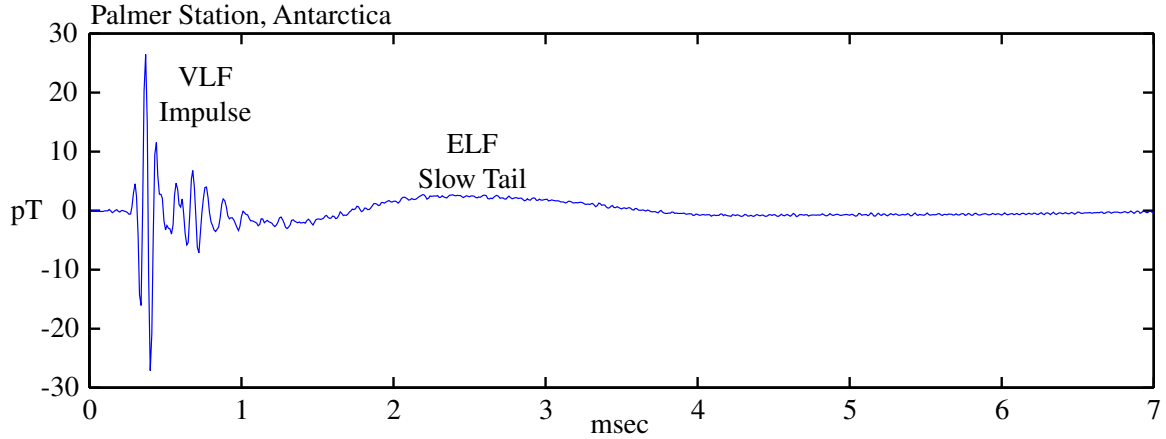


Figure 1.3: Example time domain waveform of a large sferic received at Palmer Station.

whistlers [Helliwell, 1965] covering the 1-7 kHz frequency band is also visible starting at around the 4 second mark. Whistlers acquire their particular dispersed frequency-time forms as a result of their propagation in field aligned ducts of enhanced ionization along the Earth’s magnetic field lines. The sferic wave energy originating in lightning flashes in one hemisphere leaks upward into the magnetosphere during the course of the propagation in the Earth-ionosphere waveguide, and propagates through the magnetosphere to the geomagnetic conjugate region, where it couples back into the Earth-ionosphere waveguide and is observed on the ground.

A typical sferic pulse in the time domain looks much like the relatively large amplitude sferic shown in Figure 1.3. Sferics generally consist of a VLF impulse lasting less than one millisecond and are sometimes followed by a lingering ELF component known as an ELF “slow tail” [Reising *et al.*, 1999] which typically lasts for an additional 1-3 milliseconds (A “slow tail” is visible in Figure 1.3). The oscillatory nature of the initial VLF portion is due to the superposition of different waveguide modes after multiple reflections between the Earth and the ionosphere [Horner and Clarke, 1955]. As mentioned before, the bulk of the energy of a sferic lies in the ELF/VLF range with a typical peak occurring in the 2.5-10 kHz range [Cummer, 1997, p. 33]. In general, however, the duration and spectral content of sferics are highly variable, often

manifested in the form of some unusual waveforms [Cummer, 1997, p. 38-41].

Much of the early research on sferics involved their classification based on differences in spectral properties and attempts to understand these differences. For example, *Burton and Boardman* [1933] classified sferics into musical and non-musical varieties based on how they sounded when played in audio form. The musical sferics were further classified into two types called “tweeks” and “swishes”. *Burton and Boardman* [1933] correctly theorized that the ~ 1700 Hz tail visible in “tweeks” is caused by height of the reflecting ionospheric layer, thus recognizing the cutoff frequency for the first waveguide mode. *Burton and Boardman* [1933] also observed diurnal variations in sferic occurrence and a decrease in the received signal strength of sferics during daytime relative to nighttime. Other researchers noticed that the waveforms of sferics were different depending on whether their propagation paths to the receiver were over land or over sea [Chapman and Pierce, 1957]. Others estimated the range to sferic sources and the height of the ionosphere by measuring the time difference between reflections from the Earth and the ionosphere [Horner and Clarke, 1955].

1.3 History of Global Lightning Observations

One of the first and possibly most famous global lightning study was published by *Brooks* [1925]. In this study, *Brooks* obtained “thunder day” data from hundreds of weather stations located around the world, which simply stated whether or not thunder had been heard at a particular station on a particular day. Using these sparse and often unreliable meteorological records and a lot of educated guessing, *Brooks* estimated that globally there were about 1,800 thunderstorms in progress at any moment and that these storms produced an average of about 100 lightning flashes every second. Figure 1.4 shows a map similar to that which *Brooks* used to make his estimate, displaying the number of “thunder days” (i.e., the number of days a year thunder was heard at a station) recorded for regions around the world. Over 50 years later, based on a wide variety of lightning measurements over the 50 year period, *Orville and Spencer* [1979] derived a remarkably similar value in the range of 79-142 flashes per second depending on the season. More recent estimates based

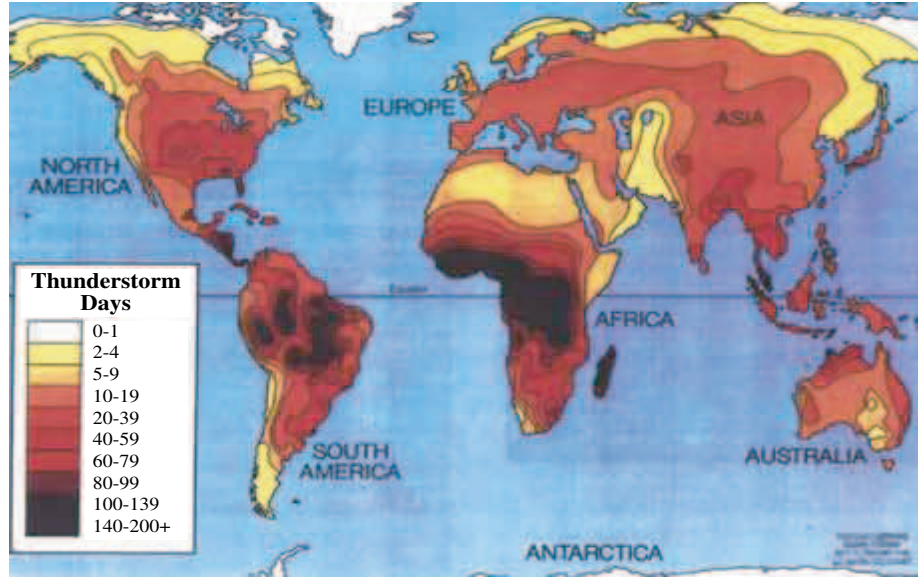


Figure 1.4: Number of thunderdays occurring during a year.

on satellite observations of lightning occurrence indicate the global flash rate may be a more modest 40 lightning flashes per second [Christian *et al.*, 1999a]. Although a single value is often quoted as the global flash rate, the lightning flash rate for any particular area varies significantly over the course of a day and from season to season.

1.4 Lightning Detection Data Systems

1.4.1 Space-borne Lightning Detection

The first targeted detection of lightning from a space-borne platform was realized with the Optical Transient Detector (OTD) [Christian *et al.*, 2003] which was followed by the Lightning Imaging Sensor (LIS) [Christian *et al.*, 1999b; Ushio *et al.*, 2002] launched aboard the Tropical Rainfall Measuring Mission (TRMM) satellite in 1997. The TRMM satellite is located at 350 km altitude and its orbit has an inclination of 35°. The LIS sensor detects total lightning by registering optical transients, which occur as a result of the scattering within the tops of the clouds of luminous radiation produced by lightning channels.

With a 600 km field of view, LIS can view a particular spot on the earth for 90 seconds at a time and reports optical transients detected by a CCD imager with 2 ms resolution. The lowest level of data provided by LIS is called an “event”, which is a transient detected on a single pixel. Events that are adjacent to each other are placed into units called “groups”. A group roughly corresponds to an optical event from a lightning stroke. LIS “flashes” are sets of groups that are separated by not more than 330 ms in time and 5.5 km in distance. Over an extended period of time LIS can create density maps for lightning occurrence over the entire Earth. A similar map created from OTD data (using a similar sensor but covering larger portions of the Earth due to the higher inclination of the satellite) is shown in Figure 1.5. These maps show that most lighting occurs in the southern hemisphere during the months from December to February and in the northern hemisphere during the months from June to August.

Unfortunately, the optical emissions detected by LIS and OTD do not correspond exactly to the electromagnetic radiation from lightning discharges. Thus, it is sometimes difficult to correlate LIS data to other data sets such as VLF sferic data or National Lightning Detection Network data. Nevertheless, some comparisons showing spatial and temporal differences between LIS and other data sets have been documented [*Ushio et al.*, 2002].

1.4.2 The National Lightning Detection Network

The National Lightning Detection Network (NLDN) provides lightning data for North America and its vicinity [*Cummins et al.*, 1998]. This network provides support to the electric utility industry, the National Weather Service, the Federal Aviation Administration and other government and commercial users. The network uses a proprietary (U.S. Patents 4,115,732 4,198,599 4,245,190 4,806,851) [*Krider et al.*, 1976] time of arrival/magnetic direction finder (TOA/MDF) technique to detect cloud-to-ground (CG) lightning events. CG flashes are singled out by matching received broadband (1 kHz - 1 MHz) waveforms to the signature waveform expected from the direct wave of a CG lightning return stroke [*Cummins et al.*, 1998]. This technique eliminates

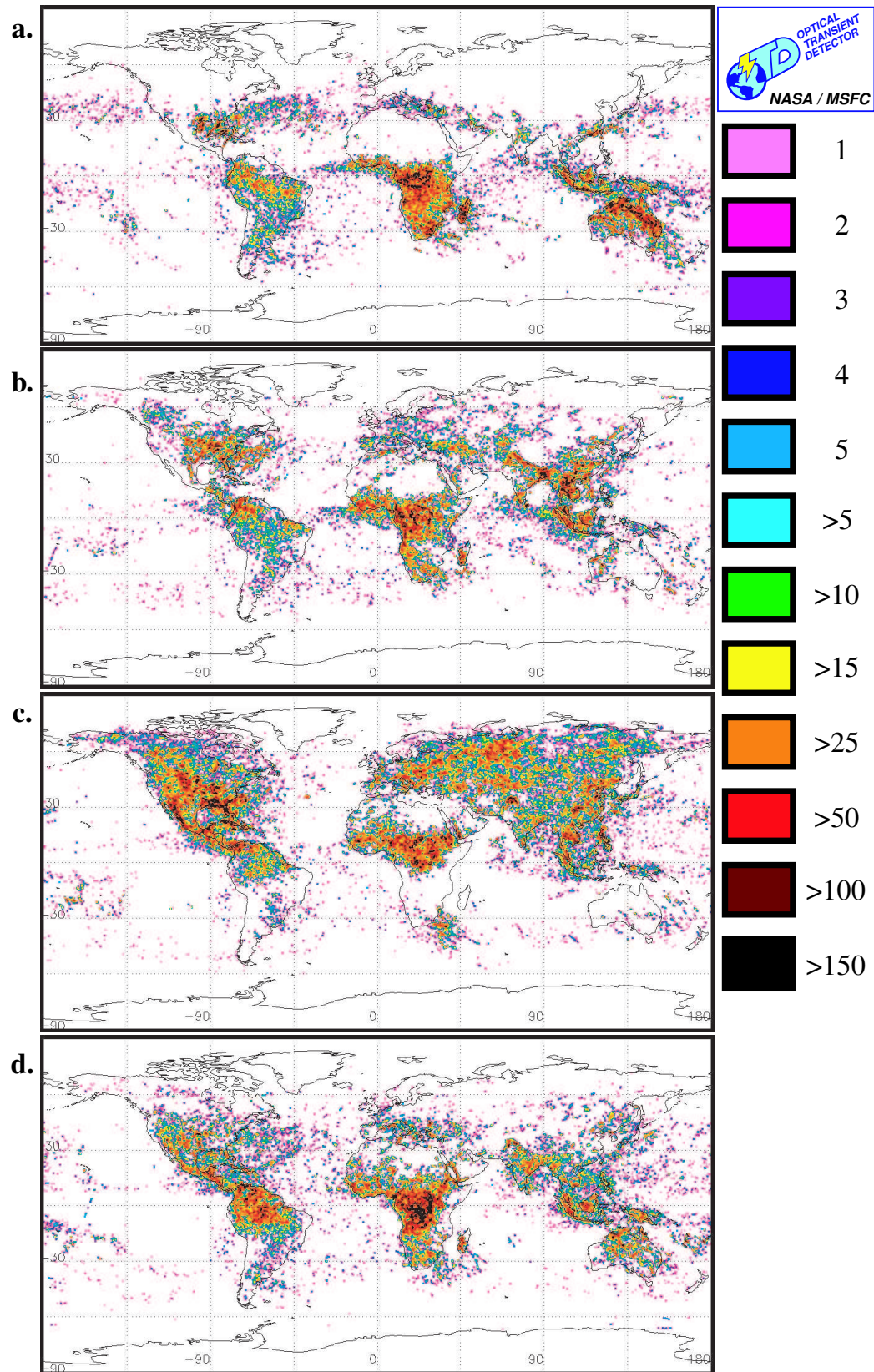


Figure 1.5: Optical Transient Detector Seasonal Flash Density (a.) December-February, (b.) March-May, (c.) June-August, (d.) September-October [Adapted from images available through the Global Hydrology Resource Center]

many of the errors caused by multiple reflections from the ionosphere and the ground as well as polarization errors [Krider *et al.*, 1976], but requires high frequency components of the sferic spectra that are often too weak to measure at large distances. Commercially available NLDN data typically excludes intra-cloud (IC) lightning from detection based on the fact that waveforms of IC discharges are distinctly different from the waveforms of CG generated sferics [Krider *et al.*, 1976].

The NLDN data used in this dissertation gives the time, location, peak current and polarization, the number of return strokes and several location accuracy parameters for individual lightning flashes. The data available typically have a time accuracy of 1 millisecond, although higher resolution data is also available. Flashes are located with a median error of 500 meters and with a detection efficiency between 80% and 90% for flashes with first return stroke peak currents greater than 5 kA. The detection efficiency is significantly lower ($\sim 50\%$) for subsequent return strokes since, as mentioned previously, multiple return strokes typically have peak currents that are about one half that of the first return stroke [Berger *et al.*, 1975]. The peak intensity of a lightning flash is sometimes provided as a range-normalized value of the signal strength (RNSS) which is based on the signal propagation model given by Cummins *et al.* [1998]. Based on this model, RNSS is linearly related to current using the equation

$$I_{\text{peak}}(\text{kA}) = 0.185 \times \text{RNSS} \quad (1.1)$$

While the peak current does not adequately describe the shape or duration of a sferic waveform in the VLF frequency band, results indicate that the peak current values provided by the NLDN are highly correlated with the maximum VLF signal intensity in sferics [Wood and Inan, 2000].

In this dissertation, comparisons are often said to be made with NLDN flashes when in reality, the comparisons are being made only with the first return stroke of the associated flash.

1.4.3 Additional Lightning Detection Systems

On the ground, many other methods of radio location of lightning have been implemented. For example, a single radio receiver can be used to locate intense lightning discharges at long range by using the wave impedance of the lightning waveform to estimate the range to the lightning strike and by using magnetic direction finding to measure the arrival azimuth of the lightning strike [Burke and Jones, 1995; Huang *et al.*, 1999; Price and Asfur, 2002]. Together, these measurements determine the location of the source lightning event. Lightning discharges measured in this manner must be intense because a large ELF energy component, also called an ELF slow-tail, is required for the range estimate [Burke and Jones, 1995]. The most common methods for the radiolocation of lightning involve the use of measurements at multiple sites. Some of these methods rely on magnetic direction finding (MDF) [Horner, 1954; Hiscox *et al.*, 1984] while other methods use arrival time difference (ATD) [Lewis *et al.*, 1960; Lee, 1986; Lee, 1990; Fullerkrug and Constable, 2000; Dowden *et al.*, 2002]. There have also been some experiments that use both MDF and ATD for location [Hughes and Gallenberger, 1974]. The techniques used vary in complexity and the number of measurement sites, as well as in accuracy and spatial coverage.

1.5 Contributions

The contributions of this dissertation are as follows:

- Development of a new algorithm for geo-location of individual lightning discharges using very low frequency impulsive electromagnetic signatures measured at global distances ($> 10,000$ km). This algorithm combines magnetic direction finding and time of arrival difference measurements and is easily adaptable to account for both simple or very complex models of the propagation environment.
- Application of the new technique to track the development of lightning and thunderstorms on a regional scale and to quantify lightning flash rates. Flash rates were seen to vary in a repeatable pattern over a twenty-four hour period in agreement with the natural variation of other atmospheric parameters.

- Demonstration of the detection of sferics from both cloud-to-ground and intra-cloud lightning and identification of a possible method of discriminating between the two types of lightning based on their different spectral characteristics.
- Demonstrated the detection of sferics from intra-cloud lightning by observing a ninety-degree difference in the arrival azimuths of some sferics when compared to the expected arrival azimuth of those sferics as calculated from Lightning Imaging Sensor data.

Chapter 2

VLF Propagation in the Earth-Ionosphere Waveguide

One of the defining characteristics of sferics is that the VLF energy that constitutes them propagates around the Earth in a guided fashion multiply reflecting between the Earth and the ionosphere. VLF propagation within the Earth-ionosphere waveguide incurs low yet highly variable attenuation, which is dependent on frequency and the properties of the waveguide over the propagation path. These properties include the reflection height of the ionosphere, which depends on day/nighttime conditions, land/sea path conductivity differences and east/west propagation differences caused by the orientation of the Earth's magnetic field. All of these factors affect the sferic waveform as observed at the receiver and should be kept in mind when performing sferic analysis.

2.1 Ideal Parallel Plate Waveguide

Many of the concepts associated with an ideal parallel plate waveguide are applicable in studying the propagation of VLF waves in the Earth-ionosphere waveguide, which, in fact, is far from being an ideal guiding structure. Consider a region of space bounded by two perfectly conducting parallel plates located at $z = 0$ and $z = h$, as shown in Figure 2.1. Now consider a linearly polarized plane wave propagating

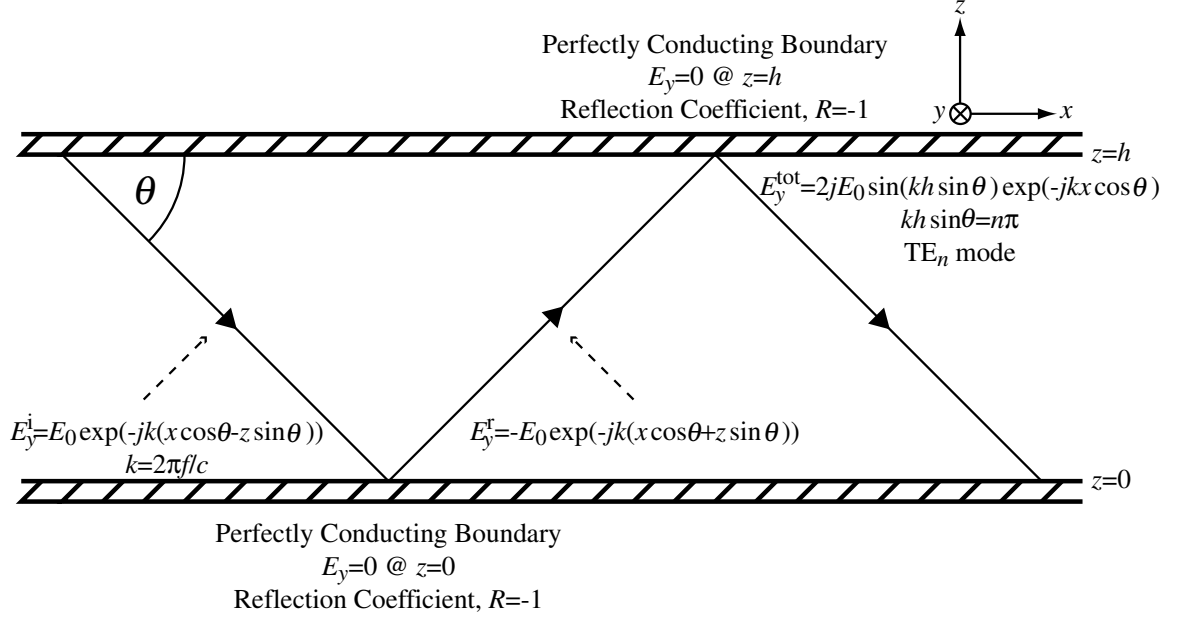


Figure 2.1: Wave propagation in an ideal waveguide with perfectly conducting boundaries.

downwards in the x - z plane at an angle θ relative to the x -axis and with its electric field vector parallel to the y -axis (perpendicularly polarized). The electric field of the wave incident on the lower plate can then be written as

$$E_y^i = E_0 \exp\{-jk(x \cos \theta - z \sin \theta)\} \exp(j\omega t) \quad (2.1)$$

where k is the wave number given by

$$k = \frac{2\pi f}{c} \quad (2.2)$$

where f is the wave frequency and c is the speed of light. In order to satisfy the boundary conditions for a perfect conductor, the tangential electric field component E_y must be equal to zero at $z=0$ [Inan and Inan, 2000, p. 123]. Also, since a perfect conductor is lossless, the incident wave is completely reflected and the boundary has a reflection coefficient $R=-1$ for perpendicularly polarized waves. Thus, the electric

field of the reflected wave can be written as

$$E_y^r = -E_0 \exp\{-jk(x \cos \theta + z \sin \theta)\} \exp(j\omega t) \quad (2.3)$$

The reflected wave is also a plane wave with perpendicular polarization. The total electric field above the lower conductor is the sum of the two plane waves represented in Equations (2.1) and (2.3) and can be written as

$$E_y^{\text{tot}} = j2E_0 \sin(kz \sin \theta) \exp(\omega t - kx \cos \theta) \quad (2.4)$$

The boundary conditions for the perfect conductor at $z = h$ also require that E_y be equal to zero there as well. This condition can only hold true if

$$kh \sin \theta = n\pi \quad (2.5)$$

where n is an integer. Equation (2.5) shows that, for a given frequency, there are specific values of θ for which a plane wave with a total electric field E_y as given in (2.4) can exist, representing a wave reflecting back and forth between the plates and propagating in the x direction. The specific cases for which such waves can exist are known as *modes* and (2.5) is called the *mode equation* for a parallel plate waveguide with perfectly conducting boundaries. Another way of thinking about the condition (2.5) is that for a waveguide mode to exist the constituent uniform plane waves that constitute the mode must retain their planar fronts upon reflection from boundaries.

Waveguide modes made up of waves with perpendicular polarization are called Transverse Electric or TE modes since their electric fields are always transverse to the direction of propagation. TE mode waves have magnetic field components, H_x and H_z , in the x and z directions respectively. Waveguide modes also exist that are composed of waves with parallel polarization. Waves with parallel polarization have magnetic fields, H_y , in the y direction and electric fields, E_x and E_z , in the x and z directions. (The reflection coefficient for waves with parallel polarization incident on a perfect conductor is also $R = -1$.) Such modes are called Transverse Magnetic or TM modes since their magnetic fields are always transverse to the direction of propagation.

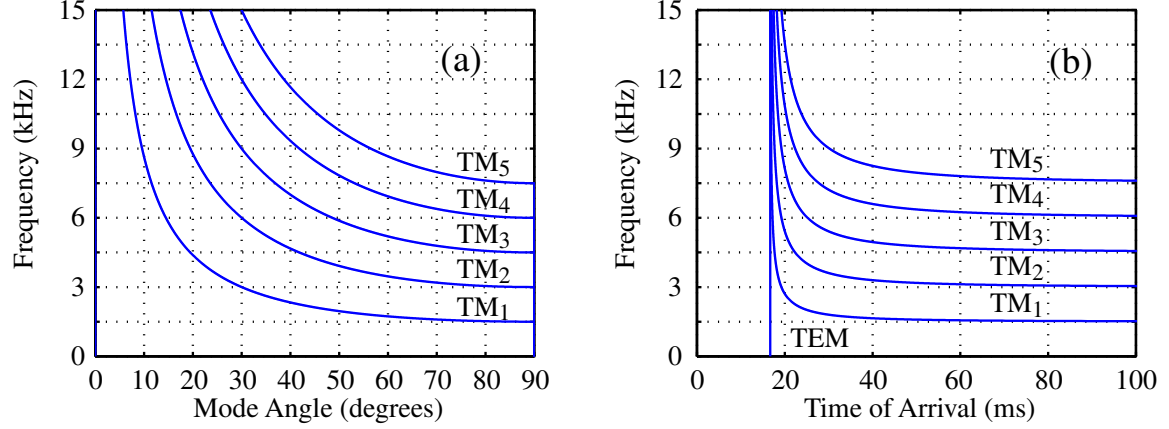


Figure 2.2: Mode-Frequency relationships in ideal waveguide with height $h = 100$ km. a: Mode angle versus frequency for first 5 waveguide modes. b: Group arrival time versus frequency for first 5 modes and TEM mode at a distance of 5000 km.

A special case of a TM mode has an electric field that is always parallel to the z -axis so that both the electric and magnetic fields are transverse to the direction of propagation. This mode is known as a transverse electromagnetic or TEM mode [Inan and Inan, 2000, p. 31].

Waveguide modes can be ordered by the values of θ for which they exist, with the mode having the lowest value of θ being the lowest order mode. For example, the lowest order TE mode is written as the TE₁ mode. Also, modes of different frequencies have different values of θ associated with them, as is obvious from (2.2) and (2.5). Figure 2.2a shows the variation of θ with frequency for the first five TM modes. Notice that, at specific frequencies, the curves flatten out as they reach 90°. At these frequencies, known as “cutoff” frequencies, waves do not actually propagate along the waveguide but the boundary conditions are met only by a wave reflecting back and forth between the top and bottom plates. When the frequency of a wave is below the cutoff frequency, the solution of (2.5) is only possible for complex values of θ (and thus $\cos\theta$), resulting in attenuation of the wave as can be seen from (2.4). These modes are known as evanescent waves [Inan and Inan, 2000, p. 196] and do not carry any real time-average power along the waveguide. The height h of the waveguide determines the cutoff frequency for each mode in accordance with $f_{cn} = nc/2h$. TEM

waves do not have a cutoff frequency since, in an ideal parallel plate waveguide, $\theta=0$ for all frequencies.

With the exception of the TEM mode, wave modes propagate back and forth between the waveguide boundaries at some angle θ so that the velocity of propagation of the energy carried by a mode through the waveguide is less than the speed of light. The phase velocity of propagation of waves of the form given in 2.5 depends on θ which, for a given mode (e.g., TM_n), is a function of frequency so that waves propagating along a parallel-plate waveguide are subject to dispersion. The group velocity of a waveguide mode is given by

$$v_g = c \cos \theta = c \sqrt{1 - (f_n/f)^2} \quad (2.6)$$

where f_n is the cutoff frequency for the n th order mode. It is apparent from (2.6) that as f approaches the cutoff frequency v_g goes to zero while as f becomes much larger than the cutoff frequency v_g approaches the speed of light. Once again, for f less than the cutoff frequency, the wave is evanescent and attenuates very rapidly with distance along the waveguide. Figure 2.2b illustrates what the received signal from an impulsive source (which excites TM wave energy in all of the modes) would look like after being dispersed in the waveguide. The TEM mode travels at the speed of light, with all frequencies arriving simultaneously. The TM_1 mode is dispersed and waves with frequencies near the TM_1 mode cutoff frequency arrive much later than the TEM mode. TM_1 mode frequencies further away from the cutoff frequency have group velocities much closer to the speed of light and arrive at nearly the same time as the TEM mode. Note that the TM_1 mode does not contribute any energy to the received signal at frequencies below its cutoff frequency. The same behavior occurs for higher order TM modes.

Even though the Earth-ionosphere waveguide is not an ideal parallel plate waveguide, the modal features just described are evident in signals received from impulsive sources. Figure 2.3 shows the frequency spectrum of two sferics (identified by the black arrows) detected in Upland, Indiana. The “tails”, also known as tweeks

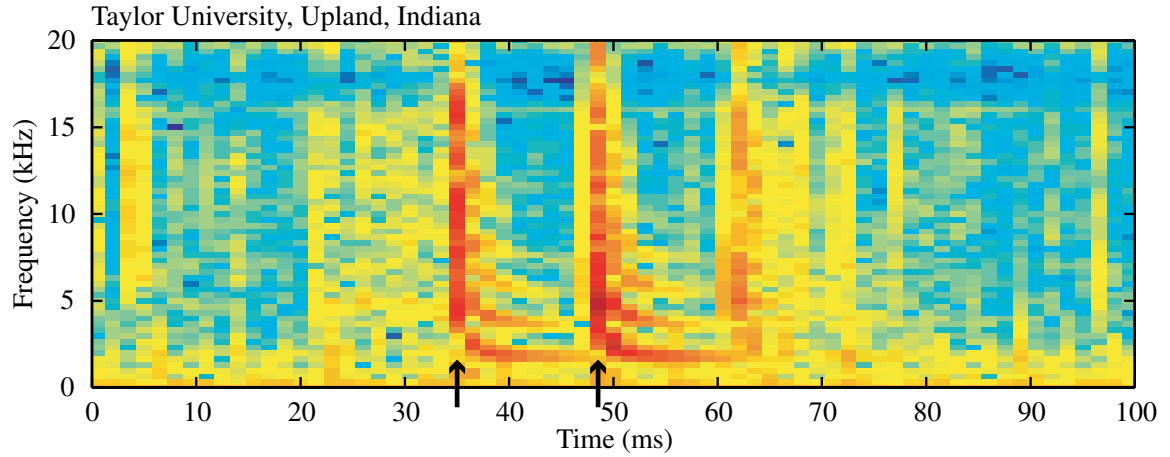


Figure 2.3: Sferic spectrum from Upland, Indiana showing twecks caused by the first five waveguide mode cutoffs.

[*Burton and Boardman, 1933*], of as many as five modes are visible in the spectrogram with cutoff frequencies at roughly 2, 4, 6, 8 and 10 kHz. These frequencies are indicative of a waveguide with a height of ~ 75 km.

2.2 Mode Excitation in a Parallel Plate Waveguide

2.2.1 Sferic Sources

The received signal from a sferic is also highly dependent on the source lightning current at which it originates. Of particular interest are waves that are excited by vertical currents, which occur in cloud-to-ground lightning flashes and portions of intra-cloud lightning, and horizontal currents, of the type manifested in other portions of intra-cloud lightning.

The simplest type of source is an infinitesimal current element known as a Hertzian dipole [*Budden, 1961*, p. 41] which consists of two opposite charges $\pm q$ connected by a wire of length l . In a true Hertzian dipole, q becomes infinitely large and l becomes infinitely small. To simplify the calculations of the electric and magnetic fields generated by a Hertzian dipole, another vector \mathbf{U} , known as the Hertz vector,

is used because the expressions involving \mathbf{U} are much simpler than those involving \mathbf{E} or \mathbf{H} directly [Stratton, 1941, p. 28]. The fields \mathbf{E} and \mathbf{H} can be derived from \mathbf{U} using the following expressions [Budden, 1961, p. 43]

$$\mathbf{E} = -\mu_0 \frac{\partial^2 \mathbf{U}}{\partial t^2} + \frac{1}{\epsilon_0} \nabla(\nabla \cdot \mathbf{U}) \quad (2.7)$$

$$\mathbf{H} = \frac{\partial}{\partial t} \nabla \times \mathbf{U} \quad (2.8)$$

For a linear source the Hertz vector is always parallel to the current source, so for a vertical source, one parallel to the z -axis, only the z component U_z of the Hertz vector is non-zero. To model a vertical electric line dipole with current I , the infinitesimal Hertz vector can be integrated over a distance l , the result of which is given by [Cummer, 1997, p. 18]

$$U_z = -\frac{kIl}{8\pi^2\omega} \int_C \exp[-jk(x \cos \theta + z \sin \theta)] \cos \theta d\theta \quad (2.9)$$

where θ is the angle in the x - z plane relative to the x axis and the harmonic term $\exp(i\omega t)$ has been dropped. The same can be done for a horizontal source except that the z component U_z of the Hertz vector is then zero while the x and y components U_x and U_y are non-zero such that \mathbf{U} is parallel to the source.

2.2.2 Excitation of Waveguide Modes

Now imagine placing the source described above into a parallel plate waveguide with perfectly conducting boundaries. As the waves radiated by the source interact with the boundaries, waveguide modes, such as the one depicted in Figure 2.2, are established. However, the relative field strength of a waveguide mode at some distance from the source depends on the propagation angle θ and on the source orientation.

Instead of accounting for all of the reflections from the conducting boundaries, Budden [1961, p. 59] uses the equivalence of the wave fields created by reflections to wave fields that would be created by the images of the source in the conductive boundaries. For example, a source at $z=0$ in a parallel plate waveguide is equivalent

to sources at $z=0, 2h, -2h, 4h, -4h, \dots$ with the plates removed, where h is the height of the waveguide. This equivalence leads to a source structure that is similar to the effect of an optical diffraction grating [Budden, 1961, p. 59].

By solving for the Hertz vector under these circumstances, several interesting results are obtained. First, in an ideal parallel plate waveguide, vertical sources excite only TM and TEM waveguide modes. The relative amplitudes of these modes are given by the so called excitation factors

$$\underbrace{1/2}_{\text{TEM}}; \underbrace{(\cos \theta_1)^{\frac{1}{2}} \cos(kz_1 \sin \theta_1)}_{\text{TM}_1}; \underbrace{(\cos \theta_2)^{\frac{1}{2}} \cos(kz_1 \sin \theta_2)}_{\text{TM}_2}; \dots; \underbrace{(\cos \theta_n)^{\frac{1}{2}} \cos(kz_1 \sin \theta_n)}_{\text{TM}_n} \quad (2.10)$$

where z_1 is the height of the source above the plate located at $z = 0$ and θ_n is the propagation angle for the n th mode. The term $\cos(kz_1 \sin \theta_n)$ is known as the “height gain” function for the source. An equivalent height gain term must also be used to account for the receiver height. However, in practical situations, the receiver is typically located at $z = 0$ (except in the case of aircraft or balloon based observations) and so the receiver height gain is usually equal to unity. Also, the TEM mode always has a gain of $1/2$ regardless of frequency.

In contrast to vertical sources, horizontal sources excite only TE waveguide modes in an ideal waveguide with perfectly conducting boundaries. Thus, horizontal sources do not excite TEM modes, meaning that they do not launch any propagating waves at frequencies below the first cutoff frequency. The relative amplitudes for the excited TE modes are given by the factors

$$\underbrace{(\cos \theta_1)^{-\frac{1}{2}} \sin(kz_1 \sin \theta_1)}_{\text{TE}_1}; \underbrace{(\cos \theta_2)^{-\frac{1}{2}} \sin(kz_1 \sin \theta_2)}_{\text{TE}_2}; \dots; \underbrace{(\cos \theta_n)^{-\frac{1}{2}} \sin(kz_1 \sin \theta_n)}_{\text{TE}_n} \quad (2.11)$$

where the height gain term is now $\sin(kz_1 \sin \theta_n)$. Note that a horizontal source located at $z_1 = 0$ in an ideal waveguide does not excite any waveguide modes since all of the height gain functions are zero. Physically, this occurs because any radiation produced by the source immediately above the perfectly conducting lower boundary is perfectly cancelled by the image immediately below.

2.3 The Earth-Ionosphere Waveguide

In many ways and under certain conditions, the Earth-ionosphere waveguide behaves very much like an ideal parallel plate waveguide. However, the electrical properties of the Earth, the ionosphere and the Earth's magnetic field cause significant deviations from this ideal model. Accordingly, we start our discussion of the Earth-ionosphere waveguide with a brief summary of the properties of its boundaries.

2.3.1 Properties of the Earth and Ionosphere

The major difference between an ideal waveguide and the Earth-ionosphere waveguide is that the Earth and ionospheric boundaries are not perfect conductors. The Earth has finite conductivity which varies over land and sea. For example, dry land typically has a conductivity σ in the range of 10^{-4} to 10^{-2} S/m and a relative permittivity $\epsilon \sim 3.4$ whereas seawater has a conductivity $\sigma = 4$ S/m and a relative permittivity $\epsilon = 81$ [Inan and Inan, 2000, p. 45]. Compared to a metallic conductor such as copper, which has a conductivity $\sigma = 5.8 \times 10^7$, the conductivity of the Earth is relatively low. However, at VLF frequencies, the land and sea can both be considered good conductors because $\sigma \gg \omega\epsilon$ [Inan and Inan, 2000, p. 54]. In general though, since the Earth is not a perfect conductor, waves propagating over a finitely conducting medium are subject to attenuation. The good conductor assumption particularly fails to hold true for ice, which has a conductivity $\sigma < 10^{-7}$ S/m. Thus, waves propagating over ice, such as the polar ice caps, are subject to much higher rates of attenuation [Rogers and Peden, 1975].

The upper boundary of the Earth-ionosphere waveguide is significantly different from a perfect conductor. The ionosphere is an ionized region of the upper atmosphere that contains significant numbers of free electrons and positive ions [Hargreaves, 1992, p. 208]. The ionosphere is subdivided into regions, designated D, E, F1 and F2, based on inflections in the electron density profile. The concentration of free electrons is caused primarily by solar radiation, such as ultraviolet and X-rays, during the day and maintained by non-solar radiation, such as cosmic rays and electron precipitation, at night [Hargreaves, 1992, p. 223]. Although the number density of electrons is small

compared to the number of neutral particles, the concentration of free electrons is high enough to make the ionosphere a good conductor at ELF and VLF frequencies.

Since solar radiation is the primary cause of ionization, there is a significant difference between the daytime and nighttime ionospheres. During the day, the D region can extend down to about 60 km where ionization begins. At night, due to recombination, the D region attenuates and the altitude at which significant ionization starts increases to about 80 km. Typical electron density profiles for day and night are given in *Hines et al.* [1965, p. 6]. As the electron density profile changes from day to night, so does the effective height of the Earth-ionosphere waveguide. The reflection height of the waveguide is dependent on the frequency and incidence angle of the oncoming wave. At normal incidence for VLF frequencies in a highly collisional system, the reflection height occurs at the point where

$$\omega_p^2 = \omega\nu \quad (2.12)$$

where ω is the wave angular frequency, ν is the electron collision frequency and ω_p is the plasma frequency given by

$$\omega_p = \sqrt{N_e(h)q^2/m_e\epsilon_0} \quad (2.13)$$

where $N_e(h)$ is the electron density height profile, q is the charge of an electron and m_e is the mass of an electron [Ratcliffe, 1959, p. 110]. From Equations (2.12) and (2.13) the electron density required for reflection of VLF waves ($f=3$ to 30 kHz and $\nu = 10^5\text{sec}^{-1}$) is calculated to be 20 to 60 cm^{-3} which is reached in the D region. In general, the electron density required for reflection of VLF waves decreases as the incidence angle θ (in Figure 2.2) decreases [Hargreaves, 1992, p. 27]. However, since the electron density initially increases very rapidly with altitude, this decrease has a minimal effect on reflection height. The calculated reflection heights are consistent with the experimental results of 63 km during the day [Rasmussen et al., 1980] and 85 km at night [Thomson, 1993].

The ionospheric waveguide boundary also diverges from a perfect conductor in that the presence of the Earth's magnetic field effectively renders the ionosphere an

anisotropic medium [Wait and Spies, 1960]. A result of this anisotropy is the fact that when an incident wave is linearly polarized with either parallel or perpendicular polarization the reflected wave is elliptically polarized with components that have both parallel and perpendicular polarization. A convenient way to think about this effect is to consider the reflection coefficient at the ionosphere boundary as a 2×2 matrix such as

$$\mathbf{R}_I(\theta) = \begin{bmatrix} {}_{\parallel}R_{\parallel}(\theta) & {}_{\parallel}R_{\perp}(\theta) \\ {}_{\perp}R_{\parallel}(\theta) & {}_{\perp}R_{\perp}(\theta) \end{bmatrix} \quad (2.14)$$

where the components ${}_{\parallel}R_{\parallel}$, ${}_{\parallel}R_{\perp}$, ${}_{\perp}R_{\parallel}$ and ${}_{\perp}R_{\perp}$ are the individual reflection coefficients for each combination of incident and reflected wave polarization and are, in general, complex. The reflection coefficient for the ground can also be written as a 2×2 matrix, except for the fact that the cross terms are equal to zero since the ground is generally not anisotropic

$$\mathbf{R}_G(\theta) = \begin{bmatrix} {}_{\parallel}\bar{R}_{\parallel}(\theta) & 0 \\ 0 & {}_{\perp}\bar{R}_{\perp}(\theta) \end{bmatrix} \quad (2.15)$$

The degree to which the anisotropy caused by the Earth's magnetic field is important depends on the relative values of the electron-neutral collision frequency, ν , and the electron gyro-frequency, ω_c , in determining the wave refractive index. The effects of the anisotropic ionosphere are most significant at night when the reflection height of the ionosphere is higher, reaching altitudes at which ν is comparable to ω_c . During the day the effect of the anisotropy is slight [Ferguson and Snyder, 1980, p. 5] since the reflection height is at lower altitudes where $\nu \gg \omega_c$. A remarkable effect caused by the presence of the geomagnetic field and the anisotropy is the difference in attenuation for propagation from West to East versus East to West. In general, waves travelling eastward experience less attenuation than waves travelling westward [Wait and Spies, 1960]. This difference was found to be greatest between 1-4 kHz where attenuation differences between eastward and westward propagation were observed to be greater than 45 dB/1000 km [Barr, 1971]. This effect is reduced as frequency is increased and the difference is only about 1 dB/1000 km for frequencies above 20 kHz [Wait and Spies, 1960]. A more general effect of the anisotropic ionospheric boundary is that, since the wave polarizations are coupled at the ionosphere,

pure TM and TE modes can not exist in the Earth-ionosphere waveguide as they do in an ideal parallel plate waveguide. Instead, the propagating energy is constituted by a superposition of quasi-TM or QTM and quasi-TE or QTE modes. QTM modes, for example, are similar to TM modes except that they have a small axial magnetic field component [Budden, 1961, p. 151] and the resulting correspondingly small additional transverse electric and magnetic field components that are not present in an ideal TM mode. The lower order quasi modes tend to be more pure than higher order modes, especially at frequencies less than 15 kHz [Snyder and Pappert, 1969].

2.3.2 Theory of Earth-Ionosphere Waveguide Propagation

Since the waveguide boundaries of the Earth and the ionosphere are non-ideal, the analysis of wave propagation in the Earth-ionosphere waveguide is considerably more complicated than that for ideal waveguides. Because of the fact that simple TM and TE modes no longer exist by themselves, the mode equation for an ideal parallel plate waveguide, as given by Equation (2.5), is no longer appropriate. For a waveguide mode to exist in any waveguide, the uniform plane waves that constitute the mode must retain their planar fronts upon reflection from both boundaries. For the Earth-ionosphere waveguide, this condition results in the mode equation

$$\mathbf{R}_I(\theta)\mathbf{R}_G(\theta)\exp(-2ikh\sin\theta) = \mathbf{I} \quad (2.16)$$

which is known as the fundamental equation of waveguide mode theory [Budden, 1961, p. 116] and where \mathbf{I} is the 2×2 identity matrix. Equation (2.16) is difficult to solve because the expressions for the elements of \mathbf{R}_I are complicated [Budden, 1961, p. 151]. Note that when the Earth and ionosphere are considered to be perfect conductors, Equation (2.16) condenses to the original mode equation (2.5).

Needless to say, the imperfect Earth-ionosphere boundary conditions also make the excitation and height gain functions much more complicated. However, if the mode angles θ_n and reflection coefficients are known, these height gain functions can be readily calculated. Pappert and Ferguson [1986] summarize the excitation factors and height gain functions formulated by Budden [1962] and expand the analysis to

account for an arbitrarily oriented dipole at a height z_t above the ground. The excitation factors given by *Pappert and Ferguson* [1986] are complicated functions of the reflection coefficient elements and mode angles and vary depending on the wave field of interest and the orientation of the exciting dipole. These height gain functions contain modified Hankel functions which cause the magnitudes of the height gain functions to oscillate with height similar to the manner which is represented by simple sines and cosines in the height gain functions for an ideal waveguide. The particular height gain function also depends on the wave field component of interest.

When the excitation factors, height gain function and dipole orientation are all taken into consideration, the equation for a general output field F can be written as [*Pappert and Ferguson*, 1986; *Cummer*, 1997]

$$F = C(F) \frac{ik^{3/2}Il}{\sqrt{8\pi x}} \exp(i\pi/4) \sum_n \Lambda_{tn} \Lambda_{rn} \exp(-ikx \sin \theta_n) \quad (2.17)$$

where $C(F) = \mu_0$ if F is a magnetic field component and $C(F) = \sqrt{\mu_0/\epsilon_0}$ if F is an electric field component. Λ_{tn} and Λ_{rn} are the combined excitation factor and height gain functions for the transmitter and receiver respectively. For an electric dipole oriented at an angle γ to the z -axis and at an angle ϕ to the direction of propagation and at a height z_t , the transmitter excitation factor Λ_{tn} is given by [*Pappert and Ferguson*, 1986; *Cummer*, 1997]

$$\Lambda_{tn} = -\tau_1 \sin(\theta_n) \cos(\gamma) f_1(z_t) + \tau_3 \tau_4 \sin(\gamma) \cos(\phi) f_2(z_t) + \tau \sin(\gamma) \sin(\phi) f_3(z_t) \quad (2.18)$$

where τ_1 , τ_3 , τ_4 , f_1 , f_2 and f_3 are defined by *Pappert and Ferguson* [1986]. The excitation factors Λ_{rn} are also given by *Pappert and Ferguson* [1986], which for the transverse magnetic field is simply the height gain function $f_1 z_r$ where z_r is the transmitter altitude. The Long Wave Propagation Capability (LWPC) software developed by the Naval Ocean Systems Center [*Ferguson et al.*, 1989] computes field values, F , for an arbitrary propagation path and ionospheric conditions along the path, including the effects of the Earth's magnetic field.

2.3.3 Correction for Curved Earth

The equations discussed thus far are applicable for a parallel plate waveguide. However, at large distances, the Earth-ionosphere waveguide can no longer be approximated as a parallel plate waveguide. In free space, the attenuation of field values due to spreading is proportional to r^{-1} where r is the 3-D distance from the source. This attenuation is equivalent to the $1/4\pi r^2$ spreading factor for wave power. For a parallel plate waveguide the field spreading factor is reduced to $r^{-1/2}$, where r is now the 2-D radial distance from the source, since the wave only spreads in two dimensions instead of three. For the Earth, which is really a spherical shell waveguide of radius R_E , the corresponding spreading factor is $[R_E \sin(s/R_E)]^{-1/2}$ where s is the great circle distance between the source and observation points [Budden, 1962]. Note that as $R_E \rightarrow \infty$ this spreading factor approaches $s^{-1/2}$, which is the cylindrical spreading factor for a parallel plate waveguide.

The mode equation (2.16) must also be modified due to the curvature of the Earth-ionosphere waveguide as the mode angles θ_n are valid for parallel surfaces and not spherical shells. A frequently used method for dealing with the curvature of the Earth mathematically is to model the refractive index of the atmosphere as a gradient $\mu = \exp(z/R_E)$ such that rays representing the plane waves bend upwards instead of travelling in straight lines [Budden, 1961, p. 140].

2.3.4 VLF Propagation Characteristics

A large number of numerical model calculations of VLF propagation in the Earth-ionosphere waveguide have been undertaken by Wait [1957], Wait and Spies [1960], Wait [1962], Snyder and Pappert [1969], Galejs [1972], Pappert and Ferguson [1986] and many others. These calculations reveal some interesting phenomena that arise for propagation in the Earth-ionosphere waveguide under realistic conditions. For example, the QTEM mode, the analog to the TEM mode, which is present for all frequencies in an ideal parallel plate waveguide, contributes little energy above ~ 1.2 kHz [Cummer, 1997] to the overall intensity of a radio atmospheric signal originating at a lightning discharge. Also, while the attenuation rate for VLF waves is low

in general, the attenuation rate generally decreases as frequency increases and is only a few dB/1000 km for frequencies greater than ~ 15 kHz [Wait, 1962]. (At still higher frequencies, the good conductor assumption, $\sigma \gg \omega\epsilon$, is no longer valid causing the waveguide boundaries to become lossy resulting in higher attenuation [Inan and Inan, 2000, p. 54].) In contrast to this, lower frequencies are more readily excited and the excitation factor (2.18) generally decreases as frequency increases [Wait, 1962]. Thus, as a wave propagates over a greater distance the ratio of energy at higher frequencies to lower frequencies should, in principle, increase. However, excitation and attenuation vary significantly with the parameters of the waveguide, such as reflection height, ground conductivity and anisotropy, which change over time and over the typically long VLF propagation path [Wait, 1957]. As mentioned previously, due to the anisotropic boundary at the ionosphere, waves travelling westward are attenuated more than waves travelling eastward [Snyder and Pappert, 1969]. In addition to this higher attenuation, west bound wave modes have a higher level of “quasiness” than east bound modes. That is to say the QTM modes propagating west have relatively larger longitudinal magnetic field components than the QTM modes propagating east, especially for frequencies less than ~ 15 kHz [Snyder and Pappert, 1969].

Another interesting result occurs due to the fact that the Earth-ionosphere waveguide is not homogeneous over an entire propagation path. Discontinuities in the waveguide parameters, such as an abrupt change in the ground conductivity or a change in the reflection height of the ionosphere can cause energy in one waveguide mode to be converted over to another waveguide mode. This effect is most apparent when the propagation path crosses the day/night terminator. When such a crossing occurs, a single mode propagating from the daytime side of the terminator is readily seen to convert into two modes on the nighttime side of the terminator [Ferguson and Snyder, 1980]. Since all of the processes described above can affect the waveforms of sferics as they propagate through the Earth-ionosphere waveguide, they should be kept in mind when undertaking analysis of sferics arriving at a receiver from distant source points.

Chapter 3

Sferic Detection and Direction Finding

3.1 Data Acquisition

VLF electromagnetic signals used in this dissertation are detected and recorded using Stanford University ELF/VLF radio receivers. A block diagram of a standard system is shown in Figure 3.1. Each receiver system consists of two orthogonally crossed magnetic loop antennas, a pre-amplifier, a line receiver, a Global Positioning System (GPS) clock and an analog to digital converter for storing waveforms on digital media. Since it is desirable to detect sferics generated both nearby and far away ($\sim 12,000$ km) a suitable VLF receiver should have a large dynamic range and should be situated in a low noise environment. If the dynamic range is too small, then high amplitude nearby sferics saturate the receiver electronics and clip the sferic waveforms. If, on the other hand, the noise environment is too severe, then low amplitude sferics arriving from far away source points are not detectable beneath the noise floor. Furthermore, since the frequency content of typical radio atmospherics spans the entire ELF/VLF band, it is desirable to have a flat frequency response over a large range. However, because of 60 Hz hum (with harmonics) from power lines, the frequency response is often kept low for frequencies below a few hundred hertz.

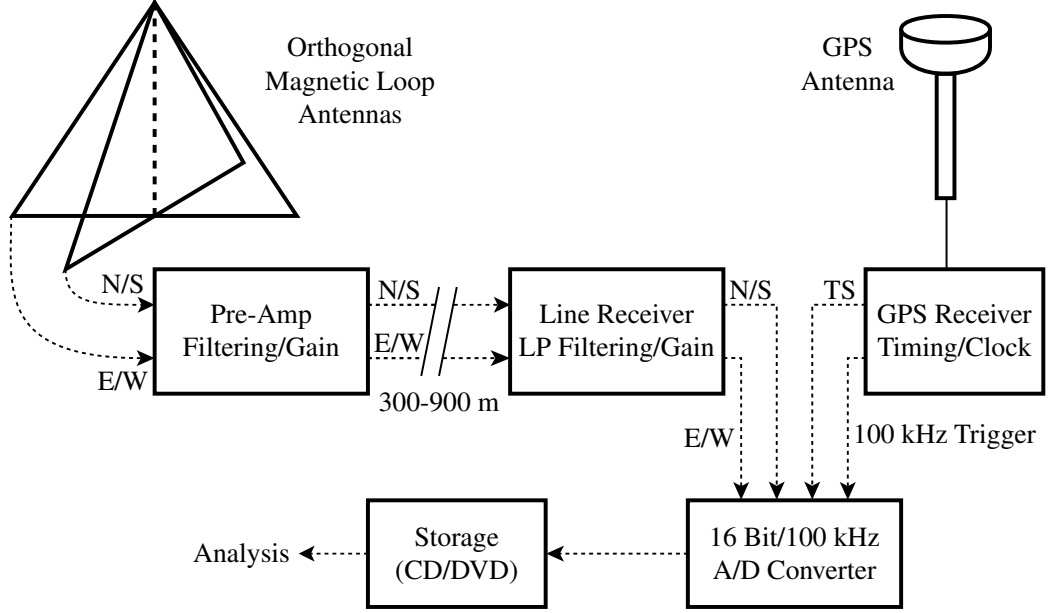


Figure 3.1: Typical VLF Receiver System

3.1.1 Magnetic Loop Antenna

The magnetic loop antennas used in the typical Stanford University VLF receiver consists of N turns of wire with an air core, where N ranges from 1 to 6 for the receivers used in this dissertation. As an electromagnetic wave impinges on the antenna, a voltage is induced in the loop due to the changing magnetic field within the loop [Ramo *et al.*, 1994, p. 116-117]. Faraday's law says that the induced voltage is equal to the time rate of change of the magnetic field through the loops which is given by

$$V = -N \frac{\partial}{\partial t} \int \mathbf{B} \cdot d\mathbf{A} \quad (3.1)$$

where V is the induced voltage and N is the number of turns in the antenna. In general, the induced voltage increases with increasing frequency. However, if the input impedance of the line receiver is correctly matched to the impedance of the antenna then the output voltage can be made independent of frequency over a limited range [Pascal, 1988].

Most receiver sites have two orthogonal antennas designated as North/South

(N/S) and East/West (E/W) based on the direction of the baseline of the antenna. Historically the N/S antenna was aligned with the Earth’s geomagnetic field, typically using a magnetic compass. Thus, the direction of the N/S is offset from true geographic North by the local declination angle of the Earth’s geomagnetic field. With the advent of the Global Positioning System (GPS), antennas can now be aligned precisely to geographic latitude and longitude lines although magnetic alignment is still used when GPS measurements are unavailable.

The shape and size of the antenna used at a particular receiver site depends mostly on the conditions and logistical support at the site itself. For example, a permanent site such as Palmer Station, Antarctica can support a masted $20\text{m} \times 10\text{m}$ single turn triangular antenna which with a matched preamplifier provides high sensitivity ($S_o = \sim 1 \times 10^{-8} \text{ VHz}^{-1/2}\text{m}^{-1}$ at 10 kHz). Whereas at a temporary receiver site, such as the one located on Vieques Island off the coast of Puerto Rico, it is more convenient to use a small $4.9\text{m} \times 4.9\text{m}$ six turn square antenna which provides a somewhat lower sensitivity ($S_o = \sim 5 \times 10^{-8} \text{ VHz}^{-1/2}\text{m}^{-1}$ at 10 kHz). In general, the larger the area of the antenna, the higher its sensitivity [Pascal, 1988]. However, it should be noted the sensitivity of both of these types of antenna-preamp systems is substantially ($\sim 20\text{dB}$) better than the atmospheric noise levels (due to totality of lightning) even at the quietest sites, so that measurement sensitivity is not limited by system sensitivity.

3.1.2 Pre-Amplifier and Line Receiver

The pre-amplifier and line receiver take the induced voltage at the antenna terminals and condition it via filtering and amplification for digitization by the analog to digital converter. Typically, the antennas are placed at a distance of up to ~ 2000 ft from sources of power line noise, such as buildings, etc., and the pre-amp is placed near to the antennas such that it has access to the VLF signal directly from the antenna leads. The pre-amp is powered over a cable of ~ 2000 ft length, which also serves as the signal cable carrying the amplified signals back to the line receiver. The pre-amp contains gain stages and a high pass filter to prevent 60 Hz “noise” from saturating the

amplifiers. In addition to amplifying and filtering the signal, the pre-amp consists of a matching input transformer, a differential amplifier and a line driver. The matching input circuit allows for a flat frequency response and high sensitivity over a wide bandwidth by compensating for the frequency dependent gain of the antennas. The line driver, which is powered by a DC source from the line receiver, allows the antennas to be removed from the AC power source of the line receiver by up to 2000 ft.

In addition to powering the pre-amp, the line driver further filters and amplifies the VLF signal. The low pass filter has a -3 dB point at ~ 22 kHz. This filtering scheme was implemented because, historically, the signal was digitized using audio recording equipment which has a standard sampling frequency of 44.1 kHz [Reising, 1998]. As an example, the full frequency response for the combination of the pre-amp and line receiver at Palmer Station, Antarctica is shown in Figure 3.2. On the low side, the -3 dB point occurs at ~ 300 Hz and at ~ 22 kHz on the high side.

3.1.3 Analog to Digital Conversion

Once the VLF signal has been conditioned by the pre-amp and line receiver, it is digitized by an A/D converter and recorded to digital media. The A/D converters used in modern systems are usually National Instruments data acquisition cards that allow both N/S and E/W channels to be sampled at 100 kS/s with 16 bit precision providing a 50 kHz bandwidth and nearly 100 dB of dynamic range respectively. To prevent clipping at the A/D, the gain of the pre-amp and line receiver should be adjusted such that the output voltage of the line receiver falls between ± 5 volts.

In order to realize the most precise timing possible, the sampling is controlled by a TrueTime brand GPS clock. The GPS clock has a 100 kpps output that is used as the sampling trigger and a 1 pps start trigger that is accurate to 200 ns. In this way data from different receiver locations can be correlated in time with each other.

The A/D cards are not capable of sampling two channels simultaneously at 100 kS/s but rather sample both channels together at 200 kS/s. That is to say the N/S channel is sampled followed by the E/W channel then followed by the N/S channel again such that each channel is sampled 100,000 times per second. Because of this

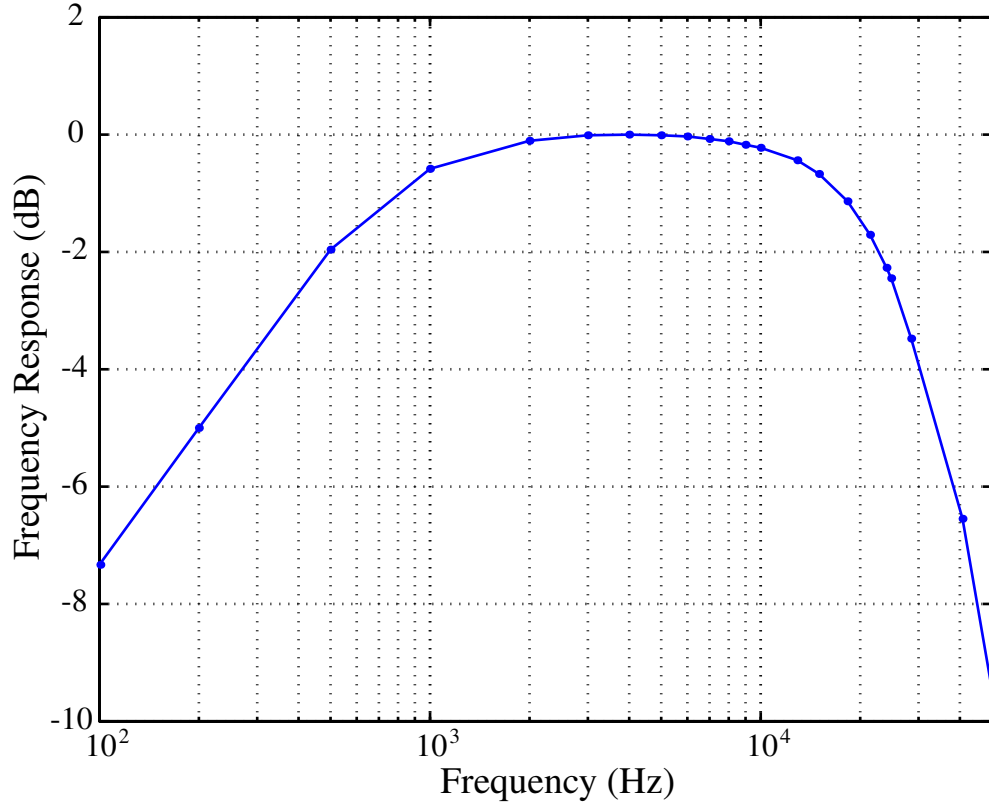


Figure 3.2: Frequency Response of VLF Receiver at Palmer Station, Antarctica

feature of the A/D card the E/W channel is effectively offset from the N/S channel by half a sample. This offset is compensated for by using the shift theorem of the Fourier transform which states that a shift in time is equivalent to multiplication by

$$\exp\left(\frac{-i2\pi f}{f_s}\right) \quad (3.2)$$

in the frequency domain where f_s is the total sampling frequency, which, in most cases, is 200 kS/s, thus resulting in a time shift of 5 microseconds.

Some of the data used in this dissertation was recorded on BETAMAX magnetic video tape using a Sony PCM 601-ESD encoder. Data of this type was recorded along with an IRIG-B time signal with a resolution of 1 ms and the timing is therefore not as precise as that for data recorded using the National Instruments A/D cards. This

BETAMAX recording scheme is described in more detail by *Reising* [1998].

3.2 Sferic Detection

As is visible in Figure 1.2, the electromagnetic environment in which individual sferics are to be detected is inundated by large numbers of sferics originating at sources worldwide as well as by magnetospheric signals, such as whistlers, and by anthropogenic sources. On the low end of the spectrum, the ever present 60 Hz power line hum and harmonics are visible and on the high end of the spectrum the Omega (though now decommissioned) and Alpha transmitters along with the VLF naval transmitters act as narrowband noise sources [*Burgess*, 1993]. Also, the sum total of all sferics arriving from all directions originating from all lightning sources around the world act as a broadband noise source. Thus, a sophisticated algorithm is necessary to detect and analyze the impulsive broadband sferic waveforms. Fortunately, much of the energy of a sferic lies in the 5-15 kHz band [*Cummer*, 1997] of which a 4 kHz band is usually used for sferic detection.

3.2.1 Detection Filtering

Figure 3.3a shows the raw broadband data for a typical sferic recorded at Palmer Station, Antarctica on August 28, 1997. In this particular case the amplitude of the E/W channel signal is greater than the amplitude of the N/S channel signal, indicating that the sferic is arriving from a more eastward (or westward) than northward direction (assuming a lack of sources south of the site due to lack of lightning in Antarctica and large attenuation over the polar cap). The main impulse of the sferic lasts about one millisecond but an ELF slow tail is also present which continues for many more milliseconds [*Reising et al.*, 1999]. The ELF slow tail suggests that this particular sferic may be associated with the production of an atmospheric upward discharge known as a sprite [*Reising et al.*, 1999].

The first step in isolating a sferic waveform is to filter the broadband signal around the frequency band of interest. Figure 3.3b shows the raw data after being bandpass

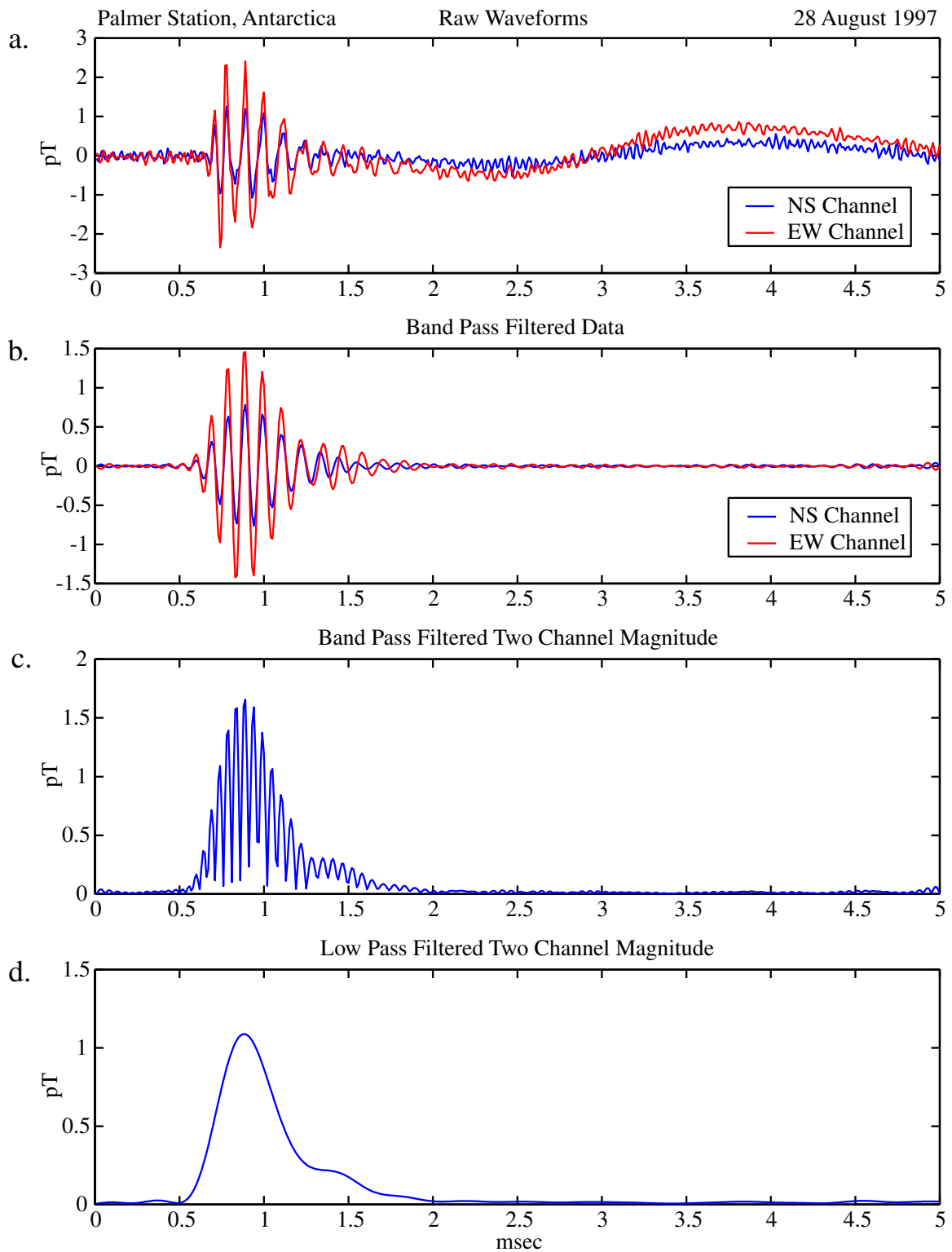


Figure 3.3: Stages of Sferic Detection Algorithm

filtered with a pass band of 9 – 13 kHz. Butterworth filters are used since they have a maximally flat pass band and a high roll off rate with a low order filter. Butterworth filters are not ideal in that they have a nonlinear phase response. However, since the filtering is being performed in post processing and not in real time, the phase relationships between the frequencies can be preserved by first filtering the data in the forward direction and then filtering the data in the reverse direction. This procedure in effect creates a zero phase filter with a magnitude response that is the square of the original frequency response. Notice that the filtered signals from the E/W and N/S are in phase up until ~ 1.3 ms when the phase of the E/W channel begins to lag behind the phase of the N/S channel. This effect is probably due to the arrival of a smaller sferic in the E/W direction which overlaps with the larger sferic and contaminates its waveform.

Also notice that the filtered signal in Figure 3.3b is still highly oscillatory in nature. In an attempt to create a single peak for each sferic, the absolute magnetic field of the incident wave is calculated by

$$B = \sqrt{B_{NS}^2 + B_{EW}^2} \quad (3.3)$$

and is displayed in Figure 3.3c. Squaring the magnetic field values is essentially equivalent to performing an autocorrelation in the frequency domain which generates new frequency components around 0 Hz and in this case up to ~ 4 kHz, which is the bandwidth of the filtered signal. Higher frequency components are also created and are centered at twice the center frequency of the filtered signals bandwidth. The absolute magnetic field signal is then low pass filtered, as shown in Figure 3.3d, which smooths the signal into a single peak. Unfortunately a single peak is not always achieved so an additional constraint is imposed on the detection process such that the subsequent sferic can not be detected within 2 ms of a previously detected one. In other words, sferics that are not sufficiently separated in time (i.e., by ~ 2 ms or more) from other sferics are not included in our analysis.

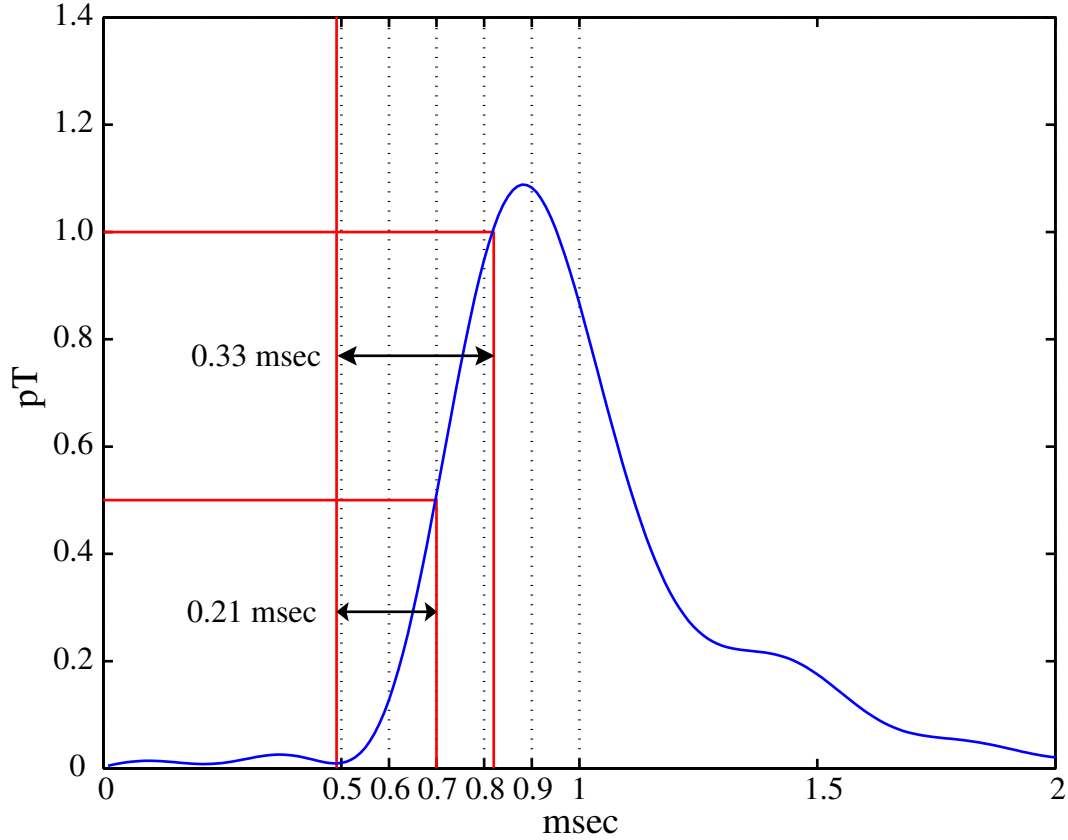


Figure 3.4: Time of Arrival Dependence on Threshold Setting

3.2.2 Time of Arrival Determination

Now that a data stream has been created where each sferic is represented as a single peak, the individual arrival times for each sferic must be extracted. To reduce geolocation errors, it is usually desirable to detect only those sferics whose maxima exceed a certain threshold. Figure 3.4 shows two different thresholds, one at 1 pT and the other at 0.5 pT. Notice that the two threshold values cross the peak at different times. The 1 pT threshold crosses the peak 0.33 ms after the onset of the rise while the 0.5 pT threshold crosses the peak 0.21 ms after the onset of the rise. Thus, the point where the sferic peak crosses the threshold value is not an appropriate representation of the sferic arrival time. This realization leaves either the maximum point of the

peak or the inflection point at the start of the peak as possible points of indication of the arrival time. Since the Earth-ionosphere waveguide is a dispersive medium [Equation (2.6)] the impulsive sferic waveform spreads out in time as it propagates through the waveguide [Budden, 1961, p. 79]. Therefore, the time of the maximum value of the envelope shifts further away from the onset time the farther it travels in the waveguide. Thus, the best point to set the sferic arrival time is at the inflection point at the start of the peak, which is at ~ 0.5 ms in Figure 3.4. In this way the arrival time is relatively independent of the threshold value, the strength of the sferic and the degree to which the sferic is dispersed. Another method of calculating the arrival time of a sferic, known as time of group arrival, is discussed by Dowden [2002].

3.3 Direction Finding

Once a sferic is detected and its arrival time is determined, its arrival azimuth can be calculated using magnetic direction finding in the Fourier domain. This determination is accomplished by using a weighted average of the arctangent of the ratio of the voltage across the E/W antenna terminals to the voltage across the N/S antenna terminals over a desired frequency range. In the continuous frequency domain the arrival azimuth is given by

$$\theta_{\text{calc}} = \frac{\int_{f_1}^{f_2} \arctan \left(\frac{|B_{\text{EW}}(f)|}{|B_{\text{NS}}(f)|} \right) B_{\text{total}}(f) df}{\int_{f_1}^{f_2} B_{\text{total}}(f) df} \quad (3.4)$$

where $B_{\text{EW}}(f)$ and $B_{\text{NS}}(f)$ are the Fourier transforms of the E/W antenna and N/S antenna time domain signals and

$$B_{\text{total}}(f) = \sqrt{B_{\text{EW}}(f)^2 + B_{\text{NS}}(f)^2} \quad (3.5)$$

Actual computation of the arrival azimuth is performed in discrete frequency space, in which these equations take on the form

$$\theta_{\text{calc}} = \frac{\sum_{n=1}^N \arctan\left(\frac{|B_{\text{EW}}[n\Delta f]|}{|B_{\text{NS}}[n\Delta f]|}\right) B_{\text{total}}[n\Delta f]}{N \sum_{n=1}^N B_{\text{total}}[n\Delta f]}; \quad N\Delta f = f_2 - f_1 \quad (3.6)$$

where Δf is the frequency resolution, $B_{\text{EW}}[n\Delta f]$ and $B_{\text{NS}}[n\Delta f]$ are the FFT's of the E/W antenna and N/S antenna discrete time signals and

$$B_{\text{total}}[n\Delta f] = \sqrt{(B_{\text{EW}}[n\Delta f])^2 + (B_{\text{NS}}[n\Delta f])^2} \quad (3.7)$$

The frequency band used for azimuth determination usually lies between ~ 5 -15 kHz since the peak signal strength for sferics occurs around 10 kHz [Cummer, 1997]. The bandwidth $f_2 - f_1$, is usually about 4 kHz as it is generally agreed that averaging over a bandwidth of a few kilohertz substantially reduces systematic azimuth errors [Strangeways and Rycroft, 1980]. Also, the azimuth determined using this technique is ambiguous to within 180° since the Poynting vector can not be determined uniquely with only magnetic field measurements.

The direction finding technique described above is based on the underlying assumption that the detected sferics are predominantly composed of transverse magnetic (TM) waveguide modes. In other words, the technique is applied with the implicit assumption that the arrival azimuth of a sferic can be accurately determined by measuring the horizontal magnetic field component of the incoming wave. Since the magnetic field components of TM waves are transverse to the direction of propagation in the waveguide, the arrival azimuth is along the direction perpendicular to the magnetic field vector in the plane parallel to the ground.

Transverse Magnetic mode waves are preferentially excited by vertical lightning currents [Budden, 1961, p. 61], such as that which occurs in CG lightning discharges, which tend to be vertical near the ground [Krider *et al.*, 1976], and the vertical portions of IC lightning discharges. Horizontal discharges, such as those found in IC

lightning [Krehbiel, 1986], preferentially excite transverse electric (TE) mode waves [Budden, 1961, p. 64]. (It should also be noted that the excitation of TE mode waves from a horizontal source is dependent on the orientation of the source relative to the observer, and the height of the source above the ground.) The orientation of the magnetic field of TE mode waves is perpendicular to the magnetic field of TM mode waves. Thus, the horizontal magnetic field component of TE mode waves is parallel to the direction of propagation. Therefore, the application of the direction finding technique which presumes TM waves to sferics that are predominantly composed of TE mode waves results in an error in azimuth of 90° . Furthermore, for low order TE modes, the magnetic field is primarily vertical and therefore the magnitude of the detected sferic appears substantially smaller than that of an equally energetic sferic composed primarily of TM mode waves.

3.4 Polarization and Quasi-mode Errors

As mentioned previously, sferics are not composed of idealized TM mode waves but are rather composed of a sum of quasi-TM (QTM) and quasi-TE (QTE) modes that deviate from ideal TM and TE modes due to the finite conductivity of the Earth and the ionosphere, the anisotropy of the ionosphere and the curvature of the earth [Martin, 1965]. Also, since higher order modes are subject to higher attenuation than lower order modes [Snyder and Pappert, 1969], the lower order modes become more dominant as the distance from the source increases. Errors in the derived azimuth angle that are caused by deviations from ideal TM waves are typically referred to as polarization errors. Yamashita and Sao [1974 a,b] discuss in more detail some of the manifestations of polarization error, such as the effects of waveguide characteristics and of source polarization. The magnitude of the error depends on frequency and also oscillates as the distance from the source changes. The polarization of the source causes more erratic variations in the azimuth error as a function of distance, with the error generally increasing as the source becomes more horizontal and in line with the receiver direction. Also, errors can be particularly high when the receiver is within a few hundred kilometers of the source [Uman *et al.*, 1980].

In general, polarization errors are functions of frequency and decrease with increasing distance from the source or a local anisotropy or inhomogeneity. For receivers at great distances from sources, polarization errors are small for three reasons. First, for frequencies less than ~ 15 kHz, the lowest order QTM and QTE modes have the lowest attenuation [Snyder and Pappert, 1969]. Therefore, at great distances, these modes are dominant. Second, for vertical discharges, QTM modes are excited to a much greater degree than QTE modes [Snyder and Pappert, 1969]. Thus, even though the lowest order QTE mode has a low attenuation rate, it is not excited as much as the lowest order QTM mode, and at great distances the QTM mode is dominant. Finally, the lowest order QTM mode is the least “quasi” of the modes [Snyder and Pappert, 1969]. That is to say, the lowest order QTM mode is closer to being a pure TM mode than the higher order modes, although the level of “quasi-ness” does depend on the direction of propagation.

3.5 Site Error Correction

Error in the arrival azimuth calculation can also be caused by the properties of the receiver site. Appropriately referred to as “site error”, this type of azimuth error is different for each site but is a calculable constant for any given azimuth and can therefore be removed in post-processing [Mach *et al.*, 1986]. The characteristic feature of site error is the presence of two cycle sinusoidal variations in error with respect to arrival azimuth [Hiscox *et al.*, 1984]. This variation is usually attributed to the topography of the surrounding terrain, such as nearby hills and elevation changes [Horner, 1954] or to nearby metallic objects and structures [Hiscox *et al.*, 1984, Mach *et al.*, 1986, Passi and Lopez, 1989], and is often minimized with the use of some type of statistical algorithm. However, imperfections in the alignment and size and shape of the two magnetic loop antennas can also cause a sinusoidal variation in azimuth error.

The antennas of the type used in the experiments pertinent to this dissertation are imperfect in several ways. First, the N/S aligned antenna does not align perfectly with geographic North but is offset by some angle, ρ . Second, the antennas are not perfectly orthogonal but are skewed from orthogonality with respect to one

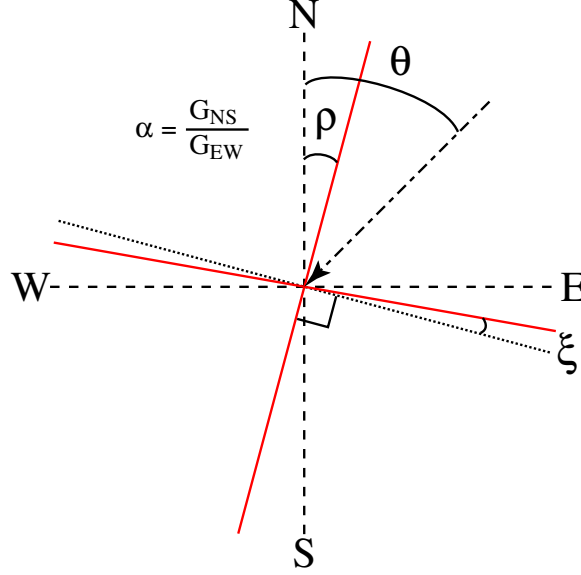


Figure 3.5: Antenna Distortion Parameters

another by some angle, ξ . Finally, the dimensions of the two loops may be different, resulting in different areas, which causes the induced voltage at the terminals of the antennas to be different for the same incident magnetic field intensity. The antenna response differences can be combined with any other differences in system gain (i.e., in the preamplifier circuitry) to determine the total gain of both the N/S and E/W channels. Using the geometry depicted in Figure 3.5, the azimuth error caused by imperfections in the dimensions of the antenna and its alignment can be corrected. Given a calculated arrival azimuth, θ_{calc} , the true arrival azimuth θ_{true} can be calculated using the following equation

$$\theta_{\text{true}} = \arctan \left[\alpha \frac{\tan(\theta_{\text{calc}})}{\cos(\xi)} - \tan(\xi) \right] + \rho \quad (3.8)$$

where α is the ratio of the gain in the N/S channel to the gain in the E/W channel, $G_{\text{NS}}/G_{\text{EW}}$. This equation is derived in Appendix A.2. The variables ρ , ξ and α vary from receiver site to receiver site and θ_{calc} , of course, varies from event to event. Figure 3.6 demonstrates how the correction curves change as these parameters vary.

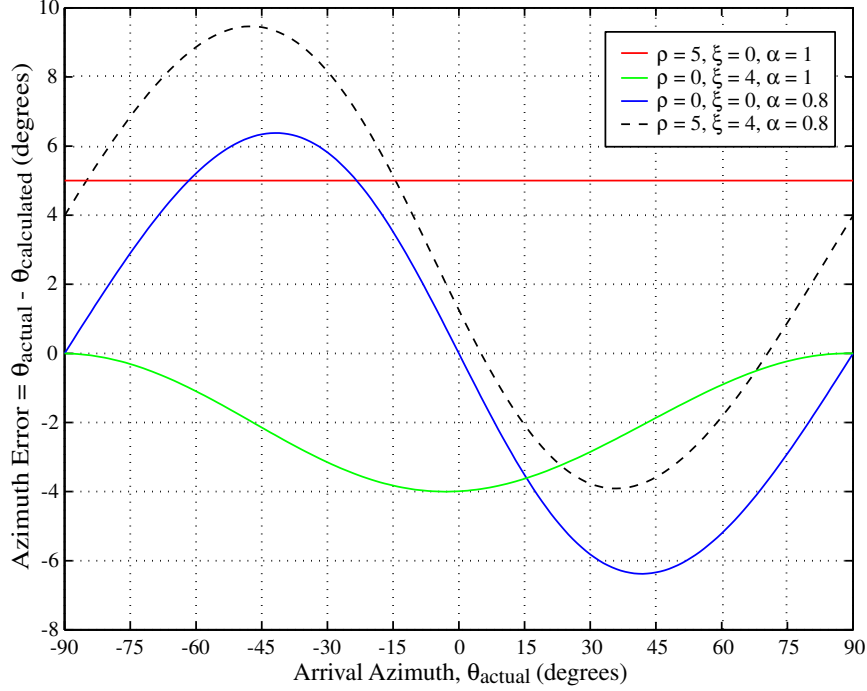


Figure 3.6: Example Site Error Correction Curves

3.6 Arrival Azimuth Verification

In all of our analyses in this dissertation, it is implicitly assumed that a sferic reaches a receiver by travelling along the shortest path from its source, which on a sphere is a great circle. Thus, the arrival azimuth of a sferic identifies the great circle path that it has propagated on. Figure 3.7 shows selected great circle bearings from North America to Palmer Station, Antarctica, located $\sim 12,000$ km away (64.77° S, 64.05° W). Some of these paths, such as the -40° bearing, are predominantly over the sea, while others, such as the -10° bearing, cross multiple land/sea boundaries. These differences are important because they affect the attenuation rate and mode structure of the signal, both of which play a role in the calculation of the arrival azimuth [Wait, 1968].

The performance of the direction finding algorithm is evaluated by matching sferics to their causative lightning discharges located by more established systems such as

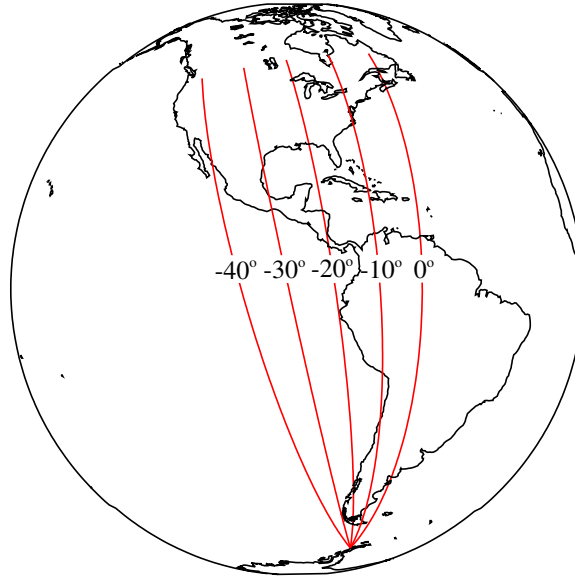


Figure 3.7: The lines labelled -40° to 0° represent great circle paths from North America to Palmer Station, Antarctica.

the NLDN or LIS. Figure 3.8 shows the locations of cloud-to-ground lightning flashes detected by the NLDN from 0100-1000 UT on 28 August 1997. The flash locations are accurate to ~ 0.5 km [Cummins *et al.*, 1998] which, at a distance of $\sim 5,000$ km, corresponds to an azimuth accuracy of ~ 0.006 degrees. This accuracy is well beyond the resolution of the direction finding system used here, so that, for the purposes of this dissertation, the locations can be considered to be exact. For the day shown in Figure 3.8, major storm centers are located off the coast of Florida, across the northeast, in the northern Midwest and along the Gulf of California. Smaller storms are also present, such as the one off the coast of Louisiana along a bearing from Palmer Station of about -22° .

Sferics detected at VLF receiver sites are often matched on a one-to-one basis to cloud-to-ground flashes detected by the NLDN. However, as mentioned in Chapter 1, individual sferics are generated by the return strokes of lightning flashes [Uman, 1987, p. 110-120]. Nevertheless, the matching of sferic times with NLDN recorded flash times is appropriate because the flash times provided by the NLDN are specifically the times of the first return strokes of flashes. Also, the radiated power of first

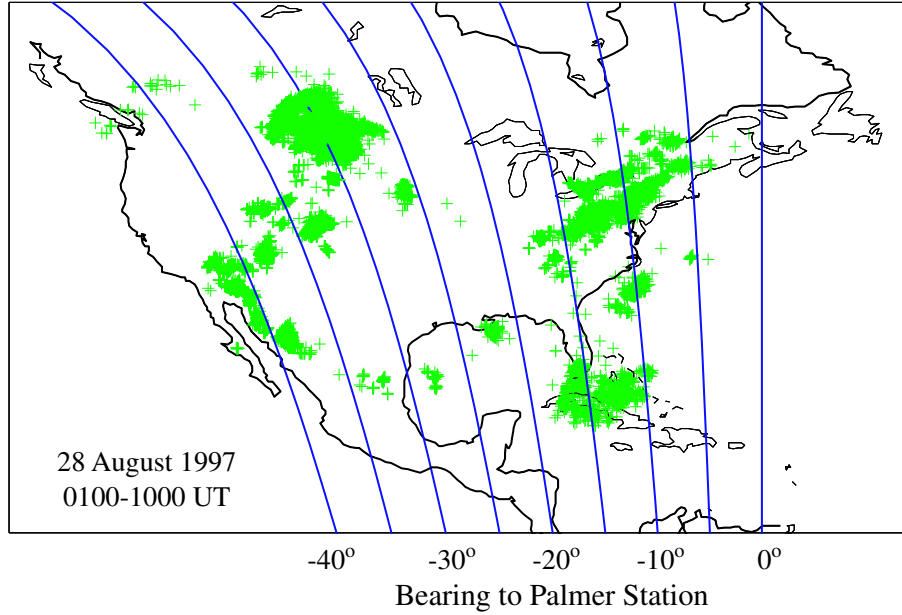


Figure 3.8: Each green cross represents the location of an NLDN cloud-to-ground lightning flash and the lines represent the great circle paths to Palmer Station.

return strokes typically exceeds that of subsequent strokes by a factor of $\sim 2-5$ [Uman, 1987; Krider and Guo, 1983]. Therefore, for distant receiver sites such as the one located at Palmer Station, sferics generated by first return strokes are more likely to be detected in the presence of the attenuation over the long path. In any case, comparisons to NLDN flashes, for the purposes of this dissertation, should be understood to be comparisons to the first return strokes of those flashes.

Sferics are time-matched to their causative lightning discharges by first computing the expected propagation time from a lightning source to a receiver. Equation (2.6) shows that the group velocity of a waveguide mode depends on the cutoff frequency for that mode which is a function of the waveguide height. Thus, as the reflection height of the Earth-ionosphere waveguide changes over the course of the day, so does the group velocity. However, for low-order modes at frequencies away from the cutoff frequency, propagation through the waveguide occurs at near the speed of light. For example, the difference in propagation time over a 10,000 km path between daytime

propagation (~ 60 km reflection height) and nighttime propagation (~ 80 km reflection height) is only $\sim 280 \mu\text{s}$ at 13 kHz. Therefore, the arrival time of a sferic at a receiver site can be calculated with better than ~ 1 ms accuracy without knowledge of the reflection height of the waveguide.

For lightning flashes in North America, propagation to Palmer Station takes $\sim 30-40$ ms depending on the location of the flash. For the purposes of comparison, any sferic arriving within 1.5 ms of the expected arrival time of a sferic radiated by an NLDN detected flash is considered to constitute a match for that flash. The arrival azimuth of each sferic is computed and corrected for site error ($\rho=4.0^\circ$, $\xi=2.4^\circ$ and $\alpha=0.90$ for Palmer Station 2001 calibration). For sferics matched to NLDN flashes, the arrival azimuth error is defined as the difference between the azimuth predicted using NLDN locations and the azimuth calculated at Palmer Station. Figure 3.9 shows a histogram of arrival azimuth errors for sferic detected at Palmer Station over a 9-hour period from 0100-1000 UT on 28 August 1997. During this period, 2771 sferics were matched to NLDN flashes. Of these sferic azimuths, 60.5% are accurate to within 1° while 80.3% are accurate to within 2° . The overlying curve in Figure 3.9 is a Gaussian with a mean of 0 and a standard deviation of 1. The high degree of correlation between the curve and the histogram suggest the error is dominantly random in nature and that the direction finding method is effective after subtraction of systematic site errors. The exception to this are the histogram bars from $\sim 2-5^\circ$ that rise above the Gaussian curve. These errors are likely the result of polarization or quasi-mode errors.

The detection efficiency at a receiver site can also be estimated using NLDN data. At Palmer Station, results show that the minimum field strength amplitude for which the azimuth of a sferic can be correctly determined (within 5°) is $\sim 250 \mu\text{V/m}$. This threshold value roughly corresponds to the detection of a lightning discharge with a peak current of ~ 10 kA at a range of $\sim 10,000$ km. The top panel of Figure 3.10 shows the predicted azimuths for all NLDN flashes detected during 0100-1000 UT on 28 August 1997 while the middle panel shows only the azimuths for sferics detected at Palmer Station that were matched to NLDN flashes. Notice that highest detection efficiency occurs for sferics arriving at -39° with $\sim 40\%$ of flashes being matched to

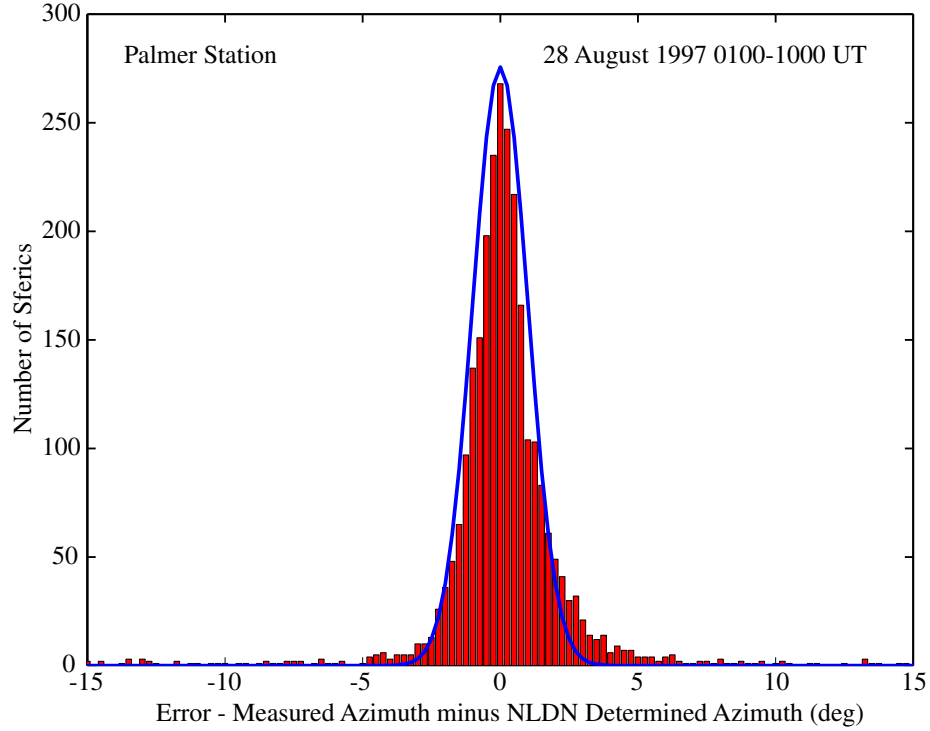


Figure 3.9: Histogram of the errors between arrival azimuths calculated from NLDN data and azimuths obtained from direction finding at Palmer Station.

sferics while the lowest detection efficiencies occur in the -5° to -15° range. This result is reasonable when one considers that the propagation path along the -39° bearing is primary over water while the propagation path along the -10° bearing crosses the South American continent. Hence the -10° path has higher attenuation than the -39° path due to the lower conductivity of land verses seawater [Wait, 1957]. Therefore, all else being equal, more sferics arriving along the -10° bearing fall below the detection threshold by the time they reach Palmer Station. A similar argument can be made to explain the difference in detection efficiency between the -39° and -29° bearings. Figure 3.8 shows that the lightning flashes along the -29° bearing are at a greater distance from Palmer Station than those along the -39° bearing. Once again, more of the sferics arriving at -29° have attenuated below the detection threshold than those arriving at -39° . The bottom panel of Figure 3.10 shows the

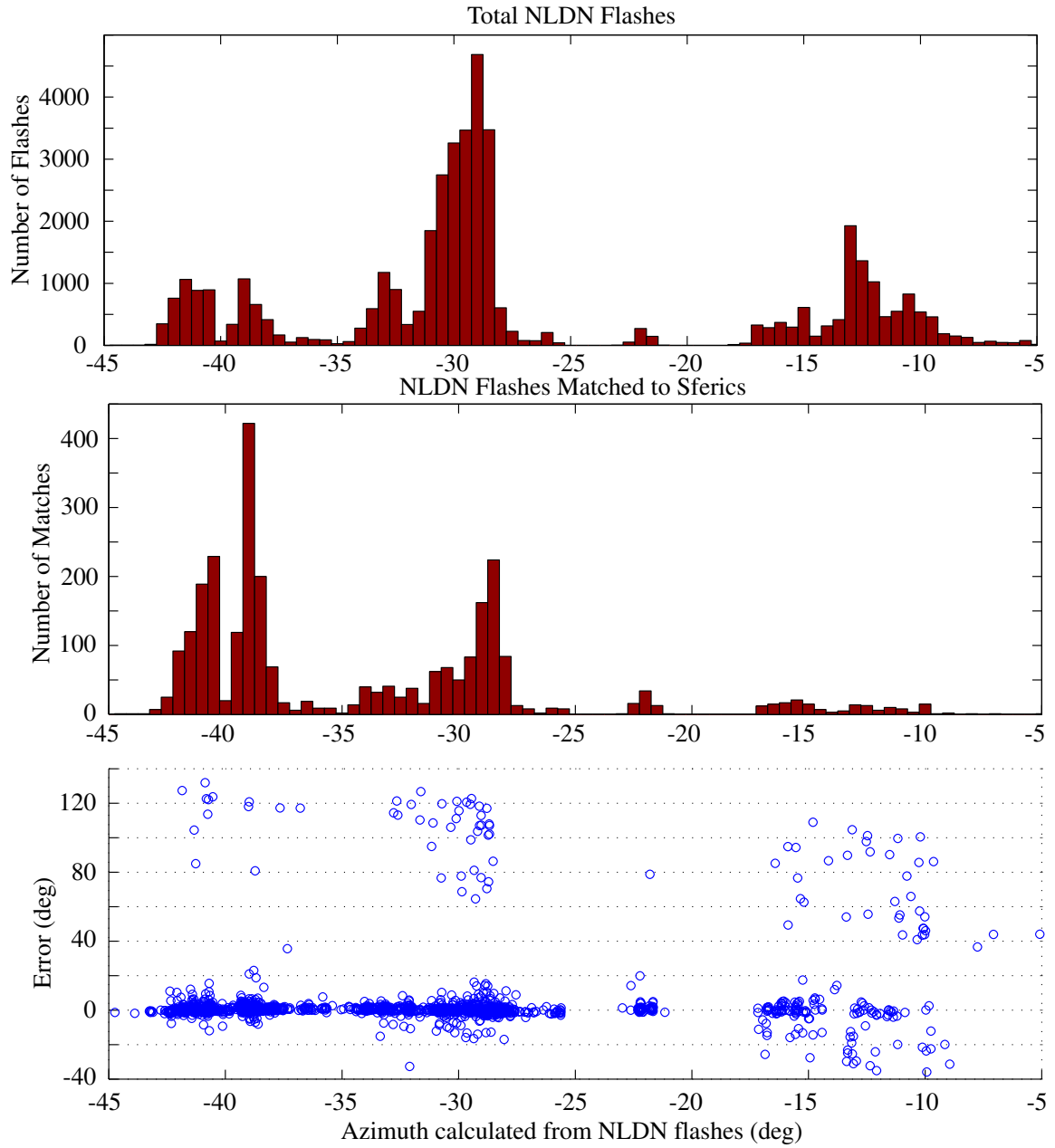


Figure 3.10: Comparison between arrival azimuth, detection efficiency and azimuth error.

azimuth errors for individual sferics versus their predicted arrival azimuths. Note that sferics with very large azimuthal errors appear to be clustered together with other sferics that have similarly large errors in azimuth. For example, a large number of sferics have azimuthal errors between 100° and 120° , suggesting that these sferics were mismatched to NLDN flashes and that they actually originate from a storm along a different azimuth such as in Africa. When these larger errors are left out of the error statistics, the accuracy improves such that 63.0% of sferics azimuths are accurate to within 1° and 83.6% of sferics azimuths are accurate to within 2° . Direction finding analysis from Palmer Station has been used in a number of applications including the identification of causative lightning waveforms that lead to the production of sprites [Reising *et al.*, 1999] and in the location of gamma ray producing lightning discharges [Inan *et al.*, 1996].

Unfortunately, not all receiver sites can be as electromagnetically quiet as that at Palmer Station. For example, the receiver located on Vieques Island in Puerto Rico (18.12° N, 65.50° W), the data from which are also used in this dissertation, is situated in a much more severe noise environment. For the Vieques Island site, the minimum required field strength amplitude for which the azimuth of a sferic can be correctly determined is ~ 25 mV/m, about 100 times greater than that at Palmer Station. This value corresponds to the detection of a ~ 10 kA lightning discharge at a range of $\sim 3,500$ km. The higher threshold of detection limits the Vieques Island site largely to the detection of sferics from only North and South America, although some of the largest sferics from Africa can also be detected. The Vieques Island site is further hampered by being a temporary installation instead of a permanent one such as that at Palmer Station, as a result of which the imperfections of the antenna setup are more pronounced ($\rho = -7.0^\circ$, $\xi = -4.0^\circ$, $\alpha = 0.75$) and therefore more difficult to correctly measure and account for. Figure 3.11 shows a histogram of azimuth errors for sferics matched to NLDN flashes from 0005 – 0950 UT and 1635 – 2350 UT on 8 September 2001. During this time, 8363 sferics detected at Vieques Island were matched to NLDN lightning flashes. The overlying curve is once again a Gaussian with a mean of 0 and a standard deviation of 1. This time, however, the correlation between the curve and the histogram is not nearly as good as it was for the Palmer

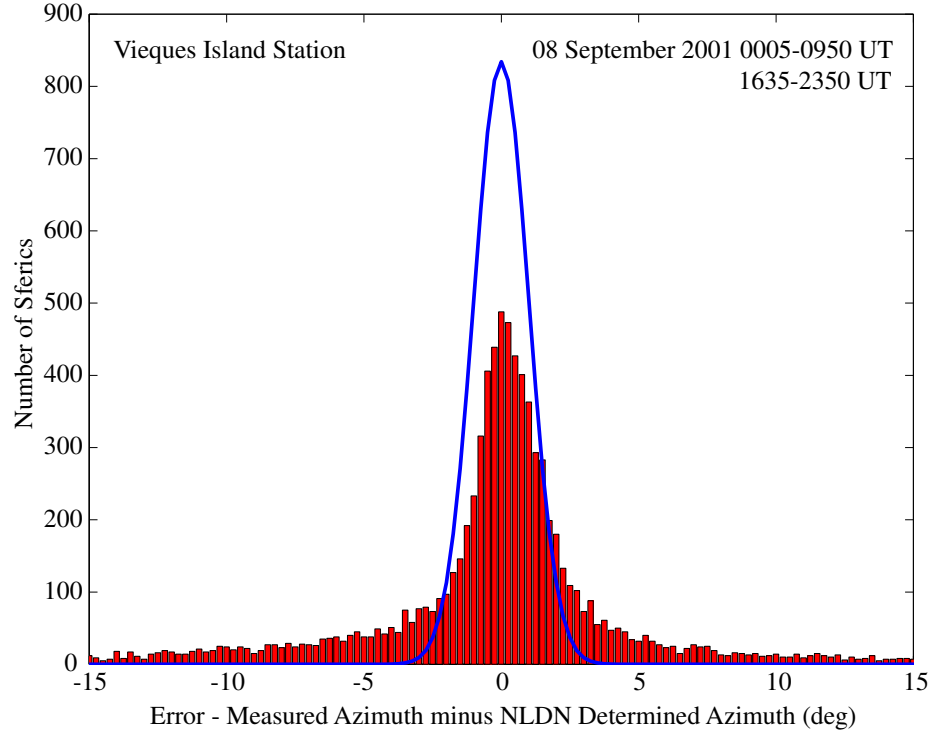


Figure 3.11: Histogram of the errors between arrival azimuths calculated from NLDN data and azimuths obtained from direction finding at Vieques Island.

Station error distribution (Figure 3.9). Instead, the Vieques Island error histogram has “side lobes” of larger errors that do not fit the Gaussian curve. Since the Vieques Island site is much closer to North America than Palmer Station, these errors are due most likely to polarization errors which are enhanced due to the fact that some very active lightning source regions are only a few hundred kilometers away.

The direction finding algorithm can also be evaluated through comparison with LIS data. One difference between the use of NLDN versus LIS data is that the latter detects and records cloud-to-ground lightning as well as intra-cloud lightning. The same process can be used to match sferics to LIS group level data as that used to match sferics to NLDN data. However, a cross-sensor evaluation of the LIS data [Ushio *et al.*, 2002] indicates that it is much more difficult to match the timing of LIS groups to event times from other data sets. Actually, measurements

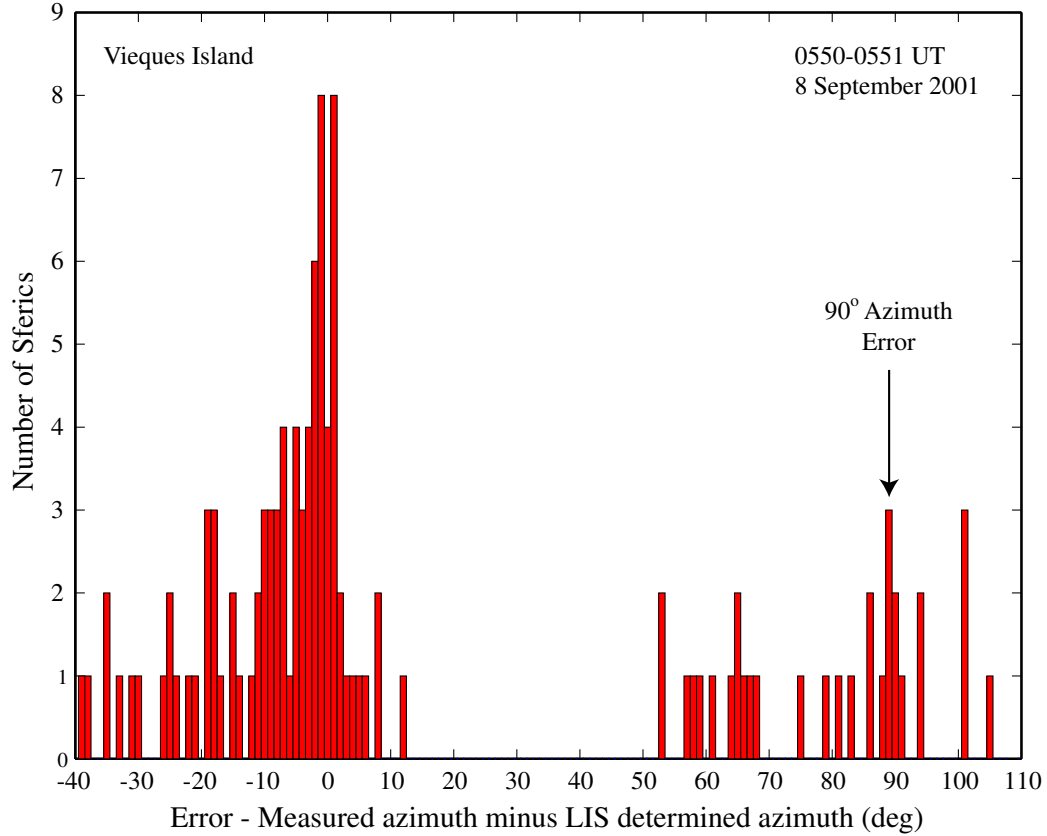


Figure 3.12: Azimuth errors between sferics detected at Vieques Island and LIS total lightning data.

show that the time offset can range from a few milliseconds to more than a second [Ushio *et al.*, 2002]. Thus, when matching to LIS data the timing requirement is expanded such that any sferics that are within 3 ms of a LIS group time are considered to constitute a match to that time. Figure 3.12 shows a histogram of azimuth errors for sferics matched to LIS groups from 0550 – 0551 UT on 8 September 2001. Notice that the largest peak in error occurs around 0° but that there is also another cluster with an error around 90° . If a sferic is composed primarily of QTE mode waves the application of our arrival azimuth determination algorithm would result in a 90° error due to our presumption of QTM modes. From Chapter 2, we know that horizontal IC discharges primarily excite QTE mode waves. Therefore, since LIS records both CG

and IC lightning discharges, it is likely that the sferics with a 90° error in azimuth relative to the azimuths calculated from LIS data do in fact originate in horizontal IC discharges within the same storm that propagate to the receiver in the QTE mode.

3.7 Correlation of Sferic VLF Energy and Lightning Peak Current

In addition to determining the arrival azimuth, the peak current of the causative lightning discharge can also be estimated from the peak amplitude of the VLF waveform of a sferic. The field intensity of a sferic is directly related to the current of the lightning discharge as can be seen from Equations (2.8) and (2.9). All sferics during 0100 – 1000 UT on 28 August 1997 detected at Palmer Station that matched to NLDN flashes and that had an azimuth error of less than $\pm 2^\circ$ degrees were correlated with the peak currents for those lightning flashes. For the entire period the VLF peak amplitudes and peak currents have a linear correlation coefficient of 0.77. However, due to $r^{-1/2}$ spreading discussed in Section 2.3.3 and attenuation caused by the finite conductivity of the waveguide boundaries, the constant of proportionality should depend on the distance from the lightning source to the receiver and on the characteristics of the path. Figure 3.8 shows that the lightning occurring in North America during this period is spread out both in distance from Palmer Station and laterally across great circle bearings. If the lightning activity is divided into zones based on its arrival azimuth such as in Figure 3.13, then the linear correlation coefficient improves dramatically. Figure 3.14 shows the linear correlation coefficient for each of the zones labeled 1 – 5. The highest correlation occurs in Zone 1 with a linear correlation coefficient of 0.95. This result is not surprising since the lightning in this zone is closely packed in its distance from the receiver and travels over a relatively low-loss sea path. The lowest correlation occurs in Zone 3 with a linear correlation coefficient of 0.90 (which is still much higher than 0.77). This result is also not that surprising since the lightning in this zone is spread out over the largest distance from the Gulf of Mexico up in to Canada. The linear correlation coefficients for the other

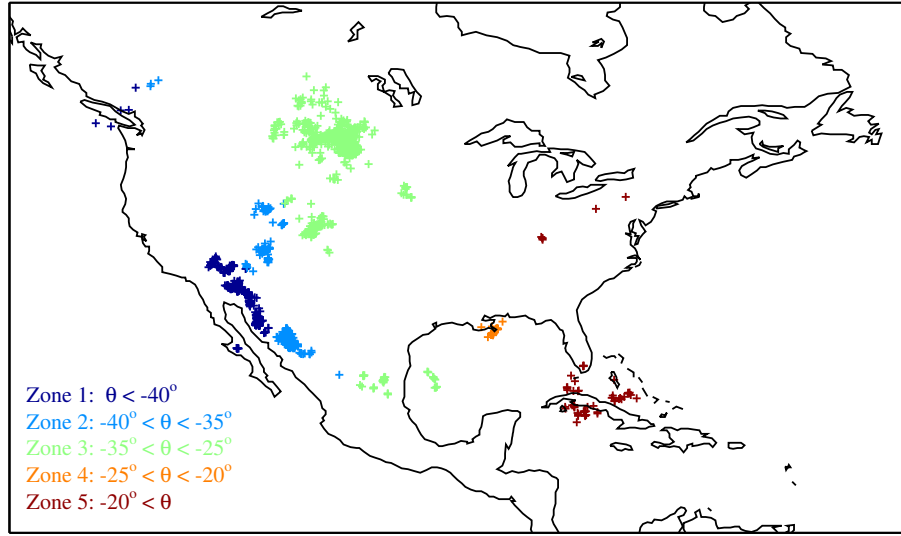


Figure 3.13: Divisions in arrival azimuth for sferics matched to NLDN flashes.

zones are also high, being ~ 0.94 , as the lightning in the other zones are also clustered in the same distance range.

3.8 Monitoring of Thunderstorms

With the arrival azimuth accuracy and VLF intensity/peak current relationship for individual lightning strokes established, some characteristics of thunderstorms can be recorded and examined continuously using VLF sferic data. Figure 3.15 shows histograms of projected azimuths at Palmer Station for NLDN flashes from three consecutive 3-hour periods. Notice that the number of flashes detected with a projected azimuth of -30° increases threefold from the first period to the third period. Also, the number of flashes with projected azimuths near -12° is greatly reduced from the first period to the last period. Figure 3.16 shows histograms of the arrival azimuths for sferics detected at Palmer Station for the same 3-hour periods. Note that the number of sferics detected with an azimuth near -30° during the third period is nearly twice the number detected during the first period. Also, a significant number of sferics were detected with an azimuth near -12° during the first period

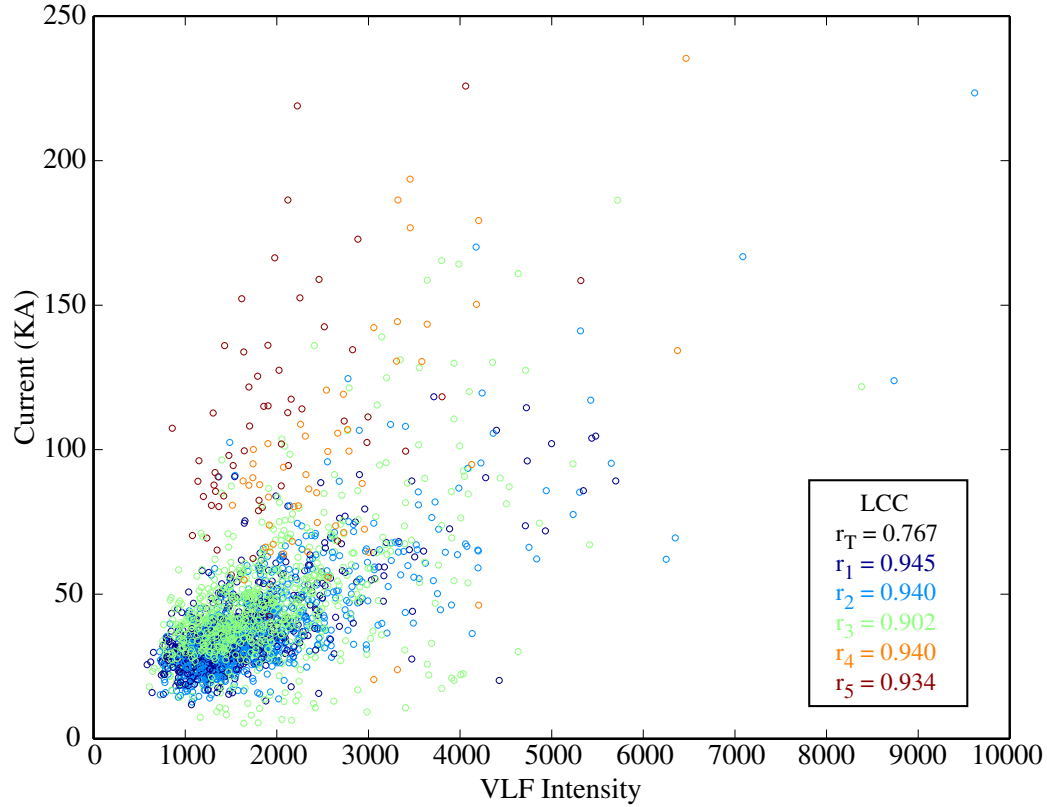


Figure 3.14: Linear correlation coefficients of VLF intensity verses NLDN peak current for sferics matched to NLDN flashes.

while very few were present during the third period. While the variations of the peaks from one 3-hour period to the next do not correspond precisely between Figure 3.15 and Figure 3.16, the overall behavior is quite similar. Also of interest in Figure 3.16 are the regions in azimuth where very few, if any, sferics are detected. Since it is already established that the sferics detected at Palmer Station originate in areas where there is lightning activity present, a lack of sferics detected along particular azimuth regions must indicate areas where there is little or no lightning activity present.

In some cases, two or more storms may be active simultaneously and located along the same azimuth bearing to Palmer Stations. In these cases it is not possible to monitor a storm using a single receiver. This limitation can be overcome by triangulating lightning locations using multiple receivers as discussed in Chapter 4.

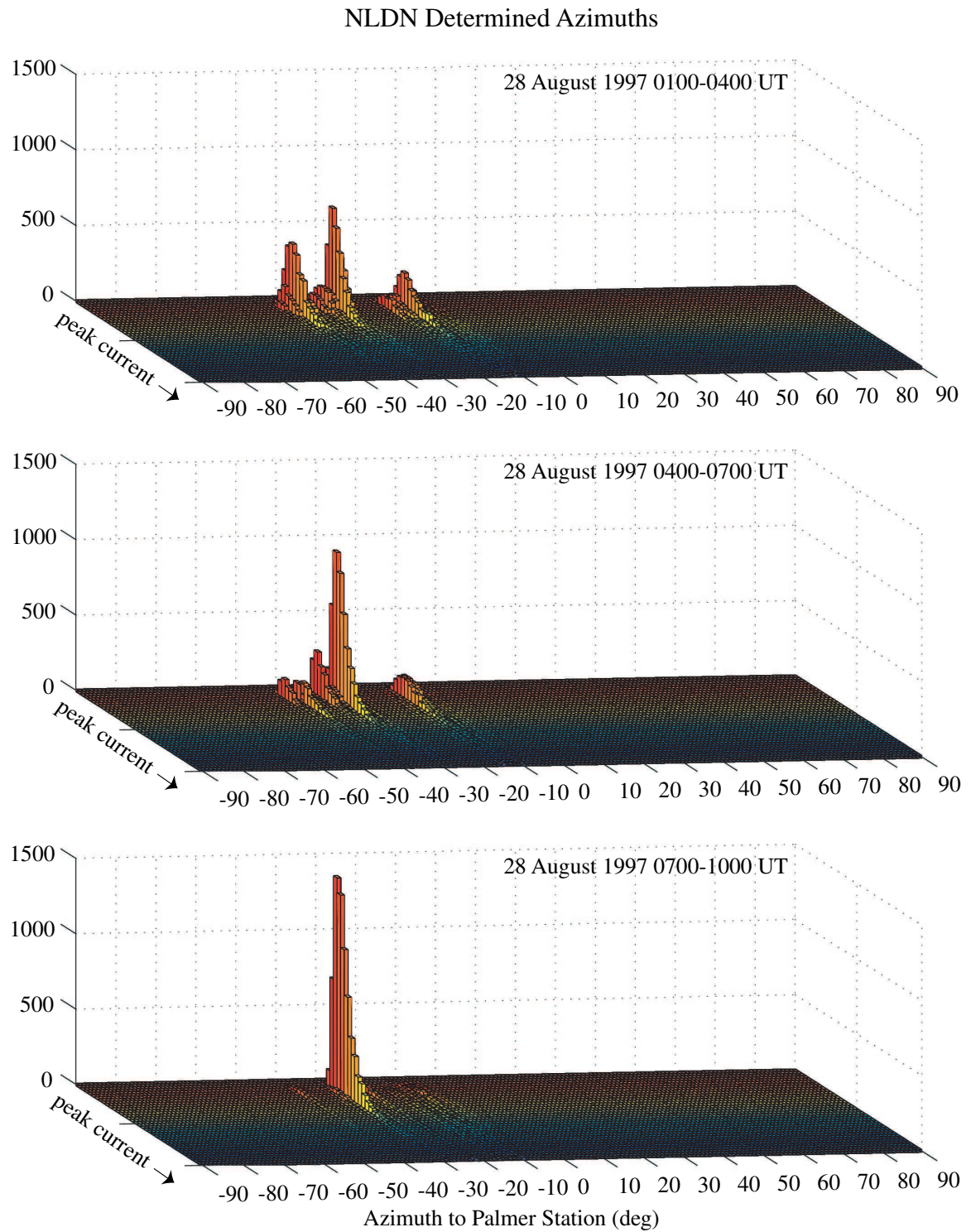


Figure 3.15: Histograms of arrival azimuths calculated from NLDN data.

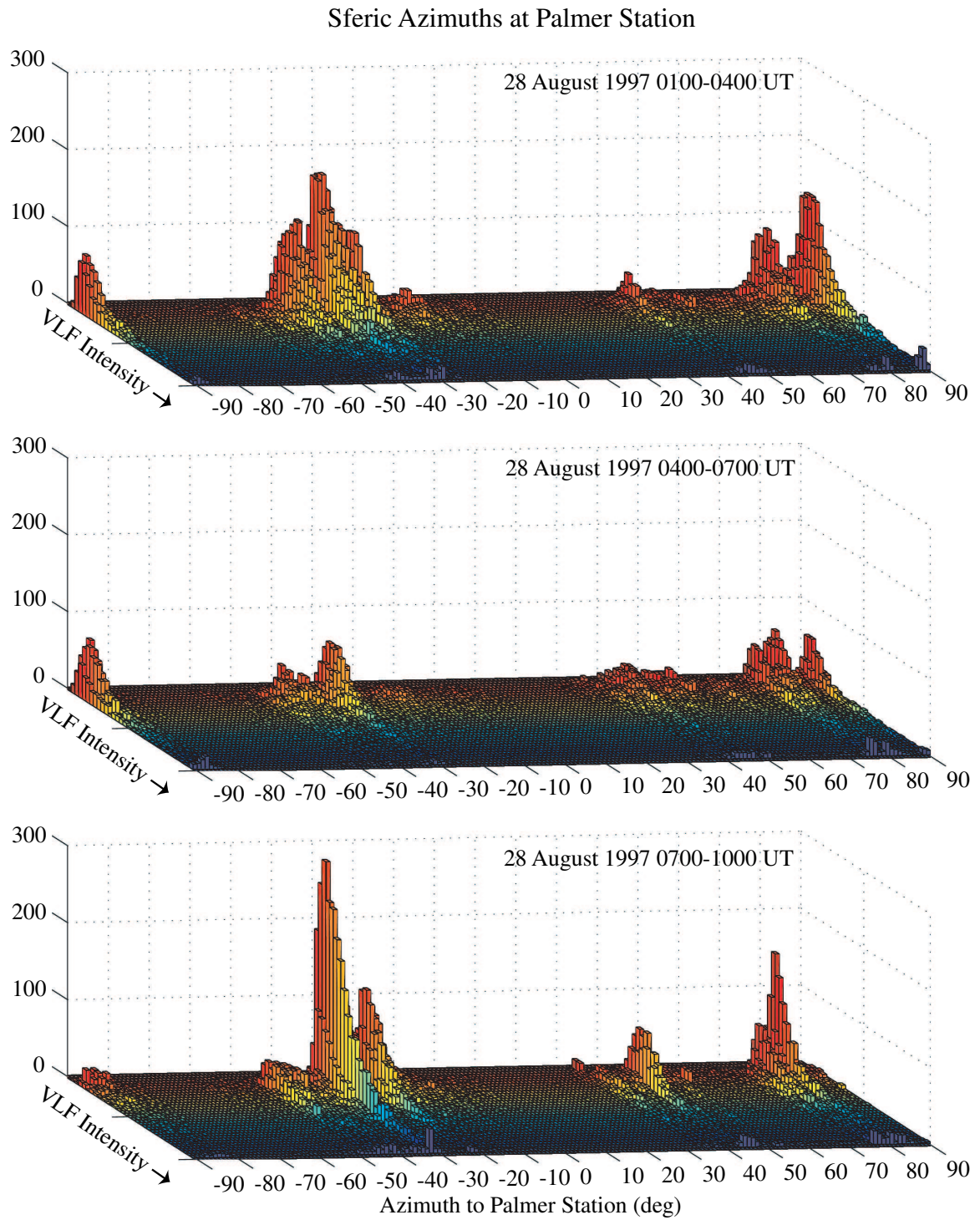


Figure 3.16: Histograms of sferic arrival azimuths.

Also of note in Figure 3.16 are the additional peaks that do not match to peaks in Figure 3.15. Since the receiver at Palmer Station can detect sferics arriving from all directions, these additional regions of high sferic occurrence indicate the presence of storms in other parts of the world outside of North America.

The top panel of Figure 3.17 shows the locations of optical transients detected by the Optical Transient Detector (OTD) from 0100 – 1000 UT along with several great circle paths to Palmer Station. The OTD coverage is limited in that it can see most points on Earth for a cumulative total of only about 14 hours over the course of a year [Christian *et al.*, 1999a]. This viewing time translates to only a few minutes of observation each day. The middle panel of Figure 3.17 shows a histogram of azimuths projected from OTD flash locations. The projected azimuths that cross the Antarctic continent were not counted because propagation over ice causes high attenuation [Rogers and Peden, 1975] and, in practice, it is unlikely that sferics propagating over Antarctica would be detectable at Palmer Station. The bottom panel of Figure 3.17 shows the arrival azimuths of sferics detected at Palmer Station from 0100 – 1000 UT. Both the middle and bottom panels show activity in the 90° to 95° range (recorded at Palmer Station as -90° to -85° due to the 180° ambiguity). This correlation strongly suggests that the sferics detected with azimuths in this range originated from the storm located off the coast of South Africa. At the same time, note that the other peaks in the bottom panel do not match up as well to storms seen in the OTD data. However, it should be noted that the receiver at Palmer Station is capable of detecting sferics from all directions simultaneously. Therefore, the other peaks visible in the third panel (i.e., peaks along azimuths of 50° , 80° and 85°) may identify storms, such as those in Central Africa, that became active while out of the field of view of the OTD. The same type of analysis described above was used during the investigation of the Space Shuttle Columbia accident, to provide evidence that the Shuttle was not struck by an electrical discharge during reentry.

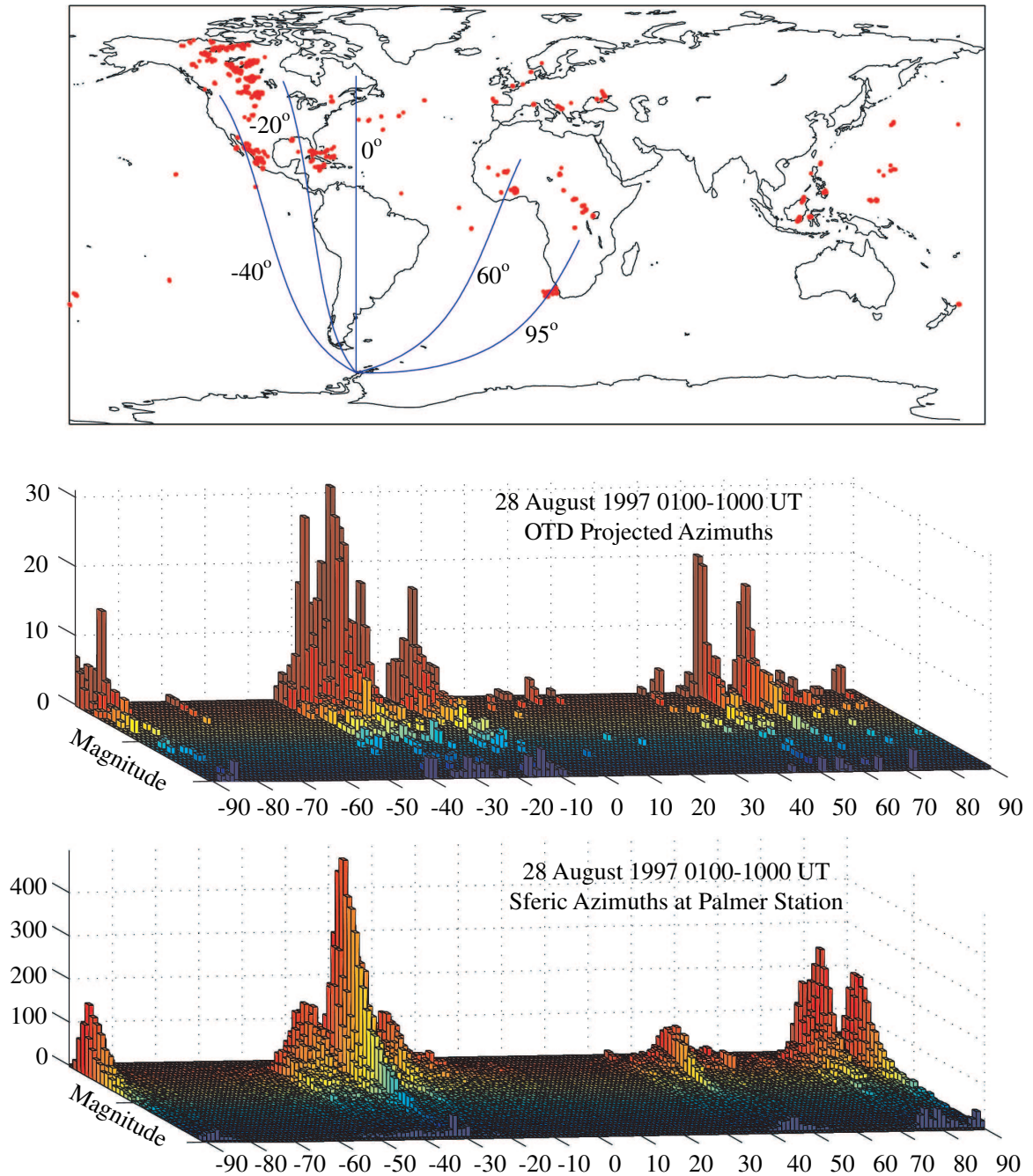


Figure 3.17: OTD data with azimuth lines to Palmer Station (top) and a comparison of projected OTD azimuths to sferic azimuth data (center and bottom).

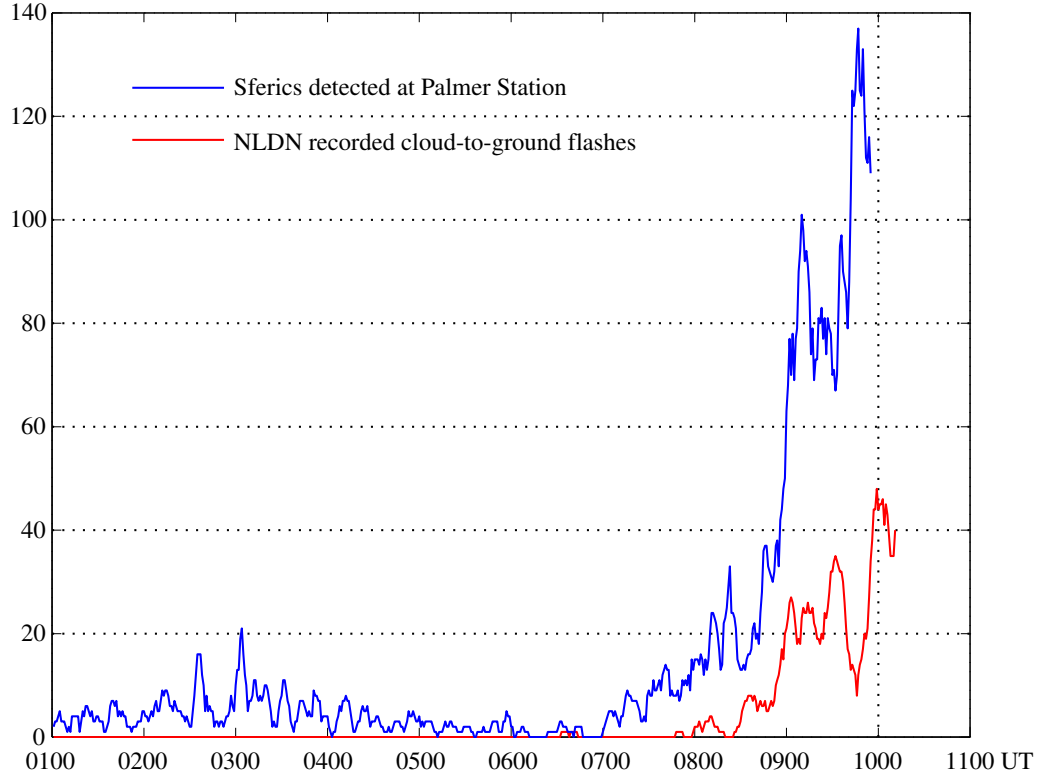


Figure 3.18: A rate comparison between sferics detected at Palmer Station with an azimuth between -21° and -23° and NLDN CG flashes with calculated azimuths between -21° and -23° .

3.9 Measurement of Lightning Stroke Rate

When there is only a single storm along a given azimuth, the sferic rate originating from that storm can be monitored through the detection of sferics over an extended period of time. Figure 3.8 shows a small, localized storm located off the coast of Louisiana and centered along a great circle bearing of -22° from Palmer Station. This storm is interesting in that no other North American storm is located along this azimuth during the 0100 – 1000 UT time period. The blue curve in Figure 3.18 represents the number of sferics detected at Palmer Station with an arrival azimuth between -21° and -23° . The bottom panel of Figure 3.10 shows that many of these sferics were correctly matched to NLDN detected flashes. The individual points on

the blue curve in Figure 3.18 are the sum of all the sferics detected over the previous 5 minutes. The red curve represents the projected azimuths of NLDN detected cloud-to-ground flashes occurring along the same azimuth range, -21° to -23° , not just those matched to sferics at Palmer Station. These two curves are correlated with a linear correlation coefficient of 0.88 suggesting that the sferic detection rate at Palmer Station is proportional to the NLDN cloud-to-ground flash rate for this storm. Also, the number of sferics detected at Palmer Station is approximately 3 times the number of cloud-to-ground flashes recorded by NLDN. This difference could, in principle, be due to sferics produced by the subsequent return strokes of the NLDN detected lightning flashes. However, the geometric mean interval between return strokes is ~ 58 ms [Thomson, 1980] whereas the geometric mean inter-arrival period between the sferics detected in this example is about ~ 80 ms for sferics arriving within 300 ms of each other. Also, many of the additional sferics, those not matched to NLDN flashes, have magnitudes that are just as large, if not larger, than the magnitudes of sferics matched to NLDN flash times (first return strokes). Since the first return stroke typically has a peak current that is twice that of subsequent strokes [Uman, 1987, p. 122-123], the additional sferics would not have such large magnitudes if they were generated by subsequent return strokes.

Another possibility is that the additional sferics observed at Palmer Station may be due to intra-cloud flashes produced by the same storm, which are not detected (by design) by the NLDN. In this connection, it is intriguing to note the apparent ~ 15 minute delay between the blue and red curves in Figure 3.18. In fact, if the sferic detection rate (blue) curve is delayed by 15 minutes, the linear correlation coefficient between the two curves increases to 0.94. One researcher observed a delay of 5 – 10 minutes between the first intra-cloud discharge and the first cloud-to-ground flashes in some storms [Krehbiel, 1986]. Furthermore, a formula developed by Prentice and Mackerras [1977] provides an empirical relationship for the expected ratio, Z , of the number of cloud flashes to the number of ground flashes in a storm as a function of latitude, λ .

$$Z(\lambda) = 4.16 + 2.16 \cos 3\lambda \quad (3.9)$$

For the storm of interest located at approximately $\lambda = 29^\circ$, north latitude, the expected ratio is $Z = 4.2$. Considering that the strengths of sferics arriving at Palmer Station must be above a specified threshold to be detected, this value is consistent with the 3 to 1 ratio between sferics detected at Palmer Station and NLDN detected cloud-to-ground flashes. Thus, it is possible that many of the sferics detected at Palmer Station were generated by intra-cloud discharges and that periods of increased intra-cloud activity are followed by a delayed but proportional increase in cloud-to-ground activity in this particular storm.

Further analysis of the sferics arriving in the -21° to -23° ranges reveals another interesting result. The ratio of the VLF peak intensity (the signal intensity of the frequency band from 5.5 to 9.5 kHz) to the ELF peak intensity (the signal intensity below 1.5 kHz) is 12% higher for the sferics matched to NLDN flashes than the ratio found in the other sferics detected along this azimuth range. The cutoff frequency of the first mode of the Earth-ionosphere waveguide occurs at ~ 1.7 kHz [Porrat *et al.*, 2001]. Therefore, propagation of the energy below 1.5 kHz in the sferic signals must occur as a QTEM mode wave since all the other modes will be evanescent at these frequencies. Other analysis shows that the QTEM mode only contributes to sferic signal at frequencies below ~ 1.2 kHz [Cummer, 1997].

Equation (2.10) shows that, except for the TEM mode, the excitation of TM mode waves changes as the height z of the vertical discharge increases in an ideal waveguide. The same holds true for the Earth-ionosphere waveguide. Figure 3.19 shows the ratio of the height gain functions of the first two waveguide modes to the height gain function for the TEM mode at a frequency of 7.5 kHz. These modes were determined by the Long Wave Propagation Capability (LWPC) program developed by the Naval Ocean Systems Center [Ferguson *et al.*, 1989] which simulates wave propagation in a realistic waveguide. As in an ideal waveguide, the height gain for the TEM mode in the Earth-ionosphere waveguide remains relatively constant as the altitude of the discharge is increased. For the other modes however, the height gain decreases, at least initially, as the altitude of the discharge is increased. Therefore, as is visible in Figure 3.19, the ratio of the height gain of the higher order modes to the height gain of the TEM mode decreases as the height of the discharge increases. In this case

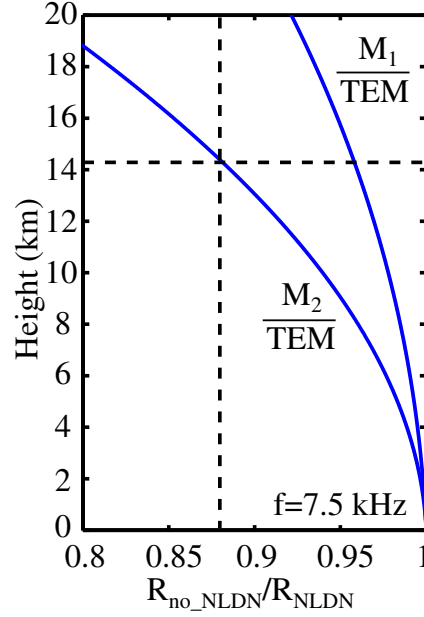


Figure 3.19: Ratio of height gain functions for two least attenuated modes, M_1 and M_2 , to TEM mode at 7.5 kHz. $R_{\text{no_NLDN}}$ is the ratio for sferics not matched to NLDN flashes and R_{NLDN} is the ratio for sferics matched to NLDN flashes

the ratio of the second mode to the TEM mode decreases faster than the ratio of the first mode to the TEM mode. However, LWPC also shows that the second mode is actually the least attenuated mode and should therefore be the dominant mode after propagating a great distance through the waveguide. Thus, a 12% difference in the ratio of VLF to ELF intensity would be indicative of a vertical discharge at a height of 14 km verses a vertical discharge at the ground. The opposite would be true for a horizontal discharge. Since TEM mode waves are not readily excited by horizontal discharges, the ratio of VLF to ELF intensity would be much higher for a sferic generated by a horizontal discharge than one generated by a vertical discharge. However, such is not what was observed. Thus, it appears that the additional sferics detected at Palmer Station were generated by intra-cloud lightning discharges with a substantial vertical component.

It is conceivable that there were other storms along the -22° azimuth out of range of the NLDN (e.g. in South America) that could account for the large number

of sferics detected at Palmer Station. However, OTD data does not contain any flashes along this path, or, for that matter, in South America during this time period. Furthermore, such a circumstance is unlikely in light of the high correlation between the sferic arrival rate and the NLDN flash rate for this storm. In particular, note that there were virtually no sferics detected prior to the onset of the lightning activity at around ~ 0700 UT, so that if there were other storms they would have to coincidentally become active at or near the same time as the North American storm.

Chapter 4

Lightning Triangulation

4.1 VLF Receiver Sites

In addition to the VLF receivers located at Palmer Station, Antarctica (64.77° S, 64.05° W) and Vieques Island, Puerto Rico (18.12° N, 65.50° W) Stanford University operates VLF receivers at several sites located around the world. Two others that are relevant to this dissertation are located at Upland, Indiana (40.45° N, 85.50° W) and Sde Boker, Israel (30.85° N, 34.78° E). The VLF equipment at these two sites is similar to the Palmer Station site in that they are permanent installations and utilize the larger triangular shaped antennas with a height of 10 m and a base of 20 m. All four sites are shown in Figure 4.1 and each site has the capability to record broadband VLF data from which sferics arrival times and azimuths can be extracted. By combining arrival times and azimuths from two or more sites, the locations of lightning sources can be determined via spherical triangulation.

4.2 Two Station Triangulation Algorithm

4.2.1 Location Grid

Figure 4.2 shows the great circle lines originating from Palmer Station, indicated by red lines, and from Vieques Island, indicated by blue lines. The great circle lines

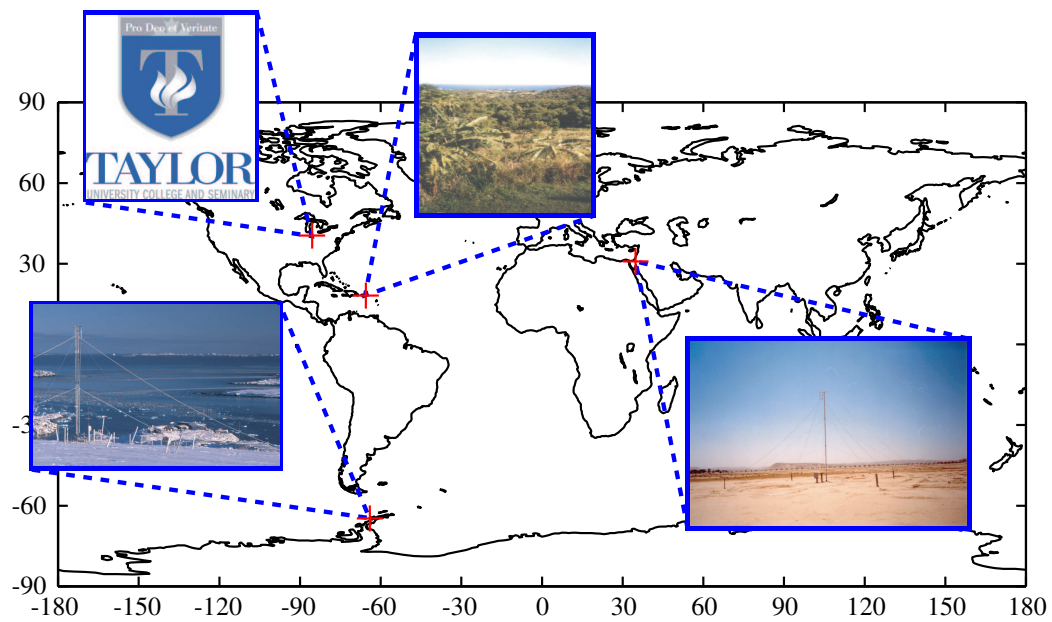


Figure 4.1: Important VLF receiver sites around the world.

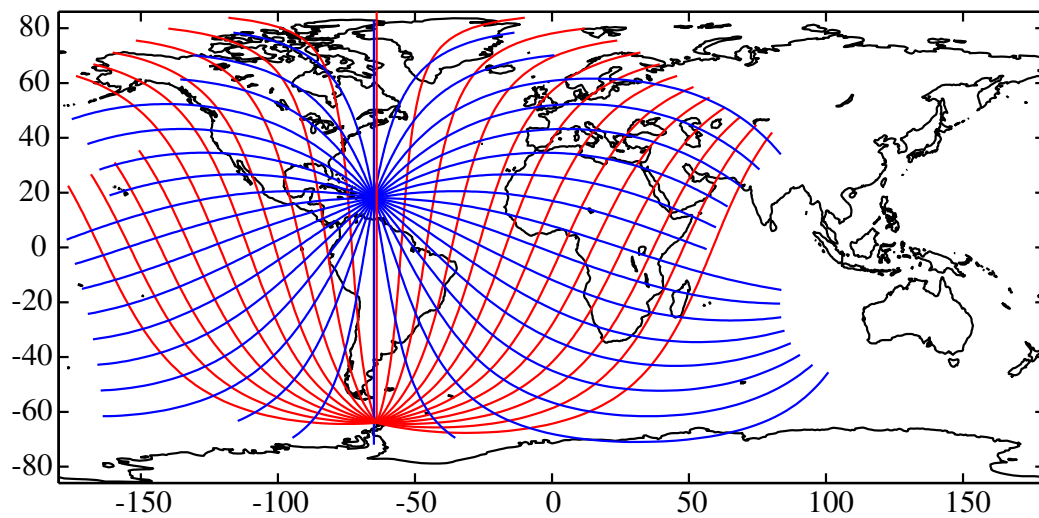


Figure 4.2: Lines of azimuth from Palmer Station (red) and Vieques Island (blue).

from the two sites form a grid that can be used to triangulate the location of a source lightning discharge. Given a site location and an arrival azimuth, a great circle path is defined about the Earth. These great circle paths are equivalent to the meridians of longitude if the receiver sites were located at the North or South poles. Also, any two distinct great circle paths intersect each other at exactly two points, which can be determined using spherical trigonometry [Orville, 1987]; a derivation of the equations for the intersection points are included in Appendix A.1. Therefore, arrival azimuths from Palmer Station and Vieques Island for sferics that originate at the same lightning discharge provide coordinates for two points on the Earth, which are antipodal to each other. The points of intersection determined by the arrival azimuths serve as a starting point for the determination of the source locations of lightning discharges.

In the absence of errors in arrival azimuth measurements, one of the two points of intersection between the great circle paths is the source location for the lightning discharge. However, in practice, errors are always present (as discussed in Chapter 3) in the azimuth measurements and translate into errors in the location estimate. This error is minimized when the great circle paths from the two sites cross one another at angles near 90° and is maximized when the great circle paths are close to being parallel to one another, which is the case for source locations along or near the great circle path connecting the two receiver sites. For such source locations, a small error in azimuth has a large effect on the points of intersection of the two great circle paths. In order to more accurately estimate the lightning source location in spite of such errors, the difference in the time-of-arrival (TOA) for the sferics at the two receivers is incorporated into the location algorithm.

Figure 4.3 shows lines of equal TOA difference between Palmer Station and Vieques Island. Assuming uniform propagation velocity (in reality this is not always true since the group velocity is different from daytime to nighttime and portions of one or both of the source-receiver paths may be daylit), sferics originating on the same line have equal TOA differences between Palmer Station and Vieques Island. For example, a sferic originating at any point on the red line in Figure 4.3 arrives at Palmer Station and Vieques Island at exactly the same time. When a line of

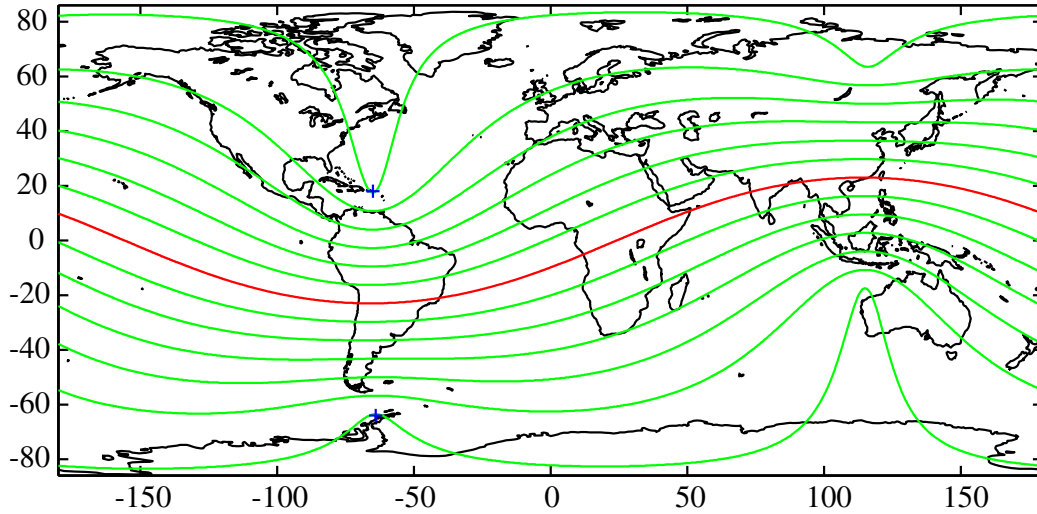


Figure 4.3: Lines of equal time of arrival difference between Palmer Station and Vieques Island.

equal TOA difference is combined with arrival azimuth lines from Palmer Station and Vieques Island, a set of quasi-spherical triangles are created. The triangles so formed are quasi-spherical since the lines of equal TOA difference are spherical hyperbolas rather than great circles. Figure 4.4 shows the geometry that might develop from measurements taken from a sferic originating in central Africa. The red line is the arrival azimuth at Palmer Station, the blue line is the arrival azimuth at Vieques Island, while the green line represents equal TOA difference. These lines form a small triangle at one location, in this case Africa, but also form another (larger) triangle on the other side of the Earth. The geometry in Figure 4.4 shows the triangle enclosing the actual lightning event although statistically (and in the presence of error) this does not always have to be the case.

4.2.2 Computational Solution

As an analytical solution, the center of gravity of this triangle was suggested by *Sato and Fukunishi* [2003]. However, *Sato and Fukunishi* incorrectly take the TOA difference curve to also be a great circle. Since an analytical solution becomes intractable

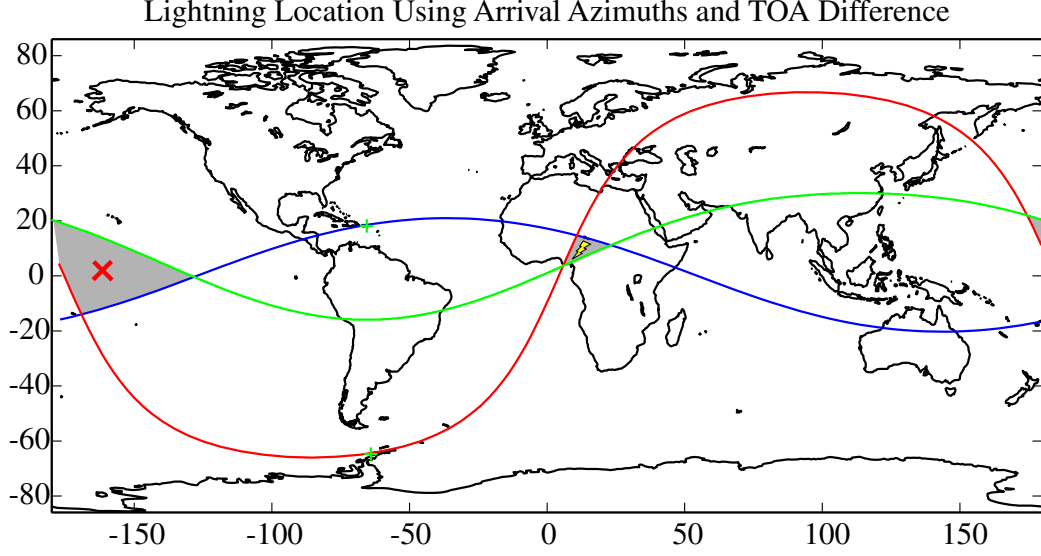


Figure 4.4: Two Station Triangulation Illustration

when the TOA difference curve is taken as a spherical hyperbola, a numerical method is used here instead. First, for every point (with 25 km resolution in latitude and longitude) on the Earth's surface the ideal values for the arrival azimuths at Palmer Station and Vieques Island from that point and the ideal TOA difference between the two stations are computed ($v_g = 0.988c$ at 13 kHz from Equation 2.6). In the actual computation of these values, the fact that the Earth is physically an oblate spheroid and not a true sphere is taken into account. These values are then put into a look-up table for future use. Thus, each 25 km by 25 km grid point has three values associated with it, namely the two arrival azimuths and the TOA difference between the two stations. When performing a triangulation, the two grid points that contain the points of intersection of the two arrival azimuths are used as starting points. Thus, the location estimation is performed at two different points on the earth. At each starting point, as identified in Figure 4.5, and its eight surrounding grid points, the residual error is computed using the chi-square function

$$\chi^2 = c_1(\theta_{\text{meas}_1} - \theta_{\text{ideal}_1})^2 + c_2(\theta_{\text{meas}_2} - \theta_{\text{ideal}_2})^2 + d_{1,2}(\Delta t_{\text{meas}_{1,2}} - \Delta t_{\text{ideal}_{1,2}})^2 \quad (4.1)$$

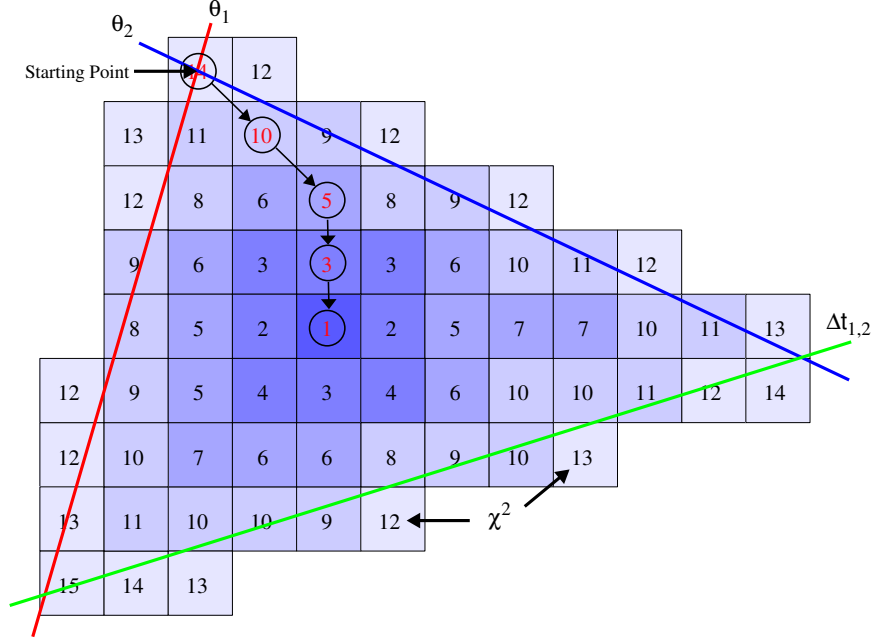


Figure 4.5: Two Station Lookup Table

where θ_{meas_1} is the measured arrival azimuth at Palmer Station, θ_{ideal_1} is the pre-calculated Palmer Station arrival azimuth, θ_{meas_2} is the measured arrival azimuth at Vieques Island, θ_{ideal_2} is the pre-calculated Vieques Island azimuth, $\Delta t_{\text{meas}_{1,2}}$ is the measured TOA difference in milliseconds and $\Delta t_{\text{ideal}_{1,2}}$ is the pre-calculated TOA difference in milliseconds. The values c_1 , c_2 and $d_{1,2}$ determine the weighting of each measurement. Any chi-square function can be used but the measurement with the least expected error should have the highest weighting [Hiscox *et al.*, 1984]. For our pair of receivers, c_1 and c_2 are given a weighting of 1 and $d_{1,2}$ is given a weighting of 4 because the standard deviation in azimuth error is one degree and the standard deviation in the timing error, when matched to NLDN times, is about half a millisecond. Thus, after the weighting, each component of the chi-square function will have the same standard deviation. It may at first be questioned as to whether it is appropriate to combine measurements of quantities with different units in this manner. However, each component in the chi-square function should be thought of in terms of its correspondence to the same position error at a range of 5,000 – 10,000 km.

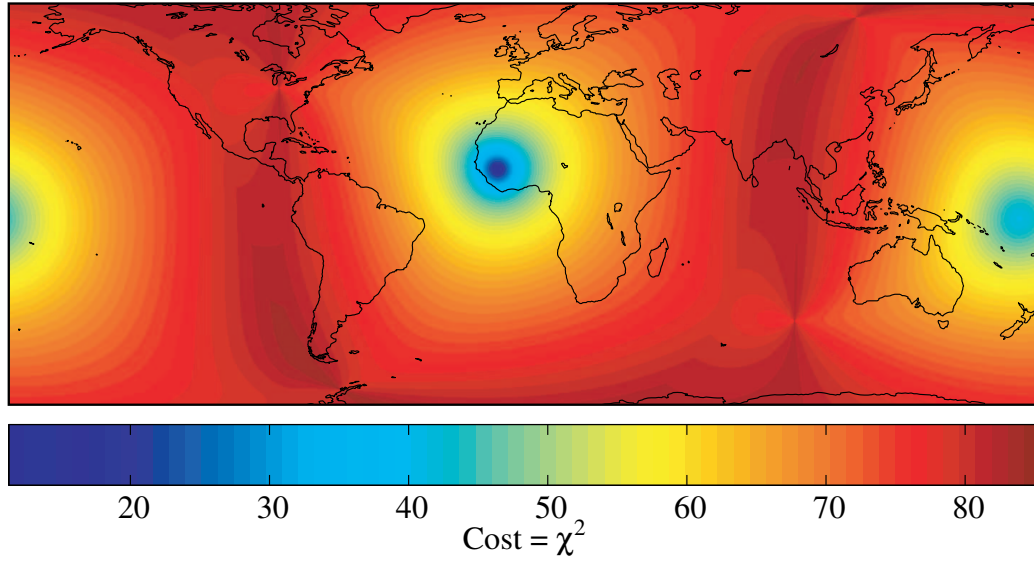


Figure 4.6: Two station chi-square cost map.

After computing the chi-square function at all nine grid points, we determine whether one of the eight points surrounding the intersection point has a smaller chi-square error than the intersection point, and if so use that point as the new starting point. Once again, the chi-square function at all of the surrounding points is computed and the process is continued until the minimum chi-square error point is reached. Figure 4.5 illustrates how the minimum chi-square error point is found by “sliding” down the chi-square error gradient. When using this technique to find a global minimum, one must be careful not to get caught in a local minimum. Figure 4.6 shows the chi-square error surface for the entire Earth for the azimuth and TOA difference measurements depicted in Figure 4.4. Notice that local minima exist near the receiver site locations and at the locations antipodal to the receiver site locations while the primary minima exist at the lightning source location and its antipodal point. Since the intersection of the azimuth lines is used as the starting point, in most cases this point is close enough to the global minimum and away from the wells of the local minima. Once again, the algorithm is performed at both intersection points of the azimuth lines. Thus two minima are found on opposite sides of the Earth. The first criterion for selecting one of the two points as the most likely lightning source

point is to make sure that the point falls within range of the receivers, deemed to be about 10,000 km. If both points are within range of both receivers then the point with the smallest chi-square error, corresponding to the point inside of the smallest triangle, is selected (this does not mean that the real source event is actually located inside the triangle, this is just the point that the source is estimated to be at).

Because the two receivers are widely separated, a space-time complication arises when attempting to match sferics received at one site with the corresponding sferics received at another site. Since the global flash rate is as high as 100 flashes every second [Orville and Spencer, 1979], it is sometimes ambiguous as to which sferics match to one another. This type of mismatch is in part due to the high sferic rate at Palmer Station, which can be upwards of 100 per second (obviously not all sferics from around the world are detectable at Palmer Station but most lightning flashes generate multiple sferics). As an example, a lightning discharge A occurring close to one receiver may be followed a few milliseconds later by a lightning discharge B occurring close to the other receiver. In such a circumstance, the sferic from discharge A arrives at the first receiver followed by the sferic from discharge B. However, at the second receiver, the sferic from discharge B arrives first, followed by the sferic from discharge A. To account for this possibility, triangulation is performed on all possible sferic matches. In other words, given a sferic arrival time at one site, triangulation is performed by pairing this sferic with all sferics arriving at the other site during a realizable time frame. For Palmer Station and Vieques Island, this time frame is plus or minus ~ 30 ms, which is the propagation time from one receiver to another over a distance of 9130 km. It is thus impossible for a sferic coming from a unique lightning source to have an arrival time difference greater than this between the two sites. After all of the triangulations are performed, the best-best source location is selected based on the triangulation which has the smallest chi-square error value. Also, a maximum chi-square error threshold is set for reporting an event location, as is discussed later in the simulation results Section (4.3.3).

4.3 Two Station Triangulation Simulation

Before application of the technique described in the previous section to actual data, it is useful to simulate the conditions under which the algorithm is to be used. Simulation provides information about three types of error that occur in the use of such an algorithm. These are designated as location error, antipodal error and mismatch error. These errors are shown for the two receiver systems at Palmer Station and Vieques Island.

4.3.1 Location Error

Location error is the most obvious type of error that occurs in the triangulation algorithm. Location error determines the fundamental accuracy that can be achieved in the presence of measurement errors in the arrival azimuth and time of arrival values. Figure 4.7 shows results for simulated discharges occurring at: a, (30° N latitude, 100° W longitude); b, (5° N, 0°); c, (10° S, 75° W); d, (25° S, 65° W); e, (35° N, 65° W). Locations “a” and “b” were chosen to show the performance of the two receiver system near the extreme of its range. Locations “c” and “d” were chosen to illustrate the optimal performance region for the system, while location “e” was chosen to exemplify the least optimal performance region. For the simulation, the expected arrival azimuths and arrival times at Palmer Station and Vieques Island are first calculated. A random error with a mean of 0° and standard deviation of 1° is then added to the azimuth calculations, in accordance with Figure 3.9. The same error distribution is assumed for the Vieques Island site since the system is designed to detect sferics arriving from an appropriately long range. The expected TOA difference is also calculated and a time error with a 0 ms mean and 1/2 ms standard deviation is added. The simulated sferic measurements are then given as inputs to the triangulation algorithm. The median error for the discharge at location “a” is ~ 110 km and the median error for the discharge at location “b” is ~ 105 km. The smallest errors occur for the locations in South America, “c” and “d”, which have median errors of ~ 75 km, while the largest error occurs at location “e” which has a median location error of ~ 2000 km. For all cases, the blue crosses identify

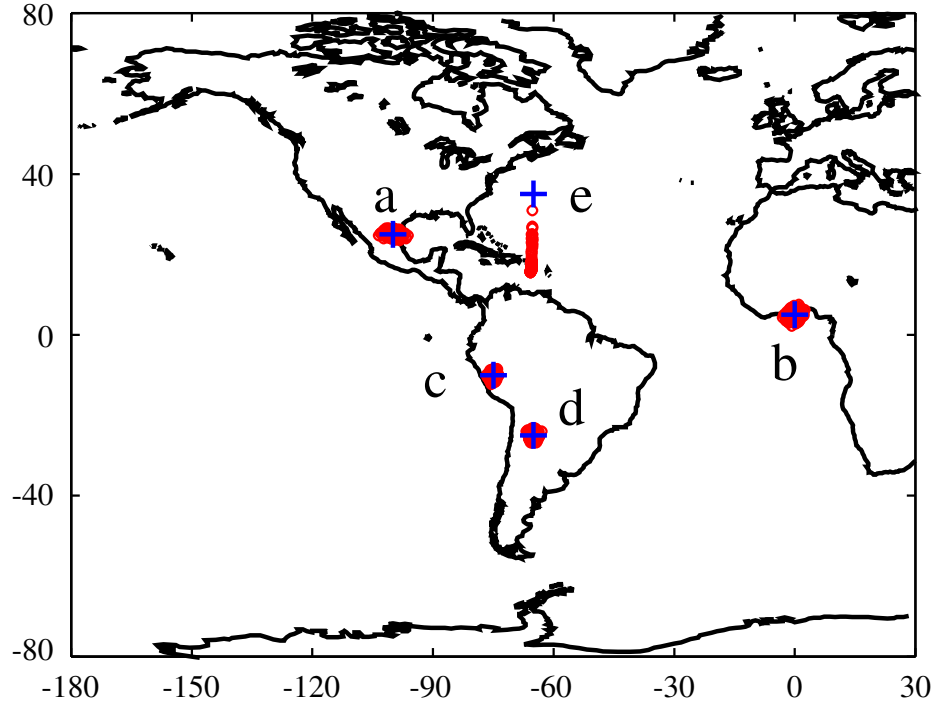


Figure 4.7: Simulated location error.

the location where the event occurred while the red area spans the region within which the simulated events were located. Simulation results also show that the more accurate the azimuth and time of arrival measurements, the lower are the location errors. For example, doubling the standard deviation of all of the measurements doubles the median location error and vice versa.

4.3.2 Antipodal Error

The second kind of error present in the simulations, shown in Figure 4.8, occurs when the algorithm mistakenly places the discharge source location at the antipodal point of its actual location. For a two receiver array, there are certain regions where the grid formed by the azimuth lines and TOA difference lines is symmetric and the azimuth lines and TOA difference line converge equally at antipodal points on the Earth. When error is added to the measurements, the minimum error point can switch from

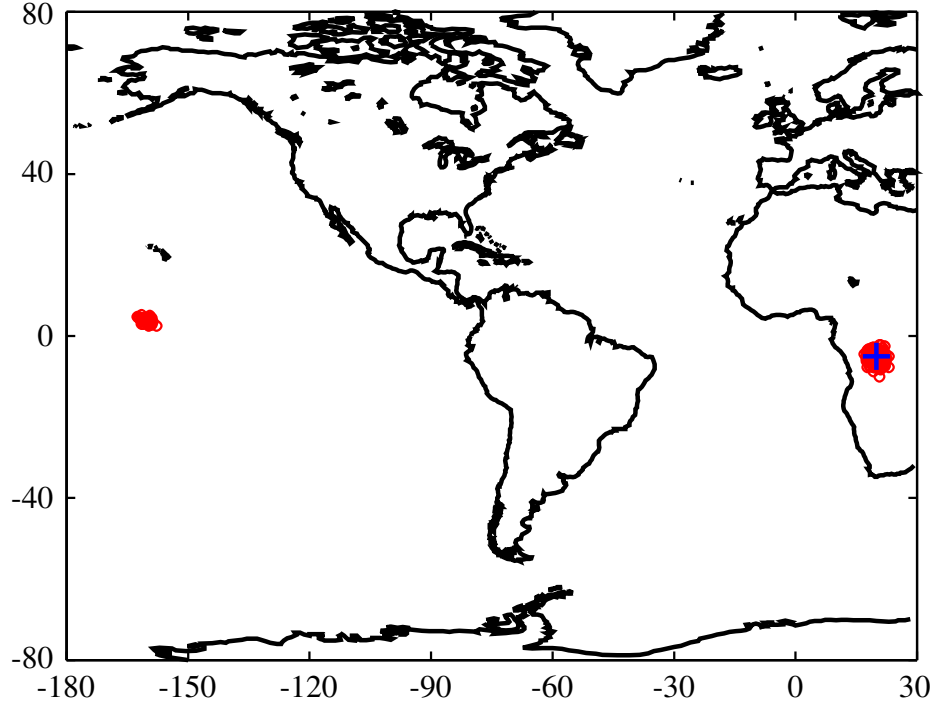


Figure 4.8: Simulated antipodal error.

the correct position to the antipodal position. One of these sensitive regions is located at the center of the array between the two receiver sites. Fortunately, this region does not pose a problem since, with the two sites both being in the western hemisphere and at about the same longitude, it is highly unlikely that a sferic generated by a lightning strike on the opposite side of the Earth (which in this case corresponds to the Indian subcontinent) would be detected by the receivers due to the very long distances and hence high attenuations involved. Therefore, the location between the receiver sites is always selected even if the antipodal point has a low chi-square error value.

The other region of concern, the one shown in Figure 4.8, is unfortunately located in central Africa, one of the most active lightning regions in the world [Bocippio *et al.*, 2002]. Figure 4.8 shows that many of the simulated lightning discharges (red areas) are incorrectly located near the antipodal point of central Africa, which is in the middle of the Pacific Ocean.

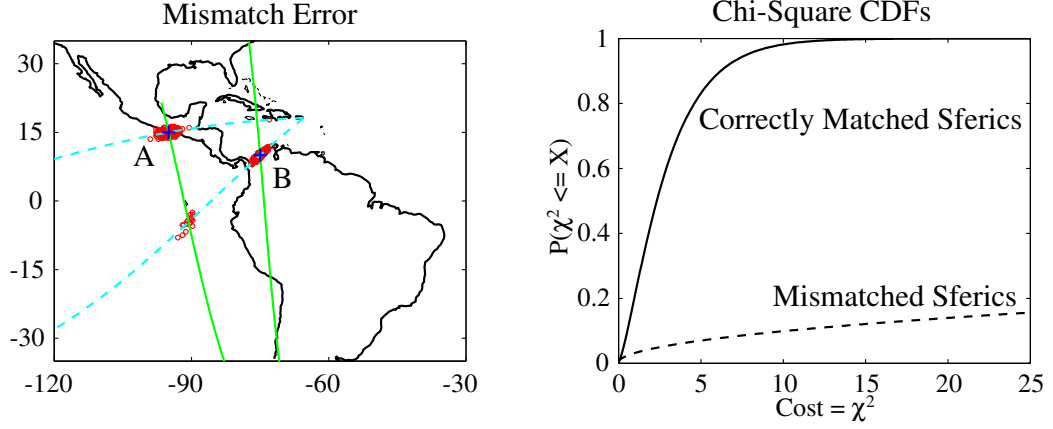


Figure 4.9: Simulated mismatch error.

4.3.3 Mismatch Error

The third kind of error revealed in the simulation is caused by the ambiguous matching of sferics detected at one receiver site to those detected at the other receiver site. This error is referred to as “mismatch” error. For this simulation, virtual storms were created at (15° N, 95° W) and (10° N, 75° W), designated as storm A and storm B respectively. Each storm was set to produce lightning discharges at random times with an inter-discharge interval specified by the exponential distribution

$$f_T(t) = \lambda_1 e^{-\lambda_1 t}, \quad t \geq 0 \quad (4.2)$$

with $\lambda_1 = 12.76s^{-1}$ [Chrissan, 1998, p. 51-68]. The results of this simulation are shown Figure 4.9 along with the arrival azimuth lines from Palmer Station (green) and Vieques Island (cyan). The majority of the lightning discharges are located correctly to within the expected positional error of ~ 100 km, determined by the measurement accuracy. However, a few discharges are incorrectly located at the crossing point of two “mismatched” azimuth lines. This type of mismatching occurs when a sferic from storm A detected at Palmer Station is matched to a sferic from storm B detected at Vieques Island. In order for the discharge to be incorrectly located at the crossing point of these azimuth lines, the chi-square value for the mismatched sferics must be

less than the chi-square value that exists when the Palmer Station sferic is correctly matched to its corresponding Vieques Island sferic. Such a condition occurs by chance even though the two discharges are unrelated events, in those cases when the TOA difference between mismatched sferics happens to be low.

The right side of Figure 4.9 shows the cumulative density functions (CDF) for the chi-square function for correctly matched sferics (solid line) and mismatched sferics (dashed line). It is evident that almost 100% of correctly matched sferics have a chi-square value of 13 or less, while only about 10% of mismatched sferics have a chi-square value of 13 or less. However, in some cases, the chi-square value for mismatched sferics can be lower than the chi-square value for correctly matched sferics. When this occurs, some lightning discharges are incorrectly located, as is revealed in Figure 4.9 by the red circles located out in the Pacific Ocean. These errors occur primarily due to the high sensitivity of the receivers used, which can detect sferics arriving from over 10,000 km away, so that the sferic rate seen by a single receiver is the sum total of the sferic rates for all the storms within 10,000 km of the site.

4.4 Two Station Triangulation Observations

Due to the synoptic (i.e. 1-min out of every 15-mins) style recording schedule and occasional system failures at the Vieques Island receiver site, the practical performance of the triangulation algorithm is best judged by comparison to the NLDN (the data for which are continuously available) rather than to LIS which views a given area for only a short duration each day. Figure 4.10 shows the detection efficiency relative to the NLDN detected cloud-to-ground flashes for 8 September 2001. Given at the top of each white bar is the total number of NLDN flashes that occurred during the periods for which Vieques Island and Palmer Station data are available. The top of each blue bar is the number of those NLDN flashes that were matched to triangulated events. A triangulated event is considered a match if it occurs within 2 ms of an NLDN flash time and within 750 km of the NLDN location. The highest detection efficiency is found during the 0900-1000 UT time period where 72% of NLDN flashes are detected. The lowest detection efficiency is found during the 2200 – 2300 UT time period where

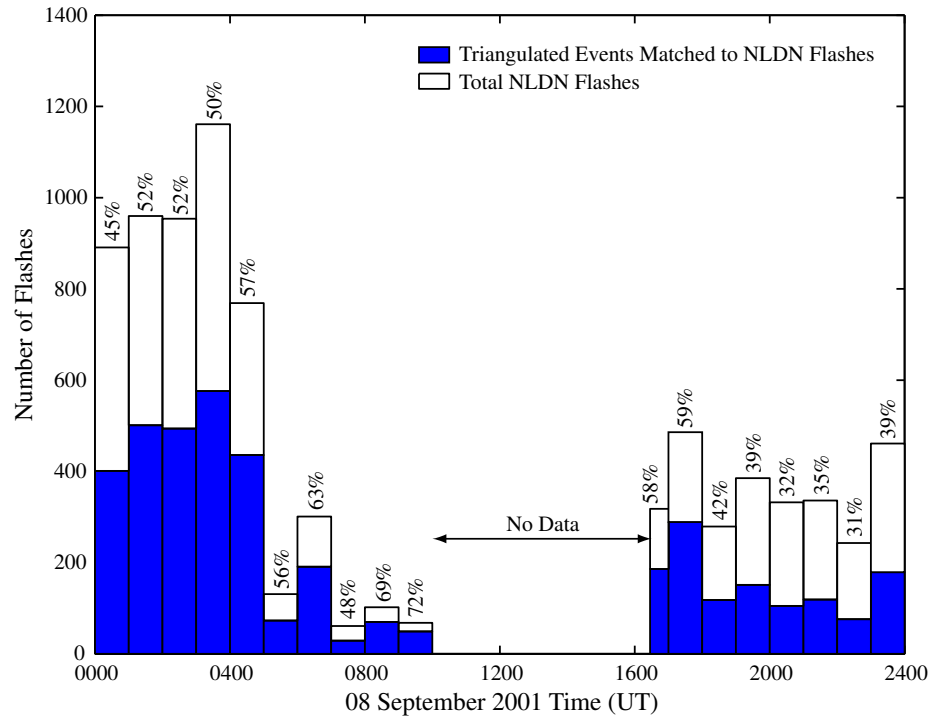


Figure 4.10: Detection efficiency of the triangulation algorithm.

only 31% of NLDN flashes are detected. This result is consistent with the fact that VLF signals are subject to lower attenuation at night than during the day and thus a higher percentage of sferics are detected at Palmer Station at night. Overall, for the entire day, 49% of NLDN flashes are detected. No data are available during the 1000 – 1630 UT time period, due to an intermittent recording schedule at Vieques Island.

Figure 4.11 shows the location accuracy of the the events triangulated on 8 September 2001 that are matched to NLDN flashes. The smallest location error is found during the 0000 – 0100 UT time period where the median location error is 174 km. The greatest location error is found during the 1900 – 2000 UT period where the median error is 298 km. Also, the 0000 – 1000 UT time period shows slightly better performance than the 1630 – 2400 UT time period. The 0000 – 1000 UT time period corresponds to nighttime propagation conditions from North America to the

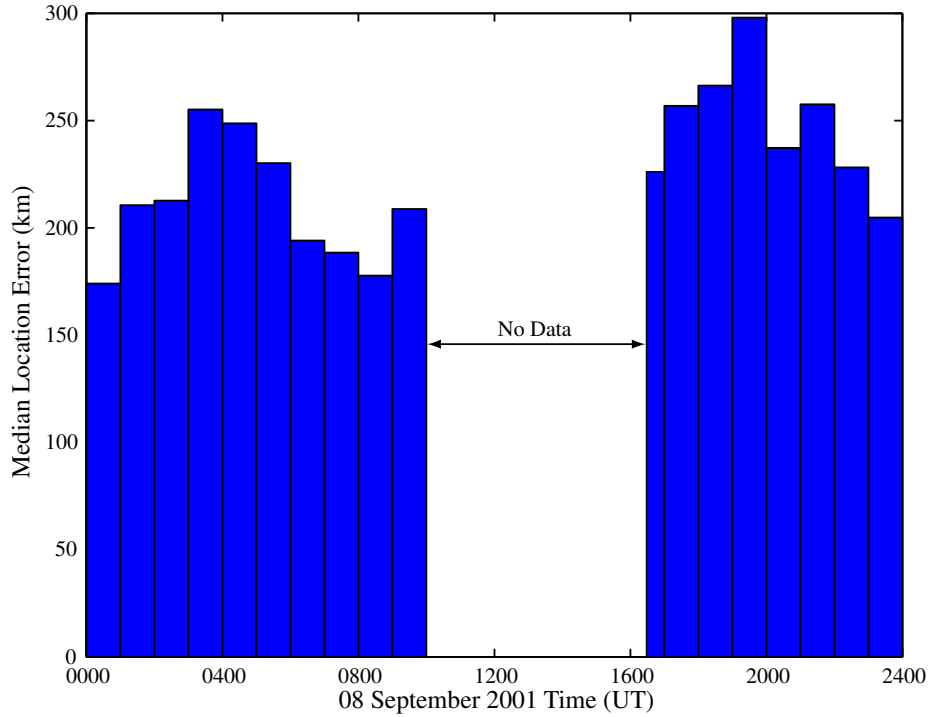


Figure 4.11: Location accuracy of the triangulation algorithm.

two receiver sites and the 1630 – 2400 UT time period corresponds to daytime propagation conditions. Thus, the difference in location error may be due to the variance in group velocity from nighttime to daytime. The difference in location error may also be due to the location of lightning discharges in North America, as discharges occurring in the eastern United States have worse location performance than discharges occurring in the western United States due to the relative locations of the receivers. Such a situation is evident in the simulation results in Section (4.3.1).

A general comparison of areas of lightning activity can be made with the Lightning Imaging Sensor. The upper panel of Figure 4.12 shows the sum of all lightning events located by LIS from 0000-2400 UT on 9 September 2001. Due to its low Earth orbit, the LIS instrument only passes over a particular area at certain times during the day. For example, on 9 September 2001, Florida is overflown at about 1140 UT and 1630 UT. The remaining panels of Figure 4.12 show lightning locations determined using

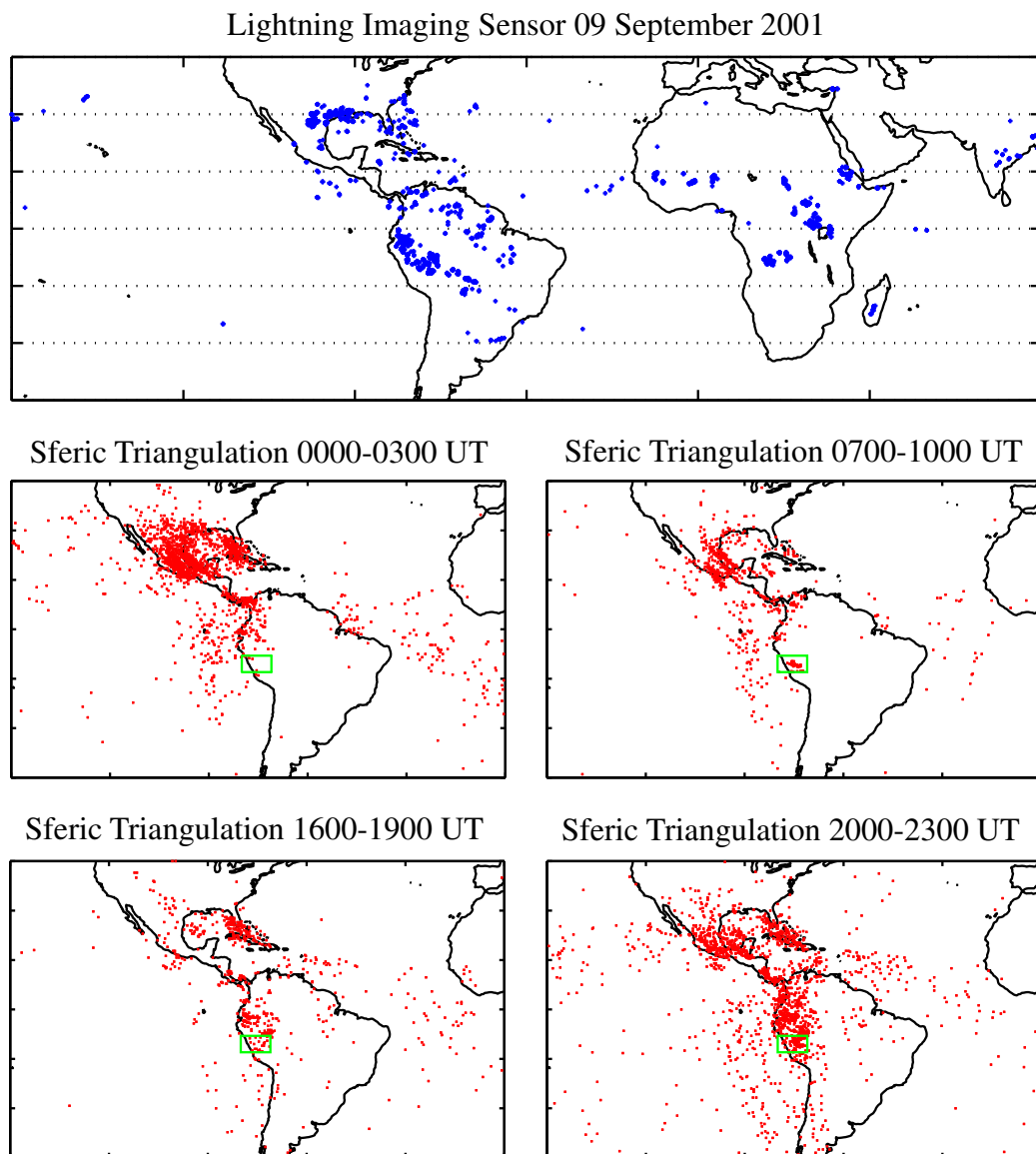


Figure 4.12: Comparison of triangulated lightning source locations to LIS lightning flashes.

the triangulation algorithm. The bottom four panels show lightning locations from 0000–0300 UT, 0700–1000 UT, 1600–1900 UT and 2000–2300 UT on 9 September 2001. These time periods were selected to show how lightning activity varies over the course of the day in different regions. For example, during the 0000–0300 UT period there is a lot of lightning activity in and around Mexico. This activity is not visible in the LIS data because the LIS passes over Mexico occurred later in the day at around 1200 UT and 1800 UT. However, the minimal lightning activity around Mexico in the LIS data around 1800 UT is consistent with the panel showing the triangulated lightning from 1600–1900 UT. Mismatch errors are also visible in the triangulated lightning data off the west coast of South America. Notice that more mismatch errors, seen as an increase in the number of scattered, non-clustered events, occur during times of increased lightning activity such as during the 0000–0300 UT and 2000–2300 UT time periods. In contrast, fewer mismatch errors occur during the periods of lighter lightning activity such as during the 0700–1000 UT and 1600–1900 UT time periods.

Once again, due to the synoptic style recording scheme and the occasional system failures at the Vieques Island receiver site, it is difficult to find LIS passes that are in range of the receivers for times for which data are available. However, one pass over South America occurred for which performance statistics could be derived. At 0550 UT on 10 September 2001 the LIS instrument passed over the point near 11° S latitude and 72° W longitude. During this time, LIS detected 121 flashes. Of these flashes 25, or 21%, were matched to within 2 ms of an event located by the triangulation algorithm. The matches are made to the time of the largest “group” in each LIS flash. The median location error for the 25 matched events is 188 km which is about a factor of two worse than the expected median location error for this region, ~ 75 km, as predicted by simulation.

The triangulation technique described above can also be used to continuously monitor a particular area over the course of several days. In Figure 4.12, the green rectangles visible in South America span the region from 8° S to 13° S and from 71° W to 80° W. This area was selected because a localized cluster of events is often visible here in the data without a lot of extraneous, possibly erroneous, events around

it. Thus, it is hoped that the event rate for this area can be studied without the inclusion of erroneously located or mismatched events. This area also contains the region for which LIS data were matched to triangulated events. In conjunction with another experiment [Pasko *et al*, 2002], data were acquired at both Palmer Station and Vieques Island from 0000 – 1000 UT and 1630 – 2400 UT over the course of several days. No data were collected from 1000 – 1630 UT because the Arecibo radio telescope, which was being used as part of the other experiment, was not available during this time. The data were acquired for 1-min intervals at 5, 20, 35 and 50 minutes past each hour. This synoptic recording schedule was used because the system had limited storage capacity and had to operate autonomously for several days. Furthermore, some of the synoptic data files were corrupted and not suitable for analysis. For each 1-min interval the sferics with triangulated locations falling within the rectangular area were counted. Figure 4.13 shows the sferic counts from 0000 UT on 7 September 2001 to 1000 UT on 10 September 2001. Initially, for the first 46 hours of observation, very few events are located within the area of interest. However, subsequently there is a noticeable increase in event occurrence during the synoptic periods over the next 16 hours. There is then an even more remarkable increase in the event occurrence rate during the next 24 hours after that. The highest event rate occurs at 0705 UT on 10 September 2001 with 68 sferics located in the region during this minute.

Also of interest in Figure 4.13 is the daily cycle of sferic occurrence that is visible during the final 40 hours of observation. Starting at 1800 UT on 8 September 2001 there is a lull in the event occurrence rate. The lull is followed in time by a small peak in the event rate that occurs at ~ 2100 UT. This peak is in turn followed by another lull at ~ 0130 UT and is then followed by a larger peak at 0700 UT. Coincidentally this exact same pattern of lulls and peaks is repeated again starting at 1800 UT on 9 September 2001, except that this time the magnitude of the peaks is larger. Unfortunately, once again data are not available during the next 24 hours in order to see if this pattern repeats again. This daily variation in sferic occurrence is similar to the daily electric field variations seen aboard the HMS Carnegie during its voyage [Chalmers, 1967] in that the variation appears to repeat over a 24 hour

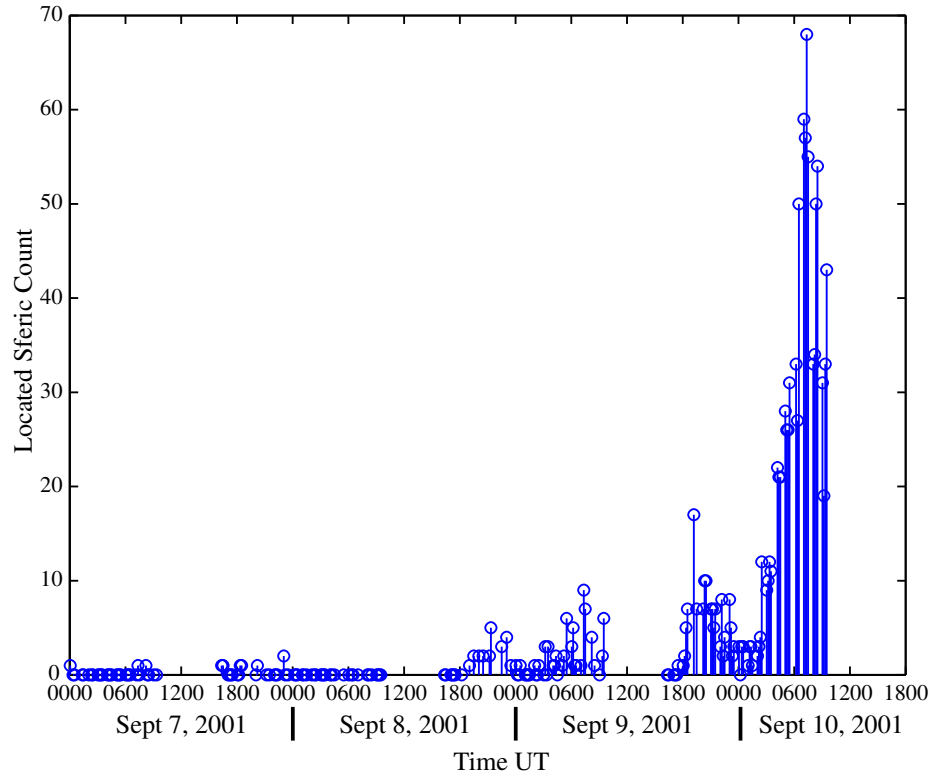


Figure 4.13: Sferic Count for region bounded by 8° S and 13° S latitude and 71° W and 80° W longitude.

period. However, the double peak is inconsistent with the so-called Carnegie curve. Similar diurnal variations in lightning activity were also seen by *Zajac and Rutledge* [2001] in North America and by *Pinto et al.* [1999] in Brazil.

4.5 Three Station Triangulation

The same type of algorithm used to triangulate lightning events using two stations can be expanded to triangulate lightning using three or more stations. The use of more stations is desirable because the more receivers used in the geolocation algorithm the more of the globe can be covered and the better is the location accuracy. For example, if a sferic is detected at three different receiver sites as opposed to just two

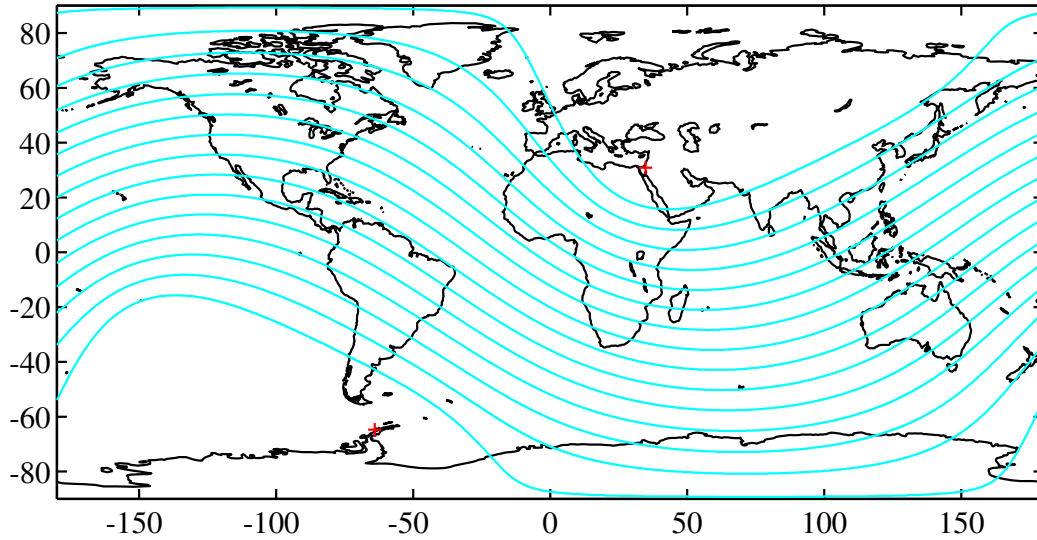


Figure 4.14: Equal time of arrival difference curves between Palmer Station and Sde Boker.

receiver sites, there then exists six measurements (three arrival azimuths and three TOA differences) that can be used in the triangulation algorithm as opposed to just three measurements. In the general case for N stations there would be $N + \binom{N}{2}$ measurements. The azimuth lines for three stations are distributed in the same manner (i.e., as in Figure 4.2) as they do for two stations. A few complications do arise however when using the TOA difference lines from three stations. Figures 4.14, 4.15 and 4.16 show the TOA difference lines between Palmer Station and Sde Boker, Palmer Station and Upland, and Sde Boker and Upland respectively. For the two receiver case using the receivers at Palmer Station and Vieques Island island, the only problem areas in the array were due north of Vieques Island and due south of Palmer Station. The area south of Palmer Station was not really a problem since there typically is no lightning generated in this Antarctic region. The region north of Vieques Island is a problem area because, in this region, TOA difference measurements start to become meaningless. That is to say, a very small error in the TOA difference measurement results in a very large error in location due to the geometry of the two sites. Now that three sites are involved, there are only a few regions of the Earth

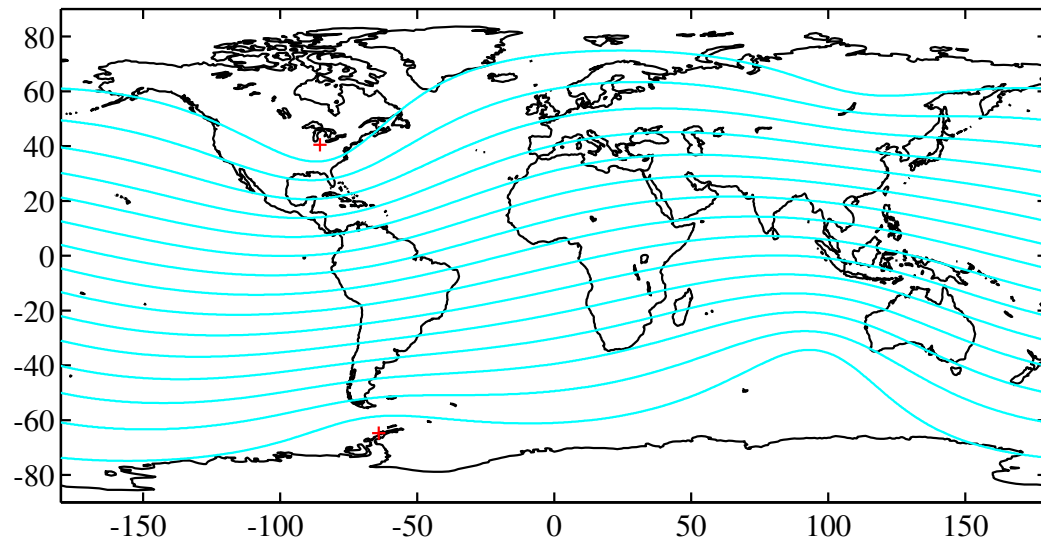


Figure 4.15: Equal time of arrival difference curves between Palmer Station and Upland.

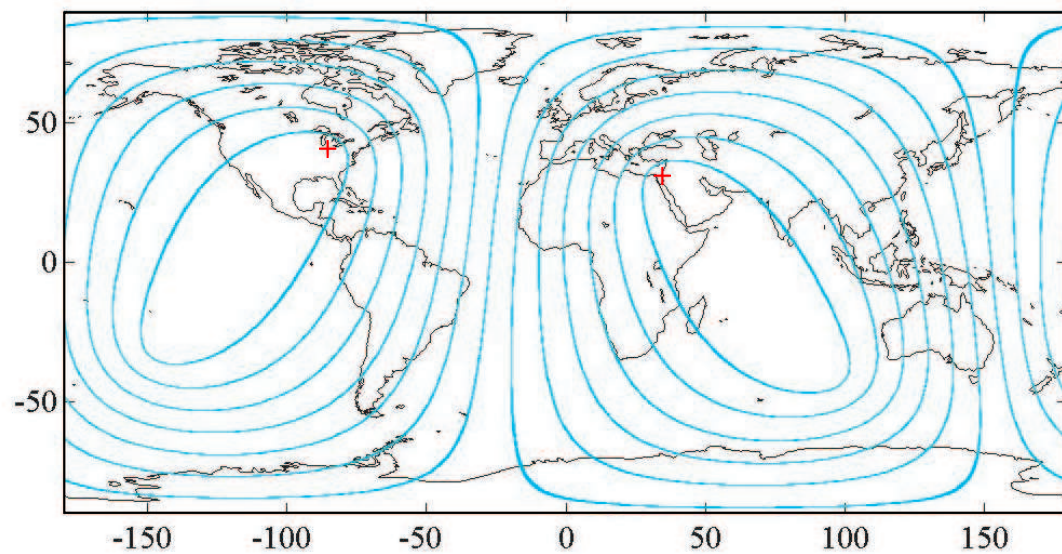


Figure 4.16: Equal time of arrival difference curves between Upland and Sde Boker.

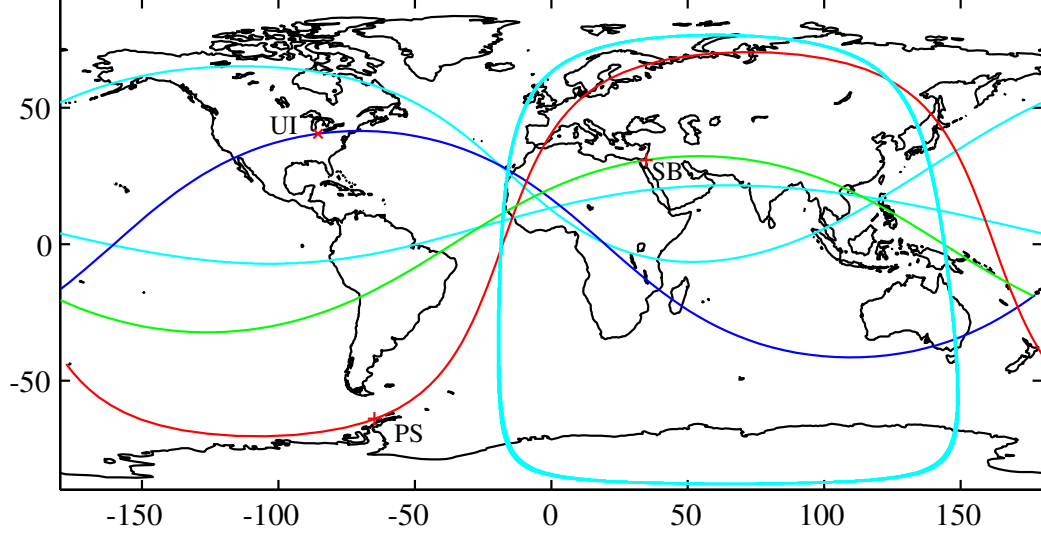


Figure 4.17: Azimuth Lines and TOAD curves for three station triangulation.

that are not in a problem area for at least one pairing of sites. For example, for the Palmer Station-Sde Boker pairing (Figure 4.14), the main problem area is eastern Europe and Asia as is shown by the lack of TOA difference curves in this area. For the Palmer Station-Upland pairing (Figure 4.15), the problem area is in the northern part of North America. The worst pairing is the Sde Boker-Upland pairing (Figure 4.16), where the problem area lies in the lightning active region of the central United States and Mexico.

When using three stations for triangulation, the three azimuth lines and three TOA difference lines no longer form triangles but constitute a density of lines instead. Lines for an example lightning discharge in Africa are shown in Figure 4.17. From this, we can construct a chi-square function which works just as for two stations except that there now are six measurements instead of three. The generalized chi-square function for N stations is given below

$$\chi^2 = \sum_{n=1}^N c_n (\theta_{\text{meas}_n} - \theta_{\text{ideal}_n})^2 + \sum_{n=1}^{N-1} \sum_{m=n+1}^N d_{n,m} (\Delta t_{\text{meas}_{n,m}} - \Delta t_{\text{ideal}_{n,m}})^2 \quad (4.3)$$

where the double summation accounts for all possible pairings of sites.

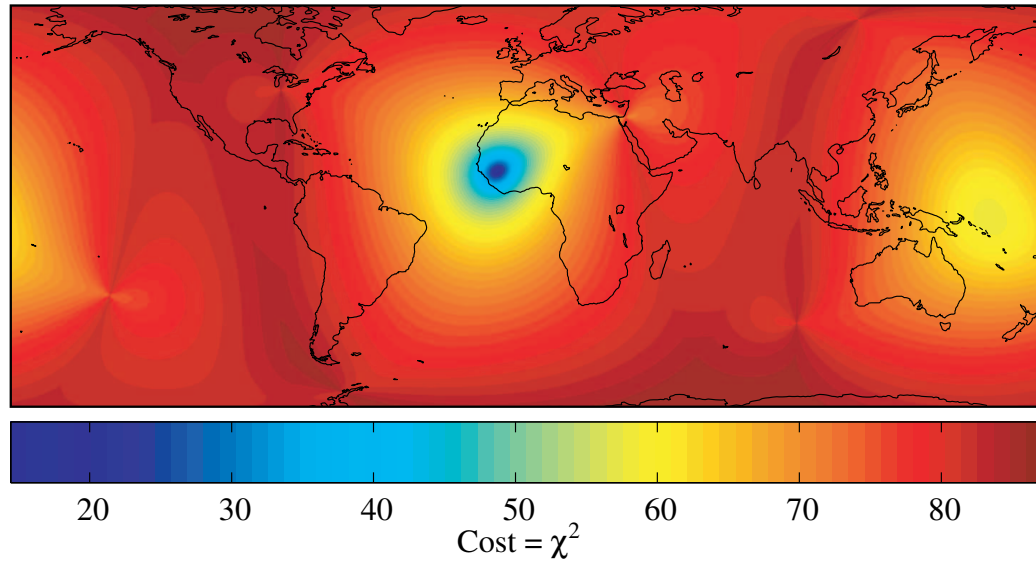


Figure 4.18: Three station chi-square cost map.

An additional advantage of three station triangulation comes in the reduction of antipodal errors. When using two stations, the azimuth lines and TOA difference line converge at two points on antipodal sides of the earth creating potential errors as discussed in a Section 4.3.2. With three stations, as the measurement lines converge at the lightning source on one side of the earth, they do not converge as well on the antipodal side. Figure 4.18 shows the chi-square error surface for the measurement scenario shown in Figure 4.17. Notice that much like the chi-square surface of Figure 4.6 there is a minimum around the lightning source location. However, the minimum on the antipodal side of the earth is much less pronounced than it was for two station triangulation (Figure 4.6).

4.6 Three Station Triangulation Observations

Figure 4.19 shows the density of cloud-to-ground lightning flashes detected by the NLDN from 0000-2400 UT on 01 August 2002. Lower flash density is shown by blue pixels while higher flash density is shown by yellow and red pixels. The red cross in the figure represents the location of the Upland, Indiana receiver site. Notice that

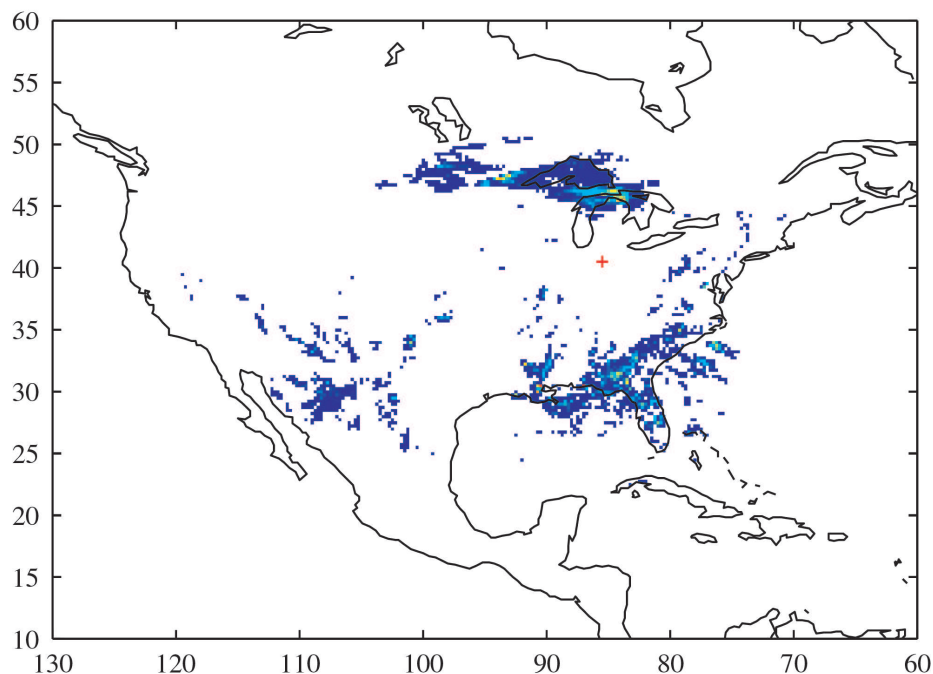


Figure 4.19: NLDN flash density for 0000 – 2400 UT, 01 August 2002.

there are three major regions of lightning activity. One to the north of the Upland site, one in the midwest and the third being in and around Florida. The storm near Florida has an area of more intense activity illustrated by the yellow pixels in northern Florida. Unfortunately, the storm to the north of Upland is in the problem region for the Palmer Station-Upland site pairing (see Figure 4.15). In a similar fashion, the midwest storm is in the problem area for the Sde Boker-Upland site pairing (see Figure 4.14).

Figure 4.20 shows the density of lightning sources triangulated by matching sferics from the Palmer Station, Sde Boker and Upland sites from 0000-2400 UT on 01 August 2002. Notice that the only clustered areas of activity visible are near Florida and on the islands off the coast of Florida. Notice that, in Figure 4.20, there is significant lightning activity over Cuba and the Dominican Republic that is not visible in Figure 4.19. This lightning is not visible in Figure 4.19 because Cuba and the Dominican Republic are outside of the coverage area of the NLDN. For the same

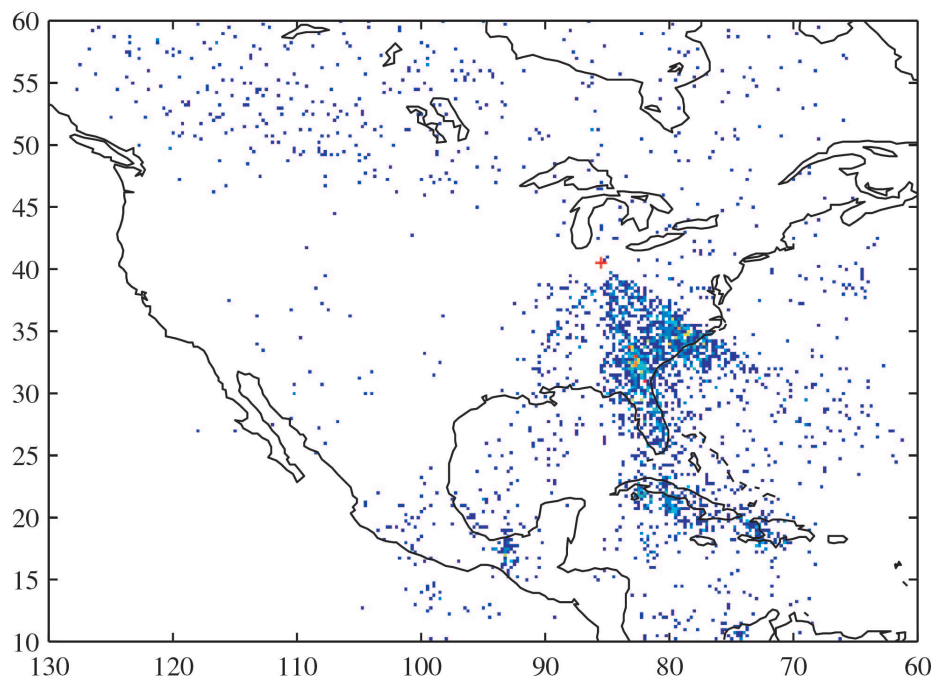


Figure 4.20: Three station triangulated event density 0000-2400 UT 01 August 2002.

reason, in Figure 4.20, there is lightning visible on the Yucatan peninsula that is not visible in Figure 4.19. The storms to the north of Upland, Indiana and in the midwest are not apparent. This result is due to large errors associated with the TOA differences to the Upland, Indiana site in these areas. Also notice that the most intense lightning region in Figure 4.20, illustrated by the yellow and red pixels, occurs in about the same location as the most intense lightning region in the NLDN data.

Chapter 5

Summary and Suggestions for Future Work

5.1 Summary

In this dissertation the ground work was laid for the development of a long range lightning detection system using the impulsive VLF waveforms of sferics. There are two primary concepts involved in developing this type of a lightning detection system. The first is the measurement of sferic arrival times and arrival azimuths to a high level of precision and the second is the development of an algorithm for combining measurements from multiple sites in order to determine locations of sources via triangulation.

Sferic arrival azimuths are calculated by measuring the ratio of the magnetic field amplitude impinging on two magnetic loop antennas and are compared to predicted azimuths of known lightning sources recorded by NLDN and LIS. Results show that the measured arrival azimuths are within $\sim 1\text{-}2^\circ$ of the expected ideal azimuths. Results also show that some of the arrival azimuths for sferics matched to events recorded by LIS events are 90° away from their expected azimuths. These sferics are believed to be generated by horizontal intra-cloud discharges whose arrival azimuths are expected to have a 90° discrepancy since they are primarily composed of QTE mode waves while our arrival azimuth determination method presumes QTM mode waves.

Monitoring of sferic arrival azimuths was shown to be an effective tool for monitoring regional thunderstorm activity on a gross scale by creating histograms of the arrival azimuths over an extended period of time. Histograms such as that in Figure 3.16 reveal a great amount of clustering in the arrival azimuths of sferics indicating thunderstorms occurring in various regions around the world. We have also shown that under the right circumstances, the lightning activity in an individual thunderstorm could be monitored with high resolution. Application of this method to an example case revealed that the amount of intra-cloud lightning activity in a storm may be a proxy indicator of the amount of cloud-to-ground lightning that will be produced.

A triangulation algorithm was developed for locating individual lightning discharges using both arrival azimuth measurements and time of arrival difference measurements from very widely spaced sites ($\sim 10,000$ km). A major challenge in the development of this algorithm was the development of a method to combine the arrival azimuth and time of arrival information in a meaningful way. This problem was solved by the use of a lookup table where idealized values for arrival azimuths and time of arrival differences were pre-computed for all locations on Earth. The most likely location for a lightning discharge was then determined by comparing the real azimuth and time of arrival measurements to the ideal values.

The triangulation algorithm was also complicated by the wide spacing of the receiver elements. The great distances between sites created ambiguities in matching sferics at different sites to their unique lighting source. This problem was solved by using a brute force method to triangulate all possible sferic matches and choosing the most likely solution (based on an error criteria) from those matches.

Triangulation results were compared to known lightning locations from the NLDN and LIS. Triangulated event sources were located to within ~ 200 km of the actual sources from a range of $\sim 10,000$ km with a detection efficiency approaching 50%.

5.2 Future Research Suggestions

5.2.1 Direction Finding Improvements

At the most basic level, the best way to improve the location accuracy of the lightning detection system is to improve the accuracy of the spheric azimuth determination. The current method for determining arrival azimuths uses an average of the arrival azimuths of individual frequency components and weighs these azimuths by the signal strengths for each of those frequency components. This method is most effective for sferics that have propagated a long distance through the Earth-ionosphere waveguide and that are therefore composed primarily of low order modes that are dominantly QTM in nature. Unfortunately, by averaging in this way, potentially valuable information about the arrival azimuth is lost. As mentioned in Chapter 2, each mode in the Earth-ionosphere waveguide is in fact a mixture of QTM and QTE modes. Interestingly, the mixing ratio, that is the ratio of energy of a sferic that is in QTM mode versus the energy that is in QTE mode, depends both on frequency and on the direction of propagation [*Snyder and Pappert, 1969*]. For example the lowest order mode for a sferic traveling eastward has a higher ratio of QTM/QTE energy than a sferic travelling westward. Thus a westward bound sferic has a higher polarization error associated with it that might be calculable. More research is needed to see how stable these errors might be under varying waveguide parameters such as day versus night propagation or under disturbed ionospheric conditions.

This type of analysis could also be taken a step further and be applied to sferics arriving from much closer distances. In such a case, the single dominant mode assumption is not appropriate and the polarization error caused by multiple modes must be considered in the arrival azimuth calculation. Unfortunately, the mode structure of individual sferics is probably highly dependent on the exact polarization of the source lightning discharge, rendering this approach ineffective. In general though, it would be better to have a mapping of a frequency versus arrival azimuth curve to a single arrival azimuth rather than to use a weighted average to arrive at the single arrival azimuth of a sferic.

Another area of direction finding that needs to be researched further is the determination of site error parameters. While measurements of the antenna dimensions are taken during calibration, these often serve mostly as a starting point for the determination of the effective site error parameters. A consistent algorithm needs to be developed that may involve a combination of calibration measurements, determination of VLF transmitter arrival azimuths and arrival azimuths from sferics with known origins. The determination of site error parameters is currently more of an art than a science and a more deterministic procedure for assessment of error parameters needs to be developed.

5.2.2 Triangulation Improvements

Lookup Table Improvements

Another way to improve the triangulation results is to make the lookup table more sophisticated. A simple way that the lookup table could be improved would be the inclusion of the effects of the day/night terminator on the group velocity in the waveguide. The current lookup table assumes a constant reflection height over the entire propagation path and thus a constant group velocity. However, if a sferic propagates under both daytime and nighttime conditions then its group velocity changes as it travels from day to night and vice versa. Implementation of this change in a lookup table would require that time of day be added as a third dimension to the lookup table. On a grander scale, the day of the year would need to be added to account for the seasonal change of the day/night terminator. These changes would affect the ideal TOA difference measurement in the lookup table grid points.

The use of a VLF propagation model such as LWPC [Ferguson *et al.*, 1989] could also be used to enhance the lookup table. In line with the improvements in direction finding, the use of the propagation model might make it possible to predict the effects of range on polarization errors. Thus each grid point along a certain great circle path might have a slightly different ideal azimuth. The VLF propagation model would also allow signal amplitude to be included in the chi-square function. The attenuation from a sferic source location to each site could be calculated and the ratio of the

sferic amplitudes at the different sites could be used as a parameter in the chi-square function. The receiver sites would have to be very carefully calibrated for such a method to be effective. Furthermore, as azimuth and TOA measurements become more precise the grid resolution could be made finer since the location accuracy would also be higher.

Conceptual Multi-Station Improvements

One improvement that is needed in the triangulation algorithm is the introduction of a method by which to decide the effective range for a particular receiver site. Some sites, such as Palmer Station, can detect much lower amplitude sferics than others, such as Vieques Island. Thus each site would have a coverage area associated with it within which measurements from that site can be used to locate sferics. The identification of a coverage area becomes more important as an algorithm is developed for a system with many sites around the world since most sferics are only detectable by a few stations, and the measurements from other stations should not be included in triangulating that sferic's location.

Alternative Location Method

In addition to triangulation, the location of a sferic can in principle also be determined by measuring the dispersion in the sferic waveform and using it to determine the range of the lightning source. The range combined with the arrival azimuth gives the location of the source lightning. This technique is used at ELF frequencies [Price and Asfur, 2002] and should in principle be applicable at VLF frequencies given a high enough sampling rate and large enough signal-to-noise ratio so as to allow the arrival time difference as a function of frequency to be determined.

Appendix A

Derivation of Equations

A.1 Great Circle Intersection

Imagine that the lines in Figure A.1 are actually great circle paths on the earth with the top intersection point being the North Pole. Points (σ_0, Ω_0) and (σ_1, Ω_1) are known receiver sites and point (σ, Ω) is located at the intersection of great circle paths δ_o and δ_1 which are at azimuths α_o and α_1 from the two receiver sites respectively.

First start with basic relations for longitude:

$$\Delta\Omega_d = \Omega_1 - \Omega_o \quad (\text{A.1})$$

$$\Delta\Omega_o = \Omega - \Omega_o \quad (\text{A.2})$$

$$\Delta\Omega_1 = \Omega - \Omega_1 \quad (\text{A.3})$$

Next use Napier's Analogies to determine the angles θ_0 , θ_1 and θ_2 [Ballou and Steen, 1953]:

$$\tan \left[\frac{1}{2} (\theta_1 - \theta_0) \right] = \cot \left(\frac{1}{2} \Delta\Omega_d \right) \frac{\sin \left[\frac{1}{2} \left(\frac{\pi}{2} - \sigma_0 - \frac{\pi}{2} + \sigma_1 \right) \right]}{\sin \left[\frac{1}{2} \left(\frac{\pi}{2} - \sigma_0 + \frac{\pi}{2} - \sigma_1 \right) \right]}$$

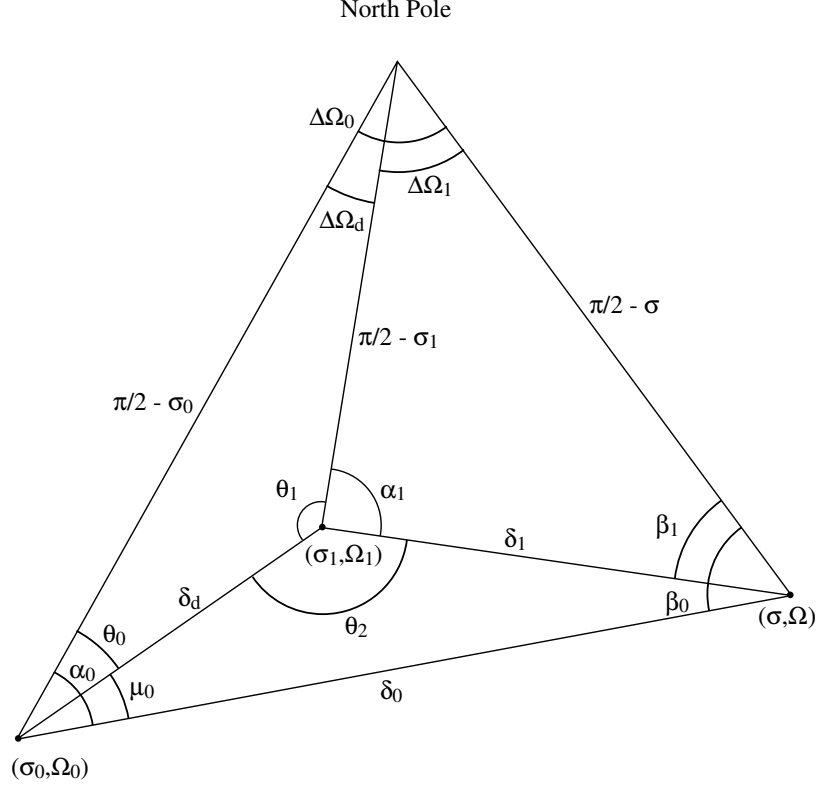


Figure A.1: Linearized Plot of Spherical Geometry.

$$\tan \left[\frac{1}{2} (\theta_1 + \theta_0) \right] = \cot \left(\frac{1}{2} \Delta \Omega_d \right) \frac{\cos \left[\frac{1}{2} \left(\frac{\pi}{2} - \sigma_0 - \frac{\pi}{2} + \sigma_1 \right) \right]}{\cos \left[\frac{1}{2} \left(\frac{\pi}{2} - \sigma_0 + \frac{\pi}{2} - \sigma_1 \right) \right]} \quad (\text{A.4})$$

$$\theta_1 = \frac{1}{2} (\theta_1 - \theta_0) + \frac{1}{2} (\theta_1 + \theta_0) \quad (\text{A.5})$$

$$\begin{aligned} \theta_1 = & \arctan \left\{ \cot \left(\frac{1}{2} \Delta \Omega_d \right) \frac{\sin \left[\frac{1}{2} (\sigma_1 - \sigma_0) \right]}{\cos \left[\frac{1}{2} (\sigma_1 + \sigma_0) \right]} \right\} \\ & + \arctan \left\{ \cot \left(\frac{1}{2} \Delta \Omega_d \right) \frac{\cos \left[\frac{1}{2} (\sigma_1 - \sigma_0) \right]}{\sin \left[\frac{1}{2} (\sigma_1 + \sigma_0) \right]} \right\} \end{aligned} \quad (\text{A.6})$$

$$\theta_0 = \frac{1}{2} (\theta_1 + \theta_0) - \frac{1}{2} (\theta_1 - \theta_0) \quad (\text{A.7})$$

$$\begin{aligned} \theta_0 = & \arctan \left\{ \cot \left(\frac{1}{2} \Delta \Omega_d \right) \frac{\cos \left[\frac{1}{2} (\sigma_1 - \sigma_0) \right]}{\sin \left[\frac{1}{2} (\sigma_1 + \sigma_0) \right]} \right\} \\ & - \arctan \left\{ \cot \left(\frac{1}{2} \Delta \Omega_d \right) \frac{\sin \left[\frac{1}{2} (\sigma_1 - \sigma_0) \right]}{\cos \left[\frac{1}{2} (\sigma_1 + \sigma_0) \right]} \right\} \end{aligned} \quad (\text{A.8})$$

$$\theta_2 = 2\pi - \alpha_1 - \theta_1 \quad (\text{A.9})$$

Next use Napier's Analogies to determine the arc lengths δ_d , δ_0 and δ_1 :

$$\mu_0 = \alpha_0 - \theta_0 \quad (\text{A.10})$$

$$\tan \left(\frac{1}{2} \delta_d \right) = \tan \left[\frac{1}{2} \left(\frac{\pi}{2} - \sigma_0 - \frac{\pi}{2} + \sigma_1 \right) \right] \frac{\sin \left[\frac{1}{2} (\theta_1 + \theta_0) \right]}{\sin \left[\frac{1}{2} (\theta_1 - \theta_0) \right]} \quad (\text{A.11})$$

$$\begin{aligned} \tan \left[\frac{1}{2} (\delta_0 - \delta_1) \right] &= \tan \left(\frac{1}{2} \delta_d \right) \frac{\sin \left[\frac{1}{2} (\theta_2 - \mu_0) \right]}{\sin \left[\frac{1}{2} (\theta_2 + \mu_0) \right]} \\ \tan \left[\frac{1}{2} (\delta_0 + \delta_1) \right] &= \tan \left(\frac{1}{2} \delta_d \right) \frac{\cos \left[\frac{1}{2} (\theta_2 - \mu_0) \right]}{\cos \left[\frac{1}{2} (\theta_2 + \mu_0) \right]} \end{aligned} \quad (\text{A.12})$$

$$\delta_0 = \frac{1}{2} (\delta_0 - \delta_1) + \frac{1}{2} (\delta_0 + \delta_1) \quad (\text{A.13})$$

$$\begin{aligned} \delta_0 = & \arctan \left\{ \tan \left(\frac{1}{2} \delta_d \right) \frac{\sin \left[\frac{1}{2} (\theta_2 - \mu_0) \right]}{\sin \left[\frac{1}{2} (\theta_2 + \mu_0) \right]} \right\} \\ & + \arctan \left\{ \tan \left(\frac{1}{2} \delta_d \right) \frac{\cos \left[\frac{1}{2} (\theta_2 - \mu_0) \right]}{\cos \left[\frac{1}{2} (\theta_2 + \mu_0) \right]} \right\} \end{aligned} \quad (\text{A.14})$$

$$\delta_1 = \frac{1}{2} (\delta_0 + \delta_1) - \frac{1}{2} (\delta_0 - \delta_1) \quad (\text{A.15})$$

$$\delta_1 = \arctan \left\{ \tan \left(\frac{1}{2} \delta_d \right) \frac{\cos \left(\frac{1}{2} (\theta_2 - \mu_0) \right)}{\cos \left(\frac{1}{2} (\theta_2 + \mu_0) \right)} \right\}$$

$$+ \arctan \left\{ \tan \left(\frac{1}{2} \delta_d \right) \frac{\sin \left(\frac{1}{2} (\theta_2 - \mu_0) \right)}{\sin \left(\frac{1}{2} (\theta_2 + \mu_0) \right)} \right\} \quad (\text{A.16})$$

Use Napier's Analogies once again to determine angles $\Delta\Omega_0$ and β_0 :

$$\begin{aligned} \tan \left[\frac{1}{2} (\Delta\Omega_0 - \beta_0) \right] &= \cot \left(\frac{1}{2} \alpha_0 \right) \frac{\sin \left[\frac{1}{2} \left(\delta_0 - \frac{\pi}{2} + \sigma_0 \right) \right]}{\sin \left[\frac{1}{2} \left(\delta_0 + \frac{\pi}{2} - \sigma_0 \right) \right]} \\ \tan \left[\frac{1}{2} (\Delta\Omega_0 + \beta_0) \right] &= \cot \left(\frac{1}{2} \alpha_0 \right) \frac{\cos \left[\frac{1}{2} \left(\delta_0 - \frac{\pi}{2} + \sigma_0 \right) \right]}{\cos \left[\frac{1}{2} \left(\delta_0 + \frac{\pi}{2} - \sigma_0 \right) \right]} \end{aligned} \quad (\text{A.17})$$

$$\Delta\Omega_0 = \frac{1}{2} (\Delta\Omega_0 - \beta_0) + \frac{1}{2} (\Delta\Omega_0 + \beta_0) \quad (\text{A.18})$$

$$\begin{aligned} \Delta\Omega_0 &= \arctan \left\{ \cot \left(\frac{1}{2} \alpha_0 \right) \frac{\sin \left[\frac{1}{2} \left(\delta_0 - \frac{\pi}{2} + \sigma_0 \right) \right]}{\sin \left[\frac{1}{2} \left(\delta_0 + \frac{\pi}{2} - \sigma_0 \right) \right]} \right\} \\ &+ \arctan \left\{ \cot \left(\frac{1}{2} \alpha_0 \right) \frac{\cos \left[\frac{1}{2} \left(\delta_0 - \frac{\pi}{2} + \sigma_0 \right) \right]}{\cos \left[\frac{1}{2} \left(\delta_0 + \frac{\pi}{2} - \sigma_0 \right) \right]} \right\} \end{aligned} \quad (\text{A.19})$$

$$\beta_0 = \frac{1}{2} (\Delta\Omega_0 + \beta_0) - \frac{1}{2} (\Delta\Omega_0 - \beta_0) \quad (\text{A.20})$$

$$\begin{aligned} \beta_0 &= \arctan \left\{ \cot \left(\frac{1}{2} \alpha_0 \right) \frac{\cos \left[\frac{1}{2} \left(\delta_0 - \frac{\pi}{2} + \sigma_0 \right) \right]}{\cos \left[\frac{1}{2} \left(\delta_0 + \frac{\pi}{2} - \sigma_0 \right) \right]} \right\} \\ &- \arctan \left\{ \cot \left(\frac{1}{2} \alpha_0 \right) \frac{\sin \left[\frac{1}{2} \left(\delta_0 - \frac{\pi}{2} + \sigma_0 \right) \right]}{\sin \left[\frac{1}{2} \left(\delta_0 + \frac{\pi}{2} - \sigma_0 \right) \right]} \right\} \end{aligned} \quad (\text{A.21})$$

Finally, a Napier Analogy can be used to determine the latitude, σ

$$\tan \left[\frac{1}{2} \left(\frac{\pi}{2} - \sigma \right) \right] = \tan \left[\frac{1}{2} \left(\delta_0 - \frac{\pi}{2} + \sigma_0 \right) \right] \frac{\sin \left[\frac{1}{2} (\Delta\Omega_0 + \beta_0) \right]}{\sin \left[\frac{1}{2} (\Delta\Omega_0 - \beta_0) \right]} \quad (\text{A.22})$$

And longitude, Ω is now also easily solved for

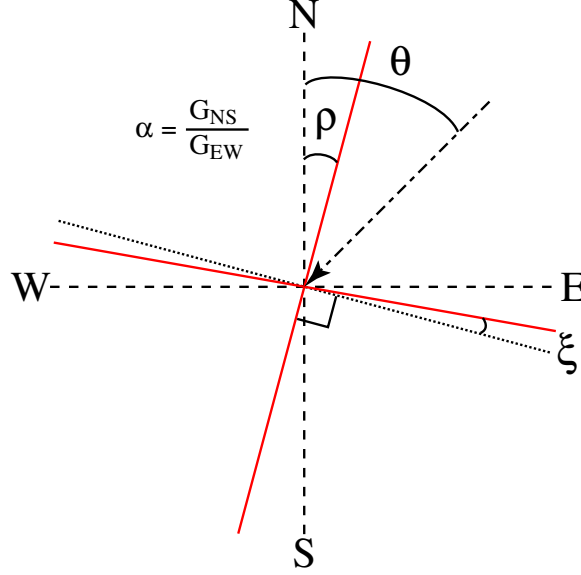


Figure A.2: Antenna Distortion Parameters

$$\Omega = \Delta\Omega_0 + \Omega_0 \quad (\text{A.23})$$

A.2 Derivation of Antenna Parameters

Using the antenna geometry from Figure A.2, the equation for correcting site error due to antenna imperfections is derived as follows. Given a signal arriving from an azimuth θ , the signals on the N/S and E/W channels are

$$\begin{aligned} S_{\text{NS}} &= G_{\text{NS}} \cos(\theta_{\text{true}} - \rho) \\ S_{\text{EW}} &= G_{\text{EW}} \sin(\theta_{\text{true}} - \rho + \xi) \end{aligned} \quad (\text{A.24})$$

where G_{NS} and G_{EW} are the gains of the N/S and E/W channels respectively. Also, ρ is the antenna rotation and ξ is the antenna skew of the E/W antenna relative to the N/S antenna. From these equations, the tangent of the calculated arrival azimuth,

θ_{calc} , is the ratio of these two signals

$$\tan(\theta_{\text{calc}}) = \frac{S_{\text{EW}}}{S_{\text{NS}}} = \frac{G_{\text{EW}} \sin(\theta_{\text{true}} - \rho + \xi)}{G_{\text{NS}} \cos(\theta_{\text{true}} - \rho)} \quad (\text{A.25})$$

which, after using a few trigonometric identities, is

$$\tan(\theta_{\text{calc}}) = \frac{G_{\text{EW}}}{G_{\text{NS}}} \frac{\sin(\theta_{\text{true}} - \rho) \cos(\xi) + \cos(\theta_{\text{true}} - \rho) \sin(\xi)}{\cos(\theta_{\text{true}} - \rho)} \quad (\text{A.26})$$

Using the substitution

$$\alpha = \frac{G_{\text{NS}}}{G_{\text{EW}}} \quad (\text{A.27})$$

and simplifying gives the equation

$$\alpha \tan(\theta_{\text{calc}}) = \tan(\theta_{\text{true}} - \rho) \cos(\xi) + \sin(\xi) \quad (\text{A.28})$$

and then solving for θ_{true} gives the equation for the corrected arrival azimuth

$$\theta_{\text{true}} = \arctan \left[\alpha \frac{\tan(\theta_{\text{calc}})}{\cos(\xi)} - \tan(\xi) \right] + \rho \quad (\text{A.29})$$

Bibliography

- [*Ballou and Steen*, 1953] Ballou, D. H. and F. H. Steen, *Plane and Spherical Trigonometry with Tables*, Ginn and Company, Boston, 1953.
- [*Barr*, 1971] Barr, R., The propagation of ELF and VLF radio waves beneath an inhomogeneous anisotropic ionosphere, *Journal of Atmospheric and Terrestrial Physics*, *33*, 343-353, 1971.
- [*Berger et al.*, 1975] Berger, K., R. B. Anderson and H. Kroninger, Parameters of Lightning Flashes, *Electra*, *80*, 23-37, 1975.
- [*Boccippio et al.*, 2002] Boccippio, D. J., W. J. Koshak and R. J. Blakeslee, Performance assessment of the Optical Transient Detector and Lightning Imaging Sensor: 1. Predicted diurnal variability, *Journal of Atmospheric and Oceanic Technology*, 1-19, 5 August 2002.
- [*Brooks*, 1925] Brooks, C. E. P., The Distribution of Thunderstorms Over the Globe, *Geophysical Memoirs*, *3*, No. 24, 147-164, 1925.
- [*Budden*, 1961] Budden, K. G., *The Wave-Guide Mode Theory of Wave Propagation*, Logos Press, London, 1961.
- [*Budden*, 1962] Budden, K. G., The influence of the earth's magnetic field on radio propagation of wave-guide modes, *Proceedings of the Royal Society A*, *265*, 538, 1962.

- [Burgess, 1993] Burgess, W.C., *Lightning-Induced Coupling of the Radiation Belts to Geomagnetically Conjugate Ionospheric Regions*, Ph.D. Thesis, Stanford University Department of Electrical Engineering, March 1993.
- [Burke and Jones, 1992] Burke, C. P. and D. L. Jones, An experimental investigation on ELF attenuation rates in the Earth-ionosphere duct, *Journal of Atmospherica and Terrestrial Physics*, 54, p. 243, 1992.
- [Burke and Jones, 1995] Burke, C. P. and D. L. Jones, Global radiolocation in the lower ELF frequency band, *Journal of Geophysical Research*, 100, 26263-26271, 1995.
- [Burton and Boardman, 1933] Burton, E. T. and E. M. Boardman, Audio-Frequency Atmospherics, *Proceedings of the Institute of Radio Engineers*, 21, 1476-1494, 1933.
- [Chalmers, 1967] Chalmers, J. A., *Atmospheric Electricity*, Pergamon Press, Oxford, New York, 1967.
- [Chapman and Pierce, 1957] Chapman, F. W. and E. T. Pierce, Relations Between the Character of Atmospherics and Their Place of Origin, *Proceedings of the Institute of Radio Engineers*, 45, 804-806, 1957.
- [Chrissan, 1998] Chrissan, Doug, *Statistical Analysis and Modeling of Low-Frequency Radio Noise and Improvement of Low-Frequency Communications*, PhD Thesis, Technical Report D179-1, Stanford University, 1998.
- [Christian et al., 1999a] Christian, H. J., R. J. Blakeslee, D. J. Boccippio, W. L. Boeck, D. E. Buechler, K. T. Driscoll, S. J. Goodman, J. M. Hall, W. J. Koshak, D. M. Mach and M. F. Stewart, Global Frequency and Distribution of Lightning as Observed By the Optical Transient Detector (OTD), *Proceedings of the 11th International Conference on Atmospheric Electricity*, Gunthersville, Alabama, 726-729, 1999.
- [Christian et al., 1999b] Christian, H. J., R. J. Blakeslee, S. J. Goodman, D. A. Mach, M. F. Stewart, D. E. Buechler, W. J. Koshak, J. M. Hall, W. L. Boeck, K. T.

- Driscoll and D. J. Boccipio, The Lightning Imaging Sensor, *Proceedings of the 11th International Conference on Atmospheric Electricity*, Gunthersville, Alabama 746-749, 1999.
- [*Christian et al.*, 2003] Christian, H. J., R. J. Blakeslee, D. J. Boccippio, W. L. Boeck, D. E. Buechler, K. T. Driscoll, S. J. Goodman, J. M. Hall, W. J. Koshak, D. M. Mach and M. F. Stewart, Global frequency and distribution of lightning as observed from space by the Optical Transient Detector, *Journal of Geophysical Research*, *108*, D1, 4005-4019, 2003.
- [*Cummer*, 1997] Cummer, S. A., *Lightning and Ionospheric Remote Sensing Using VLF/ELF Radio Atmospherics*, Ph.D. Thesis, Stanford University Department of Electrical Engineering, September 1997.
- [*Cummins et al.*, 1998] Cummins, K. L., M. J. Murphy, E. A. Bardo, W. L. Hiscox, R. B. Pyle and A. E. Pifer, A Combined TOA/MDF Technology Upgrade of the U. S. National Lightning Detection Network, *Journal of Geophysical Research*, *103*, 9035-9044, April 27, 1998.
- [*Davies*, 1990] Davies, K., *Ionospheric Radio*, Peregrinus, London, 1990.
- [*Dowden et al.*, 2002] Dowden, R. L., J. B. Brundell and C. J. Rodger, VLF lightning location by time of group arrival (TOGA) at multiple sites, *Journal of Atmospheric and Solar-Terrestrial Physics*, *64*, 817-830, 2002.
- [*Ferguson and Snyder*, 1980] Ferguson, J. A., and F. P. Snyder, Approximate VLF/LF Waveguide Mode Conversion Model, *Technical Document 400*, Naval Oceans Systems Center, San Diego, California, 1980.
- [*Ferguson et al.*, 1989] Ferguson, J. A., F. P. Snyder, D. G. Morfett and C. H. Shellman, Long-wave propagation capability and documentation, *Technical Document 1518*, Naval Ocean Systems Center, San Diego, California, 1989.
- [*Fullerkrug and Constable*, 2000] Fullerkrug, M. and S. Constable, Global Triangulation of Intense Lightning Discharges, *Geophysical Research Letters*, *27*, 333-336, 2000.

- [Galejs, 1972] Galejs, J., *Terrestrial Propagation of Long Electromagnetic Waves*, Pergamon Press, Oxford, 1972.
- [Hargreaves, 1992] Hargreaves, J. K., *The Solar-Terrestrial Environment*, Cambridge, Cambridge University Press, 1992.
- [Helliwell, 1965] Helliwell, R. A., *Whistlers and Related Ionospheric Phenomena*, Stanford University Press, Stanford, California, 1965.
- [Hines et al., 1965] Hines, C. O., I. Paghis, T. R. Hartz and J. A. Fejer, *Physics of the Earth's Upper Atmosphere*, Englewood Cliffs, N. J., Prentice Hall, 1965.
- [Hiscox et al., 1984] Hiscox, W. L., E. P. Krider, A. E. Pifer and M. A. Uman, A systematic method for identifying and correcting "site errors" in a network of magnetic direction finders, paper presented at the International Aerospace and Ground Conference on Lightning and Static Electricity, National Interagency Coord. Group, National Atmospheric Electrical Hazard Program, Orlando, Florida, June 26-28, 1984.
- [Horner, 1954] Horner, F., The Accuracy of the Location of Sources of Atmospherics by Radio Direction-Finding, *Proceedings of the Institute of Electrical Engineers*, 101, 383-390, 1954.
- [Horner and Clarke, 1955] Horner, F. and C. Clarke, Some waveforms of atmospherics and their use in the location of thunderstorms, *Journal of Atmospheric and Terrestrial Physics*, 7, 1-13, 1955.
- [Huang et al., 1999] Huang, E., E. Williams, R. Boldi, S. Heckman, W. Lyons, M. Taylor, T. Nelson and C. Wong, Criteria for sprites and elves based on Schumann resonance observations, *Journal of Geophysical Research*, 104, D14, 16943-16964, 1999.
- [Hughes and Gallenberger, 1974] Hughes, H. G. and R. J. Gallenberger, Propagation of extremely low-frequency (ELF) atmospherics over a mixed day-night path, *Journal of Atmospheric and Terrestrial Physics*, 36, 1643-1661, 1974.

- [Inan *et al.*, 1996] Inan, U. S., S. C. Reising, G. J. Fishman and J. M. Horack, On the association of terrestrial gamma-ray bursts with lightning and implications for sprites, *Geophysical Research Letters*, *23*, 1067-1070, 1996.
- [Inan and Inan, 2000] Inan, U. S. and A. S. Inan, *Electromagnetic Waves*, Prentice Hall, 2000.
- [Jones, 1967] Jones, D. L., Schumann resonances and ELF propagation for inhomogeneous isotropic ionosphere profiles, *Journal of Atmospheric and Terrestrial Physics*, *29*, 1037-1044, 1967.
- [Krehbiel, 1986] Krehbiel, P. R., The Electrical Structure of Thunderstorms, *The Earth's Electrical Environment*, 90-113, National Academy Press, Washington, D.C., 1986.
- [Krider *et al.*, 1976] Krider, E. P., R. C. Noggle and M. A. Uman, A Gated, Wide-band Magnetic Direction Finder for Lightning Return Strokes, *Journal of Applied Meteorology*, *15*, 301-306, 1976.
- [Krider and Guo, 1983] Krider, E. P. and C. Guo, The Peak Electromagnetic Power Radiated by Lightning Return Strokes, *Journal of Geophysical Research*, *88*, 8471-8474, 1983.
- [Lee, 1986] Lee, A. C. L., An experimental study on the remote location of lightning flashes using a VLF arrival time difference technique, *Quarterly Journal of the Royal Meteorological Society*, *112* 203-229, 1986.
- [Lee, 1990] Lee, A. C. L., Bias Elimination and Scatter in Lightning Location by the VLF Arrival Time Difference Technique, *Journal of Atmospheric and Oceanic Technology*, *7*, 719-733, 1990.
- [Lewis *et al.*, 1960] Lewis, E. A., R. B. Harvey and J. E. Rasmussen, Hyperbolic Direction Finding with Sferics of Transatlantic Origin, *Journal of Geophysical Research*, *65*, 1879-1905, 1960.

- [Mach et al., 1986] Mach, D. M., D. R. MacGorman and W. D. Rust, Site Errors and Detection Efficiency in a Magnetic Direction-Finder Network for Locating Lightning Strikes to Ground, *Journal of Atmospheric and Oceanic Technology*, 3, 67-74, 1986.
- [Martin, 1965] Martin, H. G., The polarization of low frequency radio waves in the terrestrial wave-guide, *Journal of Atmospheric and Terrestrial Physics*, 27, 995-1007, 1965.
- [Orville and Spencer, 1979] Orville, R. E. and D. W., Spencer, Global Lightning Flash Frequency, *Monthly Weather Review*, 107, 934-943, 1979.
- [Orville, 1987] Orville, R. E. Jr., An Analytical Solution to Obtain the Optimum Source Location Using Multiple Direction Finders on a Spherical Surface, *Journal of Geophysical Research*, 92, 10877-10886, 1987.
- [Pappert and Ferguson, 1986] Pappert, R. A. and J. A. Ferguson, VLF/LF mode conversion model calculations for air to air transmissions in the earth-ionosphere waveguide, *Radio Science*, 21, 551, 1986.
- [Pascal, 1988] Pascal, E. W., *The Design of Broad-Band VLF Receivers with Air-Core Loop Antennas*, (internal report) Stanford University Space, Telecommunications and Radioscience Laboratory, Stanford, California, 1988.
- [Pasko et al, 2002] Pasko, V. P., M. A. Stanley, J. D. Mathews, U. S. Inan and T. G. Wood, Electrical discharge from a thundercloud top to the lower ionosphere, *Nature*, 416, 152-154, 2002.
- [Passi and Lopez, 1989] Passi, R. M. and R. E. Lopez, A Parametric Estimation of Systematic Errors in Networks of Magnetic Direction Finders, *Journal of Geophysical Research*, 94, 13319-13328, 1989.
- [Pinto et al., 1999] Pinto, I. R. C. A., O. Pinto Jr., R. M. L. Rocha, J. H. Diniz, A. M. Carvalho and A. C. Filho, Cloud-to-ground lightning in the southeastern

- Brazil in 1993, 2, Time variations and flash characteristics, *Journal of Geophysical Research*, 104, 31381-31387, 1999.
- [Porrat et al., 2001] Porrat, Dana, P. R. Bannister and A. C. Fraser-Smith, Modal phenomena in the natural electromagnetic spectrum below 5 kHz, *Radio Science*, Vol. 36, Num. 3, 499-506, 2001.
- [Prentice and Mackerras, 1977] Prentice, S. A. and D. Mackerras, The ratio of cloud to cloud-to-ground lightning flashes in thunderstorms, *Journal of Applied Meteorology*, 16, 545, 1977.
- [Price and Asfur, 2002] Price, C. and M. Asfur, An improved ELF/VLF method for globally geolocating sprite-producing lightning, *Geophysical Research Letters*, 29, 2002.
- [Rakov and Uman, 2003] Rakov, V. A. and M. A. Uman, *Lightning Physics and Effects*, Cambridge University Press, Cambridge, 2003.
- [Ramo et al., 1994] Ramo, S., J. R. Whinnery and T. Van Duzer, *Fields and Waves in Communications Electronics*, John Wiley and Sons, New York, 1994.
- [Rasmussen et al., 1980] Rasmussen, J. E., P. A. Kossey and E. A. Lewis, Evidence of an Ionospheric Reflecting Layer Below the Classical D Region, *Journal of Geophysical Research*, 85, 3037-3044, 1980.
- [Ratcliffe, 1959] Ratcliffe, J. A., *The Magneto-Ionic Theory and its Applications to the Ionosphere*, Cambridge University Press, Cambridge, 1959.
- [Reising, 1998] Reising, S. C., *Remote Sensing of the Electrodynamic Coupling Between Thunderstorm Systems and the Mesosphere/Lower Ionosphere*, Ph. D. Thesis, Stanford University, Stanford, California, 1998.
- [Reising et al., 1999] Reising, S. C., U. S. Inan and T. F. Bell, ELF spheric energy as a proxy indicator for sprite occurrence, *Geophysical Research Letters*, 26, 987-990, 1999.

- [*Rogers and Peden, 1975*] Rogers, J. C., I. C. Peden, The VLF complex permittivity of deep Antarctic ice measured in situ, *Radio Science*, 10, 763-771, 1975.
- [*Sato and Fukunishi, 2003*] Sato, Mitsuteru and Hiroshi Fukunishi, Global sprite occurrence locations and rates derived from triangulation of transient Schumann resonance events, *Geophysical Research Letters*, 30, 1859-1862, 2003.
- [*Snyder and Pappert, 1969*] Snyder, F. P. and R. A. Pappert, A parametric study of VLF modes below anisotropic ionospheres, *Radio Science*, 4, 213-226, 1969.
- [*Strangeways and Rycroft, 1980*] Strangeways, H. J. and M. J. Rycroft, Systematic errors in VLF direction-finding of whistler ducts, II, *Journal of Atmospheric and Terrestrial Physics*, 42, 1009, 1980.
- [*Stratton, 1941*] Stratton, J. A., *Electromagnetic Theory*, New York, McGraw Hill, 1941.
- [*Thomson, 1980*] Thomson, E. M., The dependence of lightning return stroke characteristics on latitude, *Journal of Geophysical Research*, 85, 1050-1056, 1980.
- [*Thomson, 1993*] Thomson, N. R., Experimental daytime VLF ionospheric parameters, *Journal of Atmospheric and Terrestrial Physics*, 55, 173, 1993.
- [*Uman et al., 1980*] Uman, M. A., Y. T. Lin and E. P. Krider, Errors in magnetic direction finding due to nonvertical lightning channels, *Radio Science*, 15, 35-39, 1980.
- [*Uman, 1987*] Uman, M. A., *The Lightning Discharge*, International Geophysics Series - Vol. 39, Academic Press, Orlando, 1987.
- [*Ushio et al., 2002*] Ushio, T., S. Heckman, K. Driscoll, D. Boccippio, H. Christian and Z. Kawasaki, Cross-sensor comparison of the Lightning Imaging Sensor (LIS), *International Journal of Remote Sensing*, 23, 13, 2703-2712, 2002.
- [*Wait, 1957*] Wait, J. R., The Attenuation vs. Frequency Characteristics of VLF Waves, *Proceedings of the IRE*, 45, 768-771, 1957.

- [*Wait and Spies*, 1960] Wait, J. R. and K. Spies, Influence of Earth Curvature and the Terrestrial Magnetic Field on VLF Propagation, *Journal of Geophysical Research*, *65*, 2325-2331, 1960.
- [*Wait*, 1962] Wait, J. R., Excitation of Modes at Very Low Frequency in the Earth-Ionosphere Wave Guide, *Journal of Geophysical Research*, *67*, 3823-3828, 1962.
- [*Wait*, 1968] Wait, J. R., Mode Conversion and Refraction Effects in the Earth-Ionosphere Waveguide for VLF Radio Waves, *Journal of Geophysical Research*, *73*, 3537-3548, 1968.
- [*Weidman and Krider*, 1986] Weidman, C. D. and E. P. Krider, The amplitude spectra of lightning radiation fields in the interval from 1 to 20 MHz, *Radio Science*, *21*, 964-970, 1986.
- [*Wood and Inan*, 2000] Wood, T. G. and U. S. Inan, Long Range Tracking of Thunderstorms Using Sferic Measurements, paper #A62D-16, *American Geophysical Union*, December, 2000.
- [*Yamashita and Sao*, 1974a] Yamashita, M. and K. Sao, Some considerations of the polarization error in direction finding of atmospherics - I. Effect of the Earth's magnetic field, *Journal of Atmospheric and Terrestrial Physics*, *36*, 1623-1632, 1974.
- [*Yamashita and Sao*, 1974b] Yamashita, M. and K. Sao, Some considerations of the polarization error in direction finding of atmospherics - II. Effect of the inclined electric dipole, *Journal of Atmospheric and Terrestrial Physics*, *36*, 1633-1641, 1974.
- [*Zajac and Rutledge*, 2001] Zajac, B. A. and S. A. Rutledge, Cloud-to-ground Lightning Activity in the Contiguous United States from 1995-1999, *Monthly Weather Review*, *129*, 999-1019, 2001.